THE UNIVERSITY OF CHICAGO

ELECTROSTATIC CHARGING AND PARTICLE INTERACTIONS IN MICROSCOPIC INSULATING GRAINS

A DISSERTATION SUBMITTED TO
THE FACULTY OF THE DIVISION OF THE PHYSICAL SCIENCES
IN CANDIDACY FOR THE DEGREE OF
DOCTOR OF PHILOSOPHY

DEPARTMENT OF PHYSICS

BY
VICTOR LEE

CHICAGO, ILLINOIS
DECEMBER 2017

To my parents Ming and Sherry, my brother Wayne, and my wife Sylvia for their loving support.

Table of Contents

List of Figures

Acknowledgments

I would like to express my sincere gratitude to my Ph.D. advisor, professor Heinrich Jaeger, for his tireless support and guidance. Heinrich gave me the space and independence necessary to grow as a researcher, inspired me to think creatively about my projects, and gave me prompt responses when I needed his help and advice. I learned a lot from him about how to become a scientist and a good presenter. His enthusiasm and encouragement make the Jaeger lab a wonderful environment for pursuing my Ph.D.

I also want to thank Scott Waitukaitis and Marc Miskin greatly for their guidence during my first two years in the Jaeger lab. They taught me useful experimental and computational techniques and provided many stimulating ideas in this work.

I would like to thank the members in the Jaeger group and the James Frank Institute, especially Qiti Guo and Justin Jureller for their teaching and technical advice. I have benefited from many useful discussions with Kieran Murphy, Leah Roth, Endao Han, Nicole James, Ivo Peters, Yifan Wang, Qin Xu, Sean McBride, Edward Barry, Sayantan Majumdar, Adam Wang, Melody Lim, Jelani Hannah, Remington Carey, Mengfei He, Nick Schade, Thomas Videbaek, and Kelliann Koehler. My sincere thanks also go to Juan de Pablo, Karl Freed, Jian Qin, and Jiyuan Li for our efficient collaboration.

I am very thankful for the members of my thesis committee Sid Nagel, Abby Vieregg, and Tom Witten for their insightful comments, guidance, and encouragement in the preparation of this thesis.

Finally, I want to thank my dear wife Sylvia who stands beside me during the years of my Ph.D. with love, encouragement, and support.

Abstract

In this thesis, we experimentally investigate the electrostatic charging as well as the particle interactions in microscopic insulating grains. First, by tracking individual grains accelerated in an electric field, we quantitatively demonstrate that tribocharging of same-material grains depends on particle size. Large grains tend to charge positively, and small ones tend to charge negatively. Theories based on the transfer of trapped electrons can explain this tendency but have not been validated. Here we show that the number of trapped electrons, measured independently by a thermoluminescence technique, is orders of magnitude too small to be responsible for the amount of charge transferred. This result reveals that trapped electrons are not responsible for same-material tribocharging of dielectric particles. Second, same-material tribocharging in grains can result in important long-range electrostatic interactions. However, how these electrostatic interactions contribute to particle clustering remains elusive, primarily due to the lack of direct, detailed observations. Using a high-speed camera that falls with a stream charged grains, we observe for the first time how charged grains can undergo attractive as well as repulsive Kepler-like orbits. Charged particles can be captured in their mutual electrostatic potential and form clusters via multiple bounces. Dielectric polarization effects are directly observed, which lead to additional attractive forces and stabilize "molecule-like" arrangements of charged particles. Third, we have developed a new method to study the charge transfer of microscopic particles based on acoustic levitation techniques. This method allows us to narrow the complex problem of many-particle charging down to precise charge measurements of a single sub-millimeter particle colliding with a target plate. By simply attaching nonpolar groups onto glass surfaces, we show that the contact charging of a particle is highly dependent on hydrophobicity. Charging between a hydrophilic and a hydrophobic surface is enhanced in a basic atmosphere and suppressed in an acidic one. Moreover, hydrophobicity is also found to play a key role in particle charging driven by an external electric field. These results strongly support the idea that aqueous-ion transfer is responsible for the particle contact charging phenomenon.

Chapter 1

Introduction

Electrostatic charges can be generated after two material surfaces are brought into contact and separated. This process, known as contact electrification or tribocharging, is commonly seen in granular systems. The large surface-area-to-volume ratio of granular materials enhances contact electrification, leading to important consequences in nature, such as strong electric fields and lightning in volcanic ash clouds (Fig. 1.1) [1], sandstorms [2], dust devils [3], and thunderstorms [4]. In industry, electrostatic charging is commonly seen in granular flow processes, causing clustering or segregation in fluidized beds [5] and pneumatic conveying [6], and catastrophic dust explosion due to electrostatic discharges in food and coal processing plants [7]. Electrostatic charging of microscopic particles is also extensively used in applications such as electrophotography [8], powder coating [9], and air filtering [10].

Surprisingly, despite its importance in many natural and technological areas, the mechanisms of how charges form have never been well understood, even though it has been studied since ancient Greece when Thales of Miletus showed that rubbing amber with a piece of fur causes electrostatic charging [12]. The "triboelectric series" (Fig. 1.2(a)) [13] has been empirically derived, which is an ordering of materials according to their tendency to obtain a positive or negative charge: a material closer to the top of the list usually charges positively, while the other material charges negatively. However, the basic mechanism behind the triboelectric series remains elusive. Even the species of charge carrier transferred between surfaces is still under debate. The aim of this thesis is to obtain further insight into the mechanism behind tribocharging, particularly in systems of microscopic insulating grains, as well as their mutual electrostatic interactions due to the tribocharging.

Figure 1.1: Spectacular lightning in the erupting Sakurajima Volcano in Japan in 2013. Photograph courtesy of Martin Rietze.

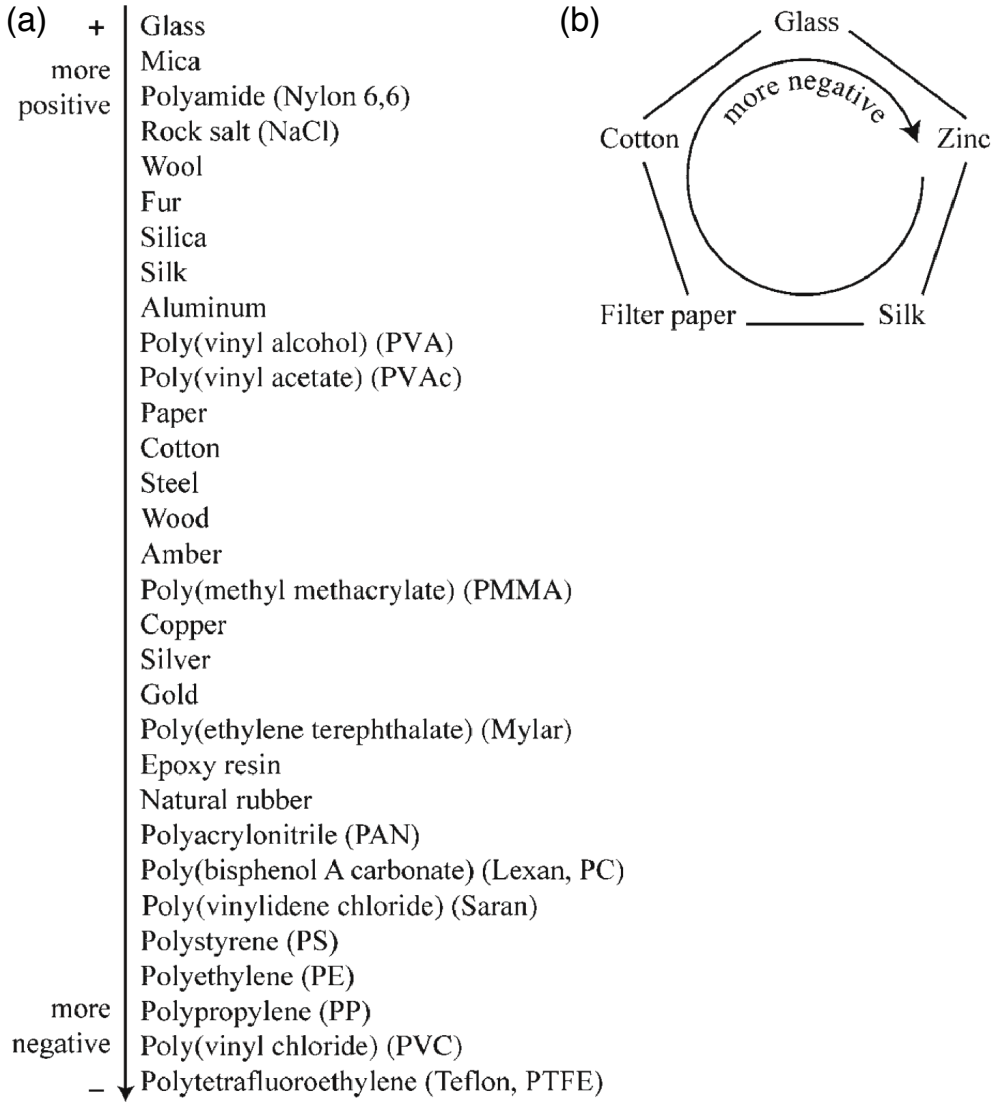

Figure 1.2: (a) Example of a triboelectric series that shows an ordering of materials according to their tendency to obtain a positive or negative charge. A material closer to the top of the list contacted with a material closer to the bottom of the list usually charges positively, while the other material charges negatively. (b) Example of a combination of five materials that form a cyclic triboelectric series. Adapted from reference [11].

1.1 Species of charge carriers

Nowadays it is still not clear what charge species is responsible for the tribocharging of insulators. By contrast, for metal-metal contact, electrons are widely believed to be the dominant charge species. The direction of charge transfer in metals depends on the Fermi levels (or the work functions). When two metal surfaces are brought into contact, electrons are transferred from the metal with the higher Fermi level (lower work function) to the metal with lower Fermi level (higher work function) [14, 15].

On the other hand, tribocharging of insulators is found not to be correlated with bulk electronic properties, such as the ionization energy, electronegativity, electron affinity, or dielectric constant [16]. It is also not intuitive why insulators, which have very low charge mobility, can transfer charges at all. To explain it, many mechanisms have been proposed, and candidates of charge carrier species include electrons, ions, and nanoscale bits of material. We will discuss the proposed mechanisms of charge transfer involving insulators below.

Electron transfer

In solid-state physics, an insulator is typically described as a material with a large band gap ($\gtrsim$ 4 eV), which is much larger than the available thermal energy ($k_BT = 0.026$ eV at room temperature). An electron cannot be transferred either to an already-filled valence band or to a conduction band with much higher energy. Based on this view, transfer of electrons seems energetically implausible for insulators.

However, it is claimed that insulators are not necessarily defect-free. There can be trap states in the band gap due to defects in insulators. As Lowell and Truscott pointed out [17, 18], there is evidence for trapped electrons existing in the trap states of insulators from thermoluminescence measurements. They developed a model that trapped electrons are responsible for the charge transfer of insulators, where the trapped electrons can tunnel between surfaces from a higher-energy trap state to an empty, lower-energy state during contact.

Experimental studies by Liu and Bard support the electron-transfer mechanism [19, 20]. They showed that charges transferred during contact electrification of polymers (Teflon rubbed with PMMA) could drive electrochemical reactions, which implies participation of excess electrons during contact electrification. An electron acceptor such as $Fe(CN)_6^{3-}$ was reduced to form $Fe(CN)_6^{4-}$ after contact-charged Teflon was immersed in a solution of $Fe(CN)_6^{3-}$. Likewise, Cu^{2+} was reduced to form Cu deposition after charged Teflon was immersed in a $CuSO_4$ solution. However, the species which drives the electrochemical reactions is controversial [21]. Radicals generated by bond cleavage of polymers are also considered to drive the electrochemical reactions [22].

Ion transfer

For the case of insulators containing mobile ions (ionic functional groups) on material surfaces, contact electrification is believed to be due to transfer of the mobile ions [11, 23–29]. This kind of material contains both loosely bound ions (mobile ions) and covalently bound counterions (immobile ions). The sign of charge developed on these materials during contact electrification is always the opposite sign of the mobile ions owing to the loss of mobile ions on their surfaces.

For insulators that do not contain mobile ions, a key question is: if contact electrification is due to ion transfer, what is the nature and source of these ions? McCarty and Whitesides proposed that contact electrification for non-ionic insulators, in general, might be due to the transfer of OH^- ions in adsorbed water from the environment [11]. In their model, OH^- ions tend to be adsorbed at the interface between adsorbed water and insulators, whereas H^+ ions stay solvated in water films. This preferential adsorption of OH^- ions at solid-water interfaces has been shown in the literature [30–32]. During contact, water bridges can form between two surfaces, and OH^- ions can be redistributed in water bridges, leading to charge transfer.

The ion-transfer mechanism is supported by the following studies: (i) atmospheric water

is found to enhance the contact electrification of insulators [33], presumably because water can improve mobilization of ions and act as the source of ions being transferred; (ii) merely varying humidity can change the charge on a material based on its acidic/basic property without any contact [34, 35], presumably due to ion exchange between the adsorbed water and the atmosphere; (iii) charge on a surface experiences step-like changes by lowering the atmospheric pressure [36], likely due to the release of ions at low pressure.

Material transfer

When two material surfaces are brought into contact, patches of material can transfer from surface to another. This material transfer process should involve chemical bond breaking, which is either heterolytic bond breaking that leads to charged species or homolytic bond breaking that leads to radicals. Thus, the patches of material are likely to carry charge and hence might provide a means for contact electrification.

This mechanism was first considered by Salaneck *et al.* [37]. They showed clear evidence of material transfer related to surface contact between polymers by using x-ray photoemission spectroscopy techniques. However, Lowell suggested that material transfer should only play a minor role in contact electrification, based on the result that material transfer happens mostly on the first contact while charge transfer can continue over many contacts [38].

Recently, Baytekin *et al.* showed experimental results that support the material-transfer mechanism. They observed that contacting polymers develop a "mosaic" of positively and negatively charged regions of nanoscale dimensions and that material transfer is concurrent with polymer contact electrification [39]. They suggested that the mosaic patterns might be due to differences in the mechanical properties of the contacting surfaces at the nanoscale.

1.2 Factors affecting charge transfer

Many factors are associated with the amount of charge transfer. For example, charge transfer often depends on the contact mode. Rubbing is known to enhance tribocharging compared to

simple touching or rolling [14], but it is not clear whether rubbing just increases the contact area, or if the charge transfer is enhanced by the stress associated with rubbing [15, 40].

There are also factors limiting the amount of charge transfer. For example, charge transfer is likely to be limited by the transferred charge itself, which generates an electric field that is against further charge transfer [14]. Moreover, if the electric field built up by charge is sufficiently high, sudden discharges can happen due to dielectric breakdown of the surrounding atmosphere and limit the charge on the surface [41]. The breakdown is dependent on the gas species and ambient pressure, which is described by Paschen's law [42]. Charge can also leak to ground through material surfaces. This effect is enhanced at high humidity, which creates a layer of adsorbed water that increases surface conductivity [11].

An additional complication is that even the direction of charge transfer is not always predictable from the triboelectric series [43]. For instance, Sow *et al.* have demonstrated that the direction of charge transfer can be reversed just by changing the strain of an elastic material when the material contacts a different material [44, 45]. Another example is that reversal of charge can occur for two different materials when they are brought into contact for longer times [46]. There are also some combinations of materials that form a "cyclic triboelectric series" [14]. For example, in Fig. 1.2(b) each material develops negative charge after contacting the next material in a counterclockwise direction. The existence of such cyclic series implies that a single physical property cannot explain all the propensities of charge transfer. It is probable that tribocharging involves more than one mechanism.

1.3 Tribocharging of granular materials

Although the triboelectric series and the above mechanisms may describe the charge transfer between different materials, they do not explain why tribocharging occurs in granular systems composed of *a single kind of material*. The phenomenon of same-material tribocharging is counter-intuitive since there is no obvious driving force for charge transfer. Lowell and Truscott proposed a model to explain the charge buildup between surfaces made of the

same material [18]. In this model, charge transfer (trapped-electron transfer) is a "one-way" process from a higher energy state on a surface to a lower energy state on another surface. Asymmetric contact area can thus lead to net charge transfer due to the depletion of high-energy trapped electrons [47]. However, it is also shown in other works that same-material tribocharging can actually occur with *symmetric* contact [48, 49]. This effect was explained by a model based on random microscopic variations of material properties [49], but what creates the variations remains unclear.

An interesting phenomenon in same-material granular systems is that there appears a tendency for larger grains to charge positively and smaller grains to charge negatively. For example, the electric field in dust storms is typically oriented upward [50], reflecting that the smaller, negatively charged particles are lighter and lifted higher than the positively charged, larger particles. Similar orientations of electric fields have also been measured in volcanic plumes [51] and polymer powders [52, 53]. Lacks and colleagues proposed a theory for this effect based on Lowell and Truscott's same-material charging model [54, 55]. In the theory, all high-energy trapped electrons can be transferred and depleted after many collisions, and the asymmetric surface contact area for the particles can result in larger particles charged positively and smaller particles charged negatively.

Pähtz *et al.* have shown that external electric fields can also break the symmetry between identical colliding particles and lead to charge transfer in granular materials [56]. In their model, a particle can be electrically polarized in an external electric field, causing one side of the particle more positively charged and another side more negatively charged. Charge transfer can occur with neutralization of two charged surfaces induced by the electric field at the point of contact. It was also suggested that this mechanism can lead to an exponential growth of charge in agitated granular materials [57].

Triboelectric charges of grains can lead to electrostatic forces that are important in the dynamics of granular flows, even though the electrostatic forces are often avoided in the simulation modeling of such systems. Examples include particle segregation in charged

granular streams [58], agglomeration in fluidized beds [59], prevention of pore clogging [60], and crystal self-assembly [61,62]. In nature, electrostatic forces can enhance the re-accretion efficiency of dust aggregates in the early stage of planet formation [63]. Harper *et al.* also showed that the electrification of sand on Titan can lead to large electrostatic forces that increase the threshold for sediment transport by an order of magnitude [64].

1.4 Overview of thesis

This thesis contains three projects investigating the electrostatic charging effects of insulating microscopic particles. In the first project (Chapter 2), we focus on the problem of how same-material insulating grains transfer charges by rubbing against each other. We study the particle-size dependence of charging by measuring the charge of individual grains while simultaneously differentiating grains by size with a falling-camera apparatus. In addition, we used this charge measurement apparatus together with a thermoluminescence technique to test the validity of the theory based on trapped electrons for the same-material tribocharging.

The second project (Chapter 3) continues to explore the effects of the same-material tribocharging on the dynamics of microscopic grains. Using the falling-camera apparatus, we are able to directly observe how microscopic charged particles undergo mutual electrostatic interactions in a low-gravity environment. We demonstrate how highly charged particles can attract others to form clusters particle by particle. We observed rich events of particle collisions such as capturing, bouncing, and fragmentation in charged granular streams. Moreover, we study the many-body polarization effects between charged dielectric particles, which are crucial in areas of colloid physics, polarizable ions, biomolecules, and dust evolution in protoplanetary disks.

In the third project (Chapter 4), we develop a new method based on acoustic levitation techniques to further investigate the charging mechanism of microscopic particles. This method allowed us to precisely measure the charge transfer of a single sub-millimeter particle colliding with a target plate without physically contacting foreign materials. This method

thus simplifies the interpretation of complex charging phenomena usually caused by many particle-particle or particle-wall collisions. With this method, we clearly show that particle contact charging is dependent on hydrophobicity of material surfaces, ambient gases, and external electric fields, all of which can be explained by a mechanism based on aqueous-ion transfer. This method, together with the model we develop in this thesis, opens up new opportunities for quantifying, understanding, and controlling contact electrification of particles.

Chapter 2

Size-dependent same-material tribocharging in insulating grains[1]

2.1 Introduction

Although tribocharging is typically assumed to arise from frictional contact between dissimilar materials, it can also be caused by interaction between objects made of the same material [65, 66]. Several observations indicate that the mechanism for same-material tribocharging in granular systems is related to particle size, with larger grains typically charging positively and smaller ones negatively. The electric field of dust devils, for example, is known to point upward, consistent with smaller, negatively charged grains being lifted higher into the air [67]. A similar mechanism is suspected to be responsible for the large electric fields and consequent lightning generated in volcanic ash clouds [1, 68–71]. Zhao *et al.* [72] showed that the charge-to-mass ratio for a variety of powder samples crossed from negative to positive as the particle diameter increased, indicating a similar trend. More recently, Forward *et al.* [73–76] conducted experiments which revealed a correlation between charge polarity and grain size for samples with a binary particle size distribution.

Lowell and Truscott [17] showed that dragging an insulating sphere across a plane made of the same material usually caused the sphere to charge negatively. They developed a model based on a combination of asymmetry between two contacting surfaces and the transfer of trapped electrons [17, 18], which they suggested tunnel between surfaces when contact offers the possibility for relaxing into an empty, lower energy state. If the initial surface density of trapped electrons is uniform, continually rubbing some small region of contact

1. Based on S. R. Waitukaitis, V. Lee, J. M. Pierson, S. L. Forman, and H. M. Jaeger, *Physical Review Letters*, 2014, **112**, 218001. Beyond this paper, in this thesis results from the energy dispersive x-ray spectroscopy measurements (Fig. 2.1(c)) are added. In this project, I was involved in preparing the samples, determining the composition of the grains with energy dispersive x-ray spectroscopy, measuring the particle size distributions with an optical microscope, conducting the falling-camera experiments, tracking particle motion to obtain the charges of individual grains, and measuring the net charges of the granular materials with a Faraday cup. This project was supported by the NSF under grant DMR-1309611.

(such as the tip of sphere) across a larger region (e.g., a plate) leads to a net transfer of charge to the smaller region. Lacks and co-workers [54, 55, 77] later showed how the same geometrical asymmetry also arises with random collisions among particles of different sizes. However, while in most situations the transferred charge species is negative, there are some materials, such as nylon, where the polarity is reversed, which points to the possibility that other charge species might be responsible (Hu *et al.* [78] recently suggested trapped holes might explain the polarity reversal). Given these observations and the lack of quantitative data specifically linking charge transfer to the presence of trapped electrons, their role in same-material tribocharging is uncertain.

Here we test whether or not trapped electrons are necessary for same-material tribocharging. First, we develop a noninvasive experimental technique that allows us to measure the charge of individual grains while simultaneously differentiating them by size. For a binary-sized sample, we show that charge is indeed transferred between the different sizes, with large grains becoming more positively charged and small ones more negatively charged. Assuming the trapped electron model is correct, the amount of charge transferred allows us to put a lower bound on the required trapped electron surface density before mixing. To test this assumption, we then directly measure the density of trapped electrons on the material surface prior to mixing with a thermoluminescence (TL) technique. The data put an upper bound on the actual surface density of trapped electrons that is orders of magnitude smaller than the lower bound required by the trapped electron model. This demonstrates that trapped electrons are not necessary for same-material tribocharging and suggests that other candidate charge carriers and mechanisms should be considered.

2.2 Experimental Setup

Our apparatus for measuring individual grain charges while simultaneously differentiating grains by size is shown in Fig. 2.1(a) [80]. For the granular material, we use fused zirconium dioxide silicate (ZrO_2:SiO_2, Glenn Mills Inc.) because it exhibits strong charging behavior

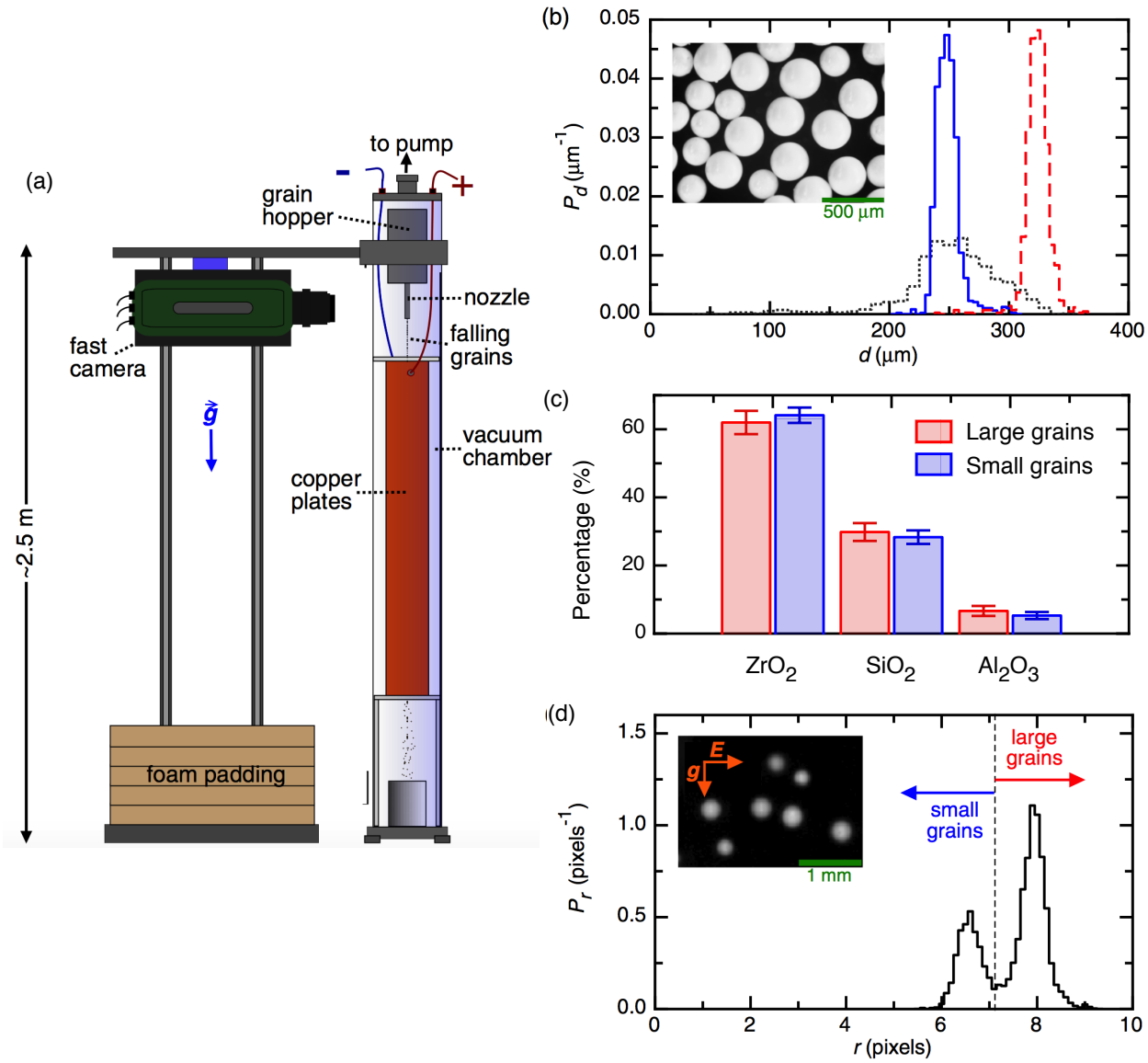

Figure 2.1: (a) Schematic of free-fall charge measurements. (b) Normalized particle size distribution determined by optical microscopy for unsifted grains (dotted grey line), sifted small grains (solid blue line), and sifted large grains (dashed red line). Inset: Microscope image of small and large grains. (c) Composition of the large and small grains measured with energy dispersive x-ray spectroscopy. (d) Radius distribution (pixels) of all grains as determined by the analysis of the free-fall video (we measure here the "radius of gyration"; see Ref. [79] for details). Dashed vertical line indicates cutoff between large and small grains. Inset: Small portion of an image from the high-speed video.

and because it is known to the thermoluminescence community for its capacity to store trapped electrons [81–84]. To ensure the grains are as materially identical as possible, we begin with an initially broad size distribution of grains from a single factory batch. We take this initial batch and mechanically sieve it into tighter distributions. We choose two cuts at the tails of the original distribution, the "large" and "small" grains, and measure their average diameters with an optical microscope, as in Fig. 2.1(b). For the experiments here, $\bar{d_l} = 326 \pm 10$ μm and $\bar{d_s} = 251 \pm 10$ μm. We have further confirmed that there is no apparent difference in the composition of the large and small grains with energy dispersive x-ray spectroscopy (Fig. 2.1(c)).

We use a Faraday cup to do a baseline measurement of the mean charges of the large and small grains before mixing. The method is illustrated in Fig. 2.2(a). Grains flow from the same nozzle/hopper as used in the experiment into an aluminum cup. This cup sits on an insulating plate inside a larger aluminum cup. The two cups are connected by a wire with a Keithley 6514 System Electrometer in charge measurement mode connected in series. As the grains fall into the inner cup, the electrometer records the current passing from the outer cylinder to the inner cylinder and simultaneously integrates the signal to acquire the charge in real time.

Results of the total charge collected in the cup Q vs. time t for the large and small grains are shown in Fig. 2.2(b). We see transient behavior at the beginning and end of the flow, but in the central region we see that Q simply increases linearly with t. We obtain the average charge from this measurement via the equation

$$\bar{q} = \frac{dQ}{dt}\frac{dt}{dM}\bar{m}, \tag{2.1}$$

where $\bar{q}$ is the average charge of a single grain, M is the total mass of grains in the Faraday cup, and $\bar{m}$ is the mass of an individual grain. For the grains used in this work, we find the mean charge of the large and small grains to be $-(3.1 \pm 0.3) \times 10^4$ e and $-(5.9 \pm 0.7) \times 10^4$

e (here e $= +1.6 \times 10^{-19}$ C), respectively. Interestingly, we tend to find a slight negative charge on the ZrO_2 grains before we mix them.

We then mix the two sizes by fluidizing with air in the grain-coated hopper for approximately 30 min. At this point we put the hopper into the vacuum chamber, as indicated in Fig. 2.1(a). Opening an orifice in the nozzle at the bottom of the hopper allows the grains to fall freely via gravity with reduced air drag (see Appendix A) between two large copper plates held at the potential difference V. The resulting electric field causes a grain of charge q and mass m to experience a horizontal acceleration $a = qV/ml$. Outside the chamber a high-speed, high-resolution video camera (Phantom v9.1, 1000 frames per second) guided by low-friction rails falls alongside the grains, which enables us to track their horizontal trajectories with precision and fit with parabolas to extract the accelerations a. The magnification and depth of field of our setup is high enough to allow us to distinguish a particle as large or small, as shown in Fig. 2.1(d). Performing approximately 25 camera drops at a given V allows us to measure the acceleration of several thousand grains and construct independent acceleration distributions for the large and small grains.

2.3 Results and discussion

In Fig. 2.3(a), we plot the acceleration distributions for the large and small grains at $V = 3.0$ kV ($|E| = 59$ kV/m), which shows that the small grains have predominantly negative accelerations, i.e., negative charge, while the large grains generally have positive accelerations. To extract the average charges $\bar{q_l}$ and $\bar{q_s}$, we calculate the mean accelerations $\bar{a_l}$ and $\bar{a_l}$ for each size and plot them as a function of V, as in Fig. 2.3(b). The proportionality between $\bar{a}$ and V confirms that the charge distribution is unaffected by the field and thus reflects the state of the sample as it exits the hopper (this proportionality would break down if particles collided and transferred charge inside the electric field, as in the mechanism proposed by Pähtz *et al.* [56]). From $\bar{a} = sV$, the slope $s = \bar{q}/l\bar{m}$ then gives access to the mean grain charge if the mass is known. Similarly, the width of the acceleration distribution, Δ_a, is related to

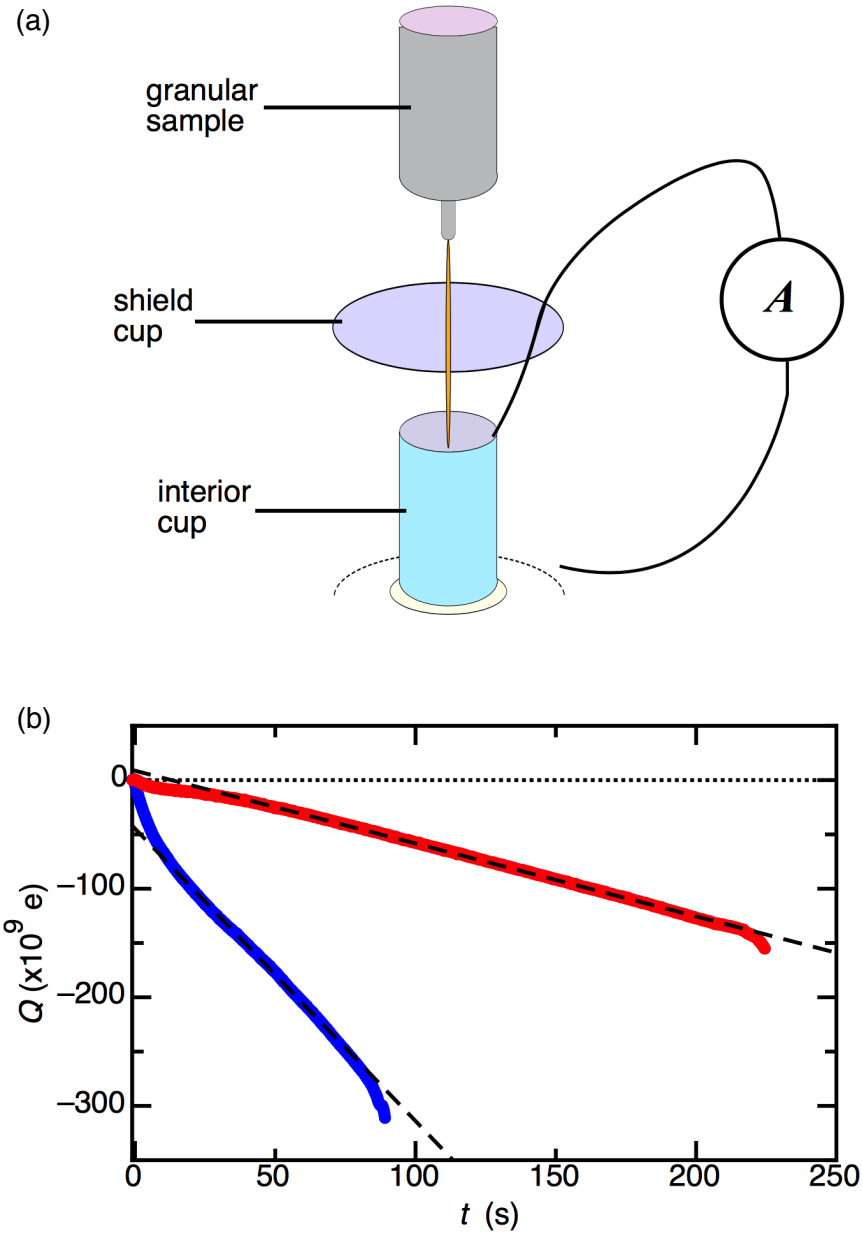

Figure 2.2: Faraday cup measurements. (a) Schematic of Faraday cup. Grains fall from the hopper/nozzle into the interior cup, which is connected by a wire to the grounded shield. The flow of charged grains into the interior cup causes it to draw an equal amount charge from the grounded shield. The resulting current is measured with an ammeter and the charge calculated by integration. (b) Total charge inside the interior cup Q vs. time t for the large (red) and small grains (blue) used in the experiment. The dashed lines are linear fits to the smooth, central region of each data set (i.e. we ignore the transient behavior at the beginning/end of each experiment).

the width of the charge distribution Δ_q via $\Delta_a = \sqrt{\delta_a^2 + (kV)^2}$, where $k = \Delta_q / l\bar{m}$ and δ_a is the average uncertainty in an individual acceleration measurement, independent of applied field.

From the specific material density $\rho = 3800$ kg/m^3 and the particle size distribution in Fig. 2.1(b) we compute the average grain masses as $\bar{m}_l = (7.0 \pm 1) \times 10^{-8}$ kg and $\bar{m_s} = (3.1 \pm 0.8) \times 10^{-8}$ kg. Using the fit values for the slope s this leads to mean charges $\bar{q}_l = (1.8 \pm 0.2) \times 10^6$ e and $\bar{q_s} = -(2.3 \pm 0.6) \times 10^6$ e for the two particle sizes. For the widths we obtain $(2.9 \pm 0.4) \times 10^6$ e and $(1.6 \pm 0.4) \times 10^6$ e for the large and small grains, respectively. Note that the values for the mean charge are 2 orders of magnitude larger than the residual grain charge prior to mixing. Within our experimental uncertainties total charge is conserved, which makes it explicit that the charge transfer is occurring among the grains themselves and not with some other material.

Assuming the trapped electron model is correct, the scale of charge transfer between the large and small grains allows us to put a lower bound on the surface density σ of trapped electrons that must have been present before the two sizes were mixed. If σ is the same for all grains initially and all the excess trapped electrons of the large grains are transferred to the small grains, it must be the case that $\sigma > N/[\pi(\bar{d_l}^2 - \bar{d_s}^2)]$, where N is the total number of electrons transferred. Given the measured number of transferred charges $N \approx 2.0 \times 10^6$, this implies $\sigma > 15$ μm^{-2}. The randomness of collisions makes this "complete transfer" scenario unlikely and, using the results of Lacks *et al.* [54], a more realistic estimate is $\sigma > 90$ μm^{-2}.

To see if enough trapped electrons to account for the observed charge transfer were present on the premixed grains, we use a technique from thermoluminescence dating. This is accomplished by heating a sample of the grains with a temperature ramp $T = T_0 + \beta t$ while simultaneously measuring the photon emission rate $\dot{N}$ with a photomultiplier [inset to Fig. 2.4(a)]. If trapped electrons are present, one observes peaks in $\dot{N}$ vs. T because although the emission rate increases with T, the available population N in the trap states is being depleted. (For an introduction to thermoluminescence, we refer the reader to Refs. [85–87].)

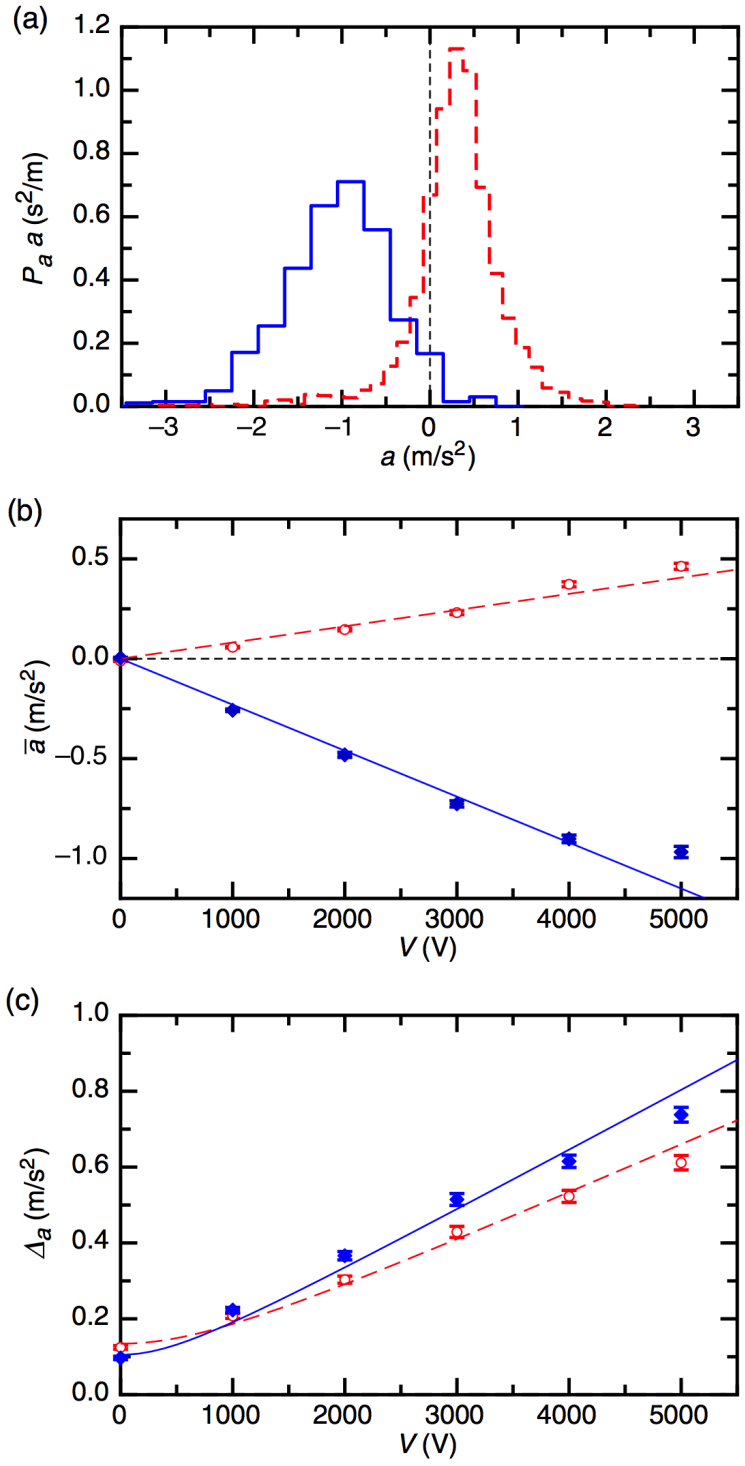

Figure 2.3: Size-dependent charging. (a) Acceleration distribution of small (solid blue line) and large (dashed red line) grains for $V = 3000$ V. (b) Mean acceleration $\bar{a}$ of small (blue solid diamonds) and large (red open circles) grains vs. V. Fits are of the form $\bar{a} = sV$. (c) Width of acceleration distributions Δ_a for small and large gains vs. V with the same symbols as (b). Fits are of the form $\Delta_a = \sqrt{\delta_0^2 + (kV)^2}$.

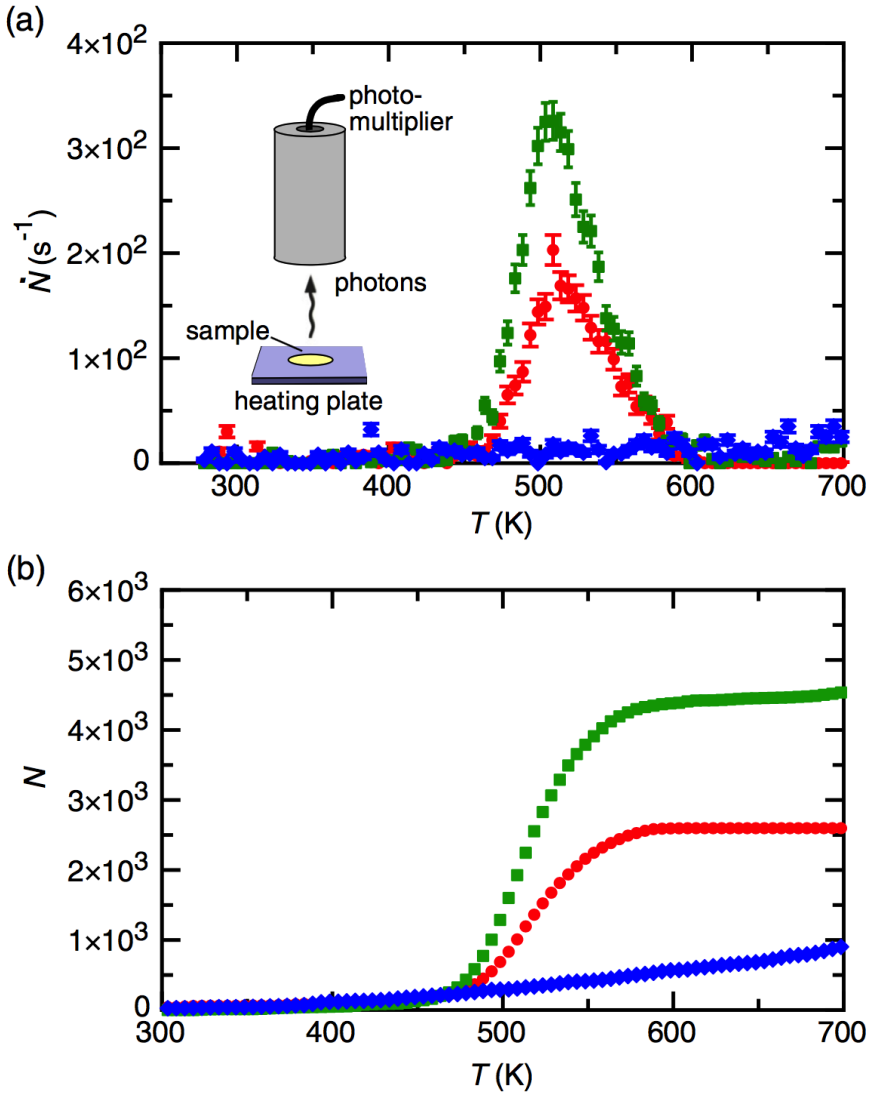

Figure 2.4: TL measurements of the trapped state density. (a) TL curves of photon count rate $\dot{N}$ vs temperature T at ramp rate 6 K/s for untreated grains (blue diamonds), grains exposed to ∼12 hours sunlight (red circles), and grains exposed to ∼12 hours UV lamp (green squares). Inset: Schematic of the TL measurement. (b) Total number of photons counted are for the same data as in (a).

In Fig. 2.4(a), we plot typical TL curves taken with a heating rate of $\beta = 6$ K/s (with a Thorn EMI 9635QB photomultiplier with peak quantum efficiency 0.29 at 375 nm). For grains from the same batch as the ones used in the experiments of Fig. 2.3, we are unable to detect trapped electrons (the slight rise in the $\dot{N}$ with T is a background "glow," not a TL peak). If we try to load electrons into the trap states by radiation, either from the Sun or from an ultraviolet lamp, we observe one characteristic TL peak.

By varying the ramp rate of the temperature in the thermoluminescence mea- surements, we can estimate the depth of the trapped state in the ZrO_2 grains. We start with the assumption that the trap release mechanism is an Arrhenius process, so that the total release rate of trapped electrons is

$$\dot{N} = -Nse^{-\epsilon/kT}, \tag{2.2}$$

where N is the total number of electrons in the trap, s is the frequency factor, ϵ is the trap depth, k is Boltzmann's constant and T is the temperature. If we ramp the temperature linearly with time (i.e. $T = T_0 + \beta t$), then we can rewrite the time derivative in terms of a temperature derivative

$$N' = \frac{-Ns}{\beta}e^{-\epsilon/kT}, \tag{2.3}$$

where we use the prime to indicate a derivate with respect to temperature. Next, to find the temperature at which the peak in N' occurs, we differentiate again with respect to temperature

$$N'' = -\left(N'se^{-\epsilon/kT} + Ns\frac{\partial}{\partial T}e^{-\epsilon/kT}\right) \tag{2.4}$$

$$= -\frac{Ns}{\beta}e^{-2\epsilon/kT} + \frac{Nse}{kT^2}e^{-\epsilon/kT}. \tag{2.5}$$

Setting this equal to zero and defining T^* as the temperature at which the peak occurs, we take the natural log of both sides to reveal an implicit relationship for T^* and ϵ

$$\ln\left(\frac{T^{*2}}{\beta}\right) = \frac{\epsilon}{kT^*} + C. \tag{2.6}$$

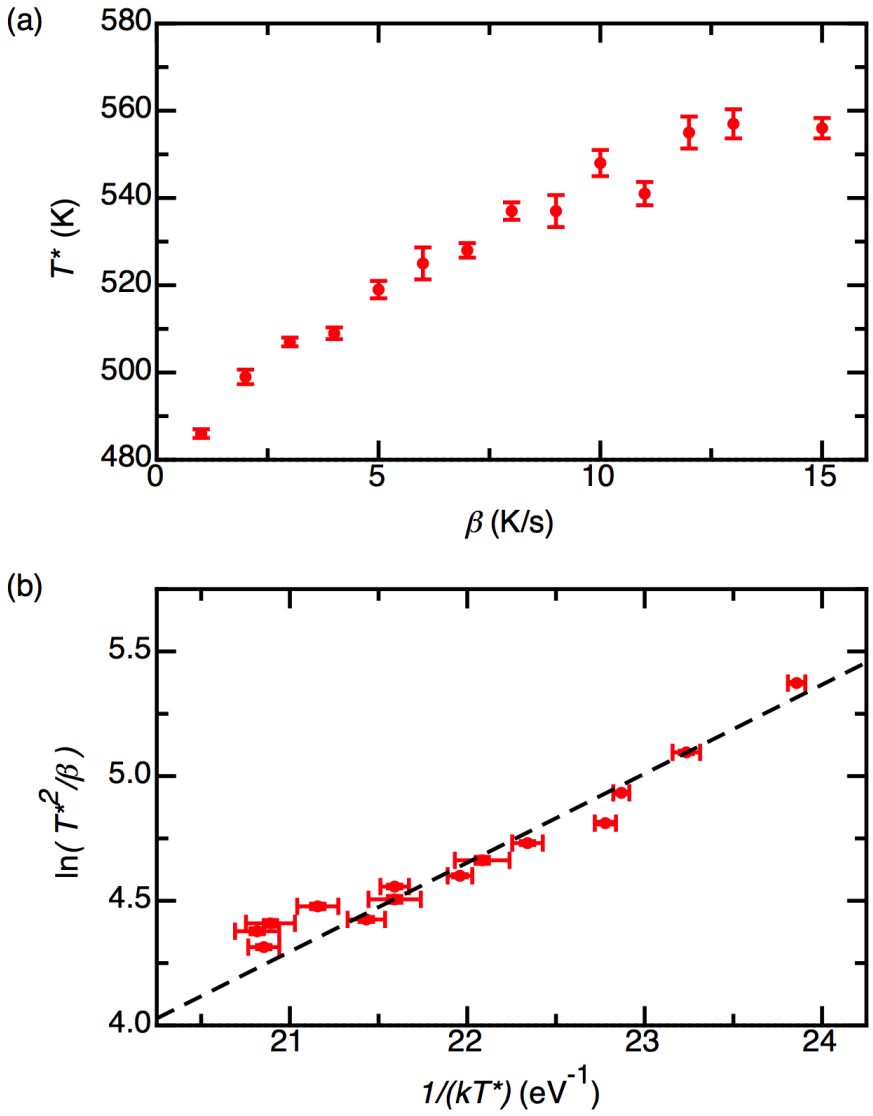

Figure 2.5: Measuring trap depth with peak shift. (a) Temperature at which maximum in photon count rate occurs T^* vs. heating rate β. (b) Reparamaterization of data in (a) according to Eq. 2.6. Fit is linear with slope $\epsilon = 0.36 \pm 0.01$ eV.

Therefore, if we plot $\ln({T^*}^2/\beta)$ vs. $1/kT^*$, we expect to find a line whose slope is ϵ.

In Fig. 2.5(a), we plot results for the shift in the peak T^* as a consequence of changing the heating rate β. As predicted, the peak occurs at later temperatures if the heating rate is increased. In Fig. 2.5(b), we parameterize our data as in Eq. 2.6 in order to determine the trap depth ϵ. Fitting this data to a line reveals $\epsilon = 0.36 \pm 0.01$ eV. This is a very typical value when compared to what is commonly seen in the literature [50, 77, 86, 87].

In Fig. 2.4(b), we plot the integrated number of photons counted for each sample, which shows that even with maximum trap loading no more than ∼5000 trapped electrons were present. Accounting for geometry and the gain of our photomultiplier setup, the actual surface density of trapped electrons is approximately $\sigma = 2\pi N/A_s\Omega$, where Ω is the solid angle common to the sample (∼5 sr) and the photomultiplier, and A_s is the area of the sample (∼1 cm^2). This reveals that the actual density of trapped electrons has an upper bound of $\sigma \approx 1 \times 10^{-4}$ μm^{-2}, 5 orders of magnitude lower than the amount necessary to account for the charge transfer we observe in the free-fall experiment.

In principle, it is possible that additional electrons exist at trap depths deeper than we can reach with the temperature range available to us, but several factors make this unlikely. First, although our TL measurement should be sensitive to traps as deep as ∼2 eV (provided the surface density of these traps $\sim 15-90$ μm^{-2}, as our charging data imply), we see no indication of traps beyond the one at $\epsilon \sim 0.36$ eV. Additionally, traps beyond ∼2 eV would be especially deep compared to what is typically reported in the literature [86]. More importantly, if traps did exist in this range, they would be susceptible to unloading via visible light ($\sim 1.8-3.1$ eV). This discrepancy is especially relevant to granular systems continually exposed to visible light from the sun, such as wind-blown dust or volcanic ash, which exhibit strong, same-material tribocharging behavior [1, 50, 67–71, 88–90]. We also considered the implications of possible size-dependent electric discharging, which might occur when the electric field at the surface of a particle exceeds the dielectric strength of the surrounding gas. However, any discharge would imply that the actual amount of charged transferred between

the large and small particles must have been larger than what we measured. Consequently, the required number of trapped electrons would also have to be larger, which makes the discrepancy with the thermoluminescence experiments more compelling still.

2.4 Summary

These considerations lead us to conclude that trapped electrons are not necessary for same-material tribocharging. This touches on an ongoing debate regarding the most fundamental question in tribocharging: what is the charge species being transferred? While in metal-metal tribocharging it has been shown that electrons are transferred [91, 92], insulator-insulator experiments have pointed to electron transfer [20, 93, 94], transfer of ions adsorbed on the surface [11, 24, 25, 39], and recruitment of ions from the atmosphere surrounding the contact [48].

In our case, the geometric mechanism implies a negatively charged species but trapped electrons are not the culprit, and we suspect that ions on the surface or recruited from the surrounding gas might be responsible. Several recent experiments suggest this could be the case. Baytekin *et al.* [39] showed that charge transfer between nonidentical insulating materials can be correlated with the breaking of molecular bonds on the surface. Alternatively, other investigations have pointed out the importance of molecularly thin layers of absorbed water [11, 24, 33]. In particular, McCarty and Whitesides suggest that contact charging between different insulating materials in general might be due to the transfer of OH^- ions. As they point out, the exact details of how OH^- ions might transfer are not clear, but in this scenario the density of transferrable charges is no longer an issue. Even with partial monolayer coverage the number of OH^- ions far exceeds the lower bound of 15 μm^{-2}. Thus, the transfer of OH^- ions in adsorbed surface water is an intriguing possibility that will be the subject of Chapter 4 in this thesis.

Chapter 3

Direct observation of particle interactions and clustering in charged granular streams[1]

3.1 Introduction

Clustering of fine particles is of crucial importance in settings ranging from the early stages of planet formation [63, 95, 96] to the coagulation of industrial powders and airborne pollutants [97–100]. Models of such clustering typically focus on inelastic deformation and cohesion [63, 97, 99, 101]. However, even in charge-neutral particle systems comprised of grains of the same dielectric material, tribocharging can generate large amounts of net positive or negative charge on individual particles, resulting in long-range electrostatic forces [55, 56, 102]. The effects of such forces on cluster formation are not well understood and have so far not been studied in situ. Here we report the first observations of individual collide-and-capture events between charged sub-millimeter particles, including Kepler-like orbits. Charged particles can become trapped in their mutual electrostatic energy well and aggregate via multiple bounces. This enables the initiation of clustering at relative velocities much larger than the upper limit for sticking after a head-on collision, a longstanding issue known from preplanetary dust aggregation [63, 103]. Moreover, Coulomb interactions together with dielectric polarization are found to stabilize characteristic molecule-like configurations, providing new insights for modeling of clustering dynamics in a wide range of microscopic dielectric systems, such as charged polarizable ions, biomolecules, and colloids [104–107].

1. Based on V. Lee, S. R. Waitukaitis, M. Z. Miskin, and H. M. Jaeger, *Nature Physics*, 2015, **11**, pp 733-737. Beyond this paper, in this thesis analysis of the polarization effects (Fig. 3.8 (a)-(c) and Fig. 3.9) is added. In this project, I had the leading role in most parts of the research including preparing the samples, conducting the falling-camera experiments, modeling the Kepler-like orbits, measuring the binding energy of the clusters, modeling the molecule-like configurations with polarization, and preparing the manuscript. This project was supported by the NSF under grant DMR-1309611. The Chicago MRSEC, supported by NSF DMR-1420709, is gratefully acknowledged for access to its shared experimental facilities.

3.2 Experimental Setup

One of the key difficulties in studying the interplay between repulsive contact forces, short-range cohesion, and long-range electrostatic forces during cluster formation has been to obtain sufficiently detailed experimental data. Seeing how this process unfolds demands in situ observation of the collision trajectories among charged grains to extract quantitative information about their interactions. This requires the grains to be freed from gravity and tracked with high spatial and temporal resolution to capture individual collision events [108, 109].

We overcome these obstacles with the setup shown in Fig. 3.1(a) [80, 110]. The particles we used are fused zirconium dioxide-silicate grains (68% ZrO_2, 32% SiO_2 by volume, material density $\rho = 3800\,\mathrm{kg/m^3}$; Glenn Mills Inc.), sieved to average particle diameters $d = 274\pm14$m for the monodisperse sample, and 326 $\pm$ 10 μm and 251 $\pm$ 10 μm for the binary sample (mixed in equal numbers by fluidizing with dry air for 30 minutes). Prior to the experiments, the grains were stored at 40-50% relative humidity. The grains were placed into a hopper mounted inside a transparent, cylindrical vacuum chamber that then was evacuated to < 2 mTorr by a turbo pump to eliminate air drag on the falling grains (see Appendix A). When a shutter covering a small orifice ($< 15d$) at the bottom of the vessel is opened, particles fall out freely, forming a a highly dilute granular stream. Outside the chamber, a high-speed video camera (Phantom v9.1) falls alongside the grains guided by low-friction rails. In the co-moving frame taken by the camera (1,000 frames per second), the effect of gravity is eliminated, making it possible to track particle interactions in detail for about 0.2 s until the camera is decelerated by a foam pad. This apparatus could also be used for $P(q)$ measurements, where the grains fall freely via gravity between two vertical large copper plates held at an external horizontal electric field E, causing a grain of charge q and mass m to undergo a horizontal acceleration $a = qE/m$. To extract the accelerations a, we tracked the horizontal trajectories and fitted with parabolas. Particles in the raw videos were identified and tracked with the algorithm developed by Crocker and Grier [79]. The

field was applied only to measure $P(q)$; all trajectories and clusters shown in this chapter were obtained without applied external electric field. See Ref. [80] for more details about the apparatus.

3.3 Results and discussion

Using particles with a narrow size distribution gives rise to the distribution of net grain charge, $P(q)$, shown in Fig. 3.1(b). This distribution is the result of a very large number of collisions and sliding/rubbing events among particles during sample preparation and outflow from the vessel [80]. It arises from tribocharging between grains of identical material and thus statistically similar surface density of transferrable charges, but slightly different surface area [55, 76, 111]. Overall charge is conserved and the distribution is centered around zero. As expected for nearly monodisperse grains, $P(q)$ is narrowly peaked. However, the tails of $P(q)$ extend to magnitudes of several million elementary charges e (1.6×10^{-19} C) per grain. Interactions involving these highly charged grains are the ones most easily detected and tracked, and in the following we focus on them.

Figures 3.1(c),(d) introduce the complex behaviors that arise when particle collisions involve charge, in particular the sequence of elliptical orbit fragments between successive bounces. The fact that the particles separate hundreds of micrometers before re-approaching each other is a clear indicator of long-range electrostatic forces, and being able to observe the orbits over several successive bounces implies that collisional energy losses are small, at least for binary collisions.

The electrostatic Coulomb force $\mathbf{F}(\mathbf{r})$ between two particles with net charges q_1 and q_2 separated by a (time-varying) distance $\mathbf{r}(t)$ gives rise to the equation of motion $\mu d^2\mathbf{r}/dt^2 = \mathbf{F}$, where $\mu = m_1 m_2/(m_1 + m_2)$ is the reduced mass. For non-polarizable particles, the electrostatic force is $\mathbf{F}(\mathbf{r}) = (1/4\pi\varepsilon_0)(q_1 q_2 \mathbf{r})/r^3$, where $\varepsilon_0 = 8.85 \times 10^{-12}$ C^2 N^{-1} m^{-2} is the permittivity of free space. The solution $\mathbf{r}(t)$ is a Kepler orbit. The sum E_0 of the translational kinetic energy (in the center-of-mass reference frame) and electrostatic

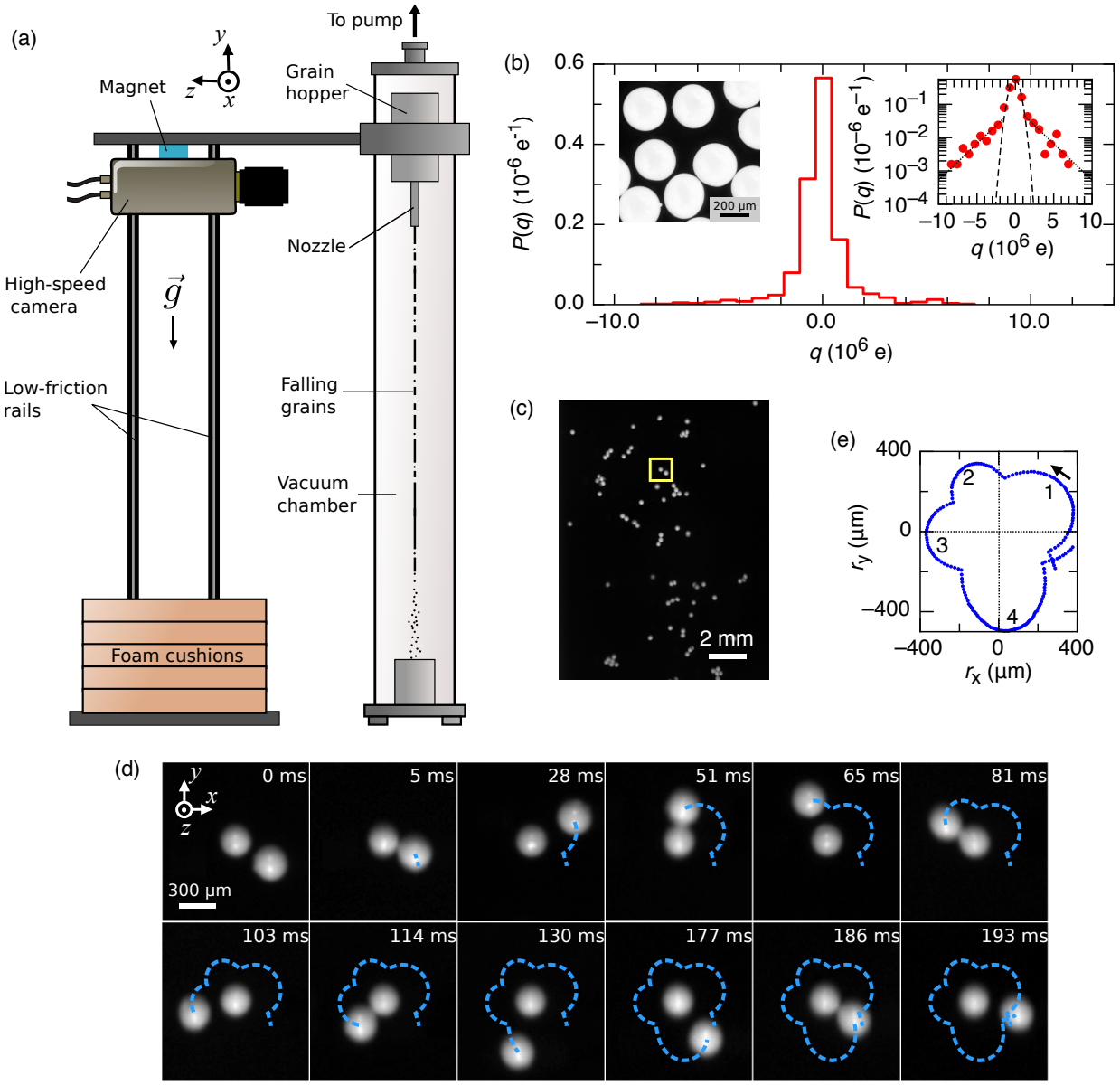

Figure 3.1: Free-fall video imaging of particle interactions. (a) Sketch of experimental set-up. Charged ZrO_2:SiO_2 grains fall freely inside a vacuum chamber, while their motion is captured by a co-falling high-speed camera. (b) Particle-charge distribution $P(q)$ for nearly monodisperse grains. Inset right: The same data plotted on a log-linear graph. Inset left: Optical micrograph of the grains. (c) Representative still frame from high-speed video, showing the dilute particle stream in the full field of view. (d) Sequence of zoomed-in still frames tracking the interaction of two oppositely charged grains. The image at $t = 0$ ms corresponds to the area inside the yellow frame in (c); subsequent frames have been re-centred to keep the slightly smaller grain in the middle of the image. Blue dashed lines indicate the path of the other grain as it repeatedly approaches and bounces off. (e) Horizontal (r_x) and vertical (r_y) components, in the x-y imaging plane, of the relative position vector of the grains in (d). The time interval between adjacent data points is 1 ms, the arrow indicates the direction of motion, and the numbers denote the four distinct trajectory segments between bounces.

potential energy determines whether $\mathbf{r}(t)$ forms an elliptical ($E_0 < 0$), parabolic ($E_0 = 0$), or hyperbolic ($E_0 > 0$) trajectory. For dielectric particles, important corrections arise from induced polarization [106, 107, 112]. These polarization forces are always attractive and become increasingly important at close approach.

In Fig. 3.2 we plot examples of observed trajectories together with best fits. In fitting the data, the unknown parameters are: the charges q_1 and q_2, the initial relative positions in the z direction (since the camera only images the x-y plane), and the initial relative velocities. We calculate μ by measuring the grain diameters in the videos and taking $\rho = 3800$ kg/m^{-3} as the grain density. The net (free) charge on a grain was assumed uniformly distributed over the surface. The dielectric constant of the grain material was taken as $\varepsilon \approx 15$, based on the volume-weighted average of $\varepsilon_{ZrO_2} \approx 22$ and $\varepsilon_{SiO_2} \approx 3.9$. To investigate trajectories between two particles, we only considered pairs of particles at least 800 μm away from surrounding grains in order to minimize multi-body effects. In addition, the relative acceleration (in the x-y plane) between the surrounding grains and the center of mass of the two investigated particles was less than 3% of the relative acceleration between the two investigated particles.

This fitting procedure consisted of two parts: (a) generating model trajectories by using the electrostatic interactions including polarization contributions, and (b) optimizing the input parameters for these model trajectories in order to obtain the best fit and thereby the best estimate for the particle charges.

To generate model trajectories a leapfrog integration was employed that numerically integrated the equation of motion [113]. The electrostatic forces including the full set of polarization terms calculated by a re-expansion method [112]. The integration was performed with a time-step size of 10^{-5} s. To insure that this time step was sufficiently small, we performed test integrations also using a time step of 10^{-7} s. The difference between these two time steps was less than 0.01 pixels in the position of an endpoint of a typical trajectory segment lasting about 50 ms between bounces, well within the ≈ 0.1 pixel uncertainty of our experimental position measurements.

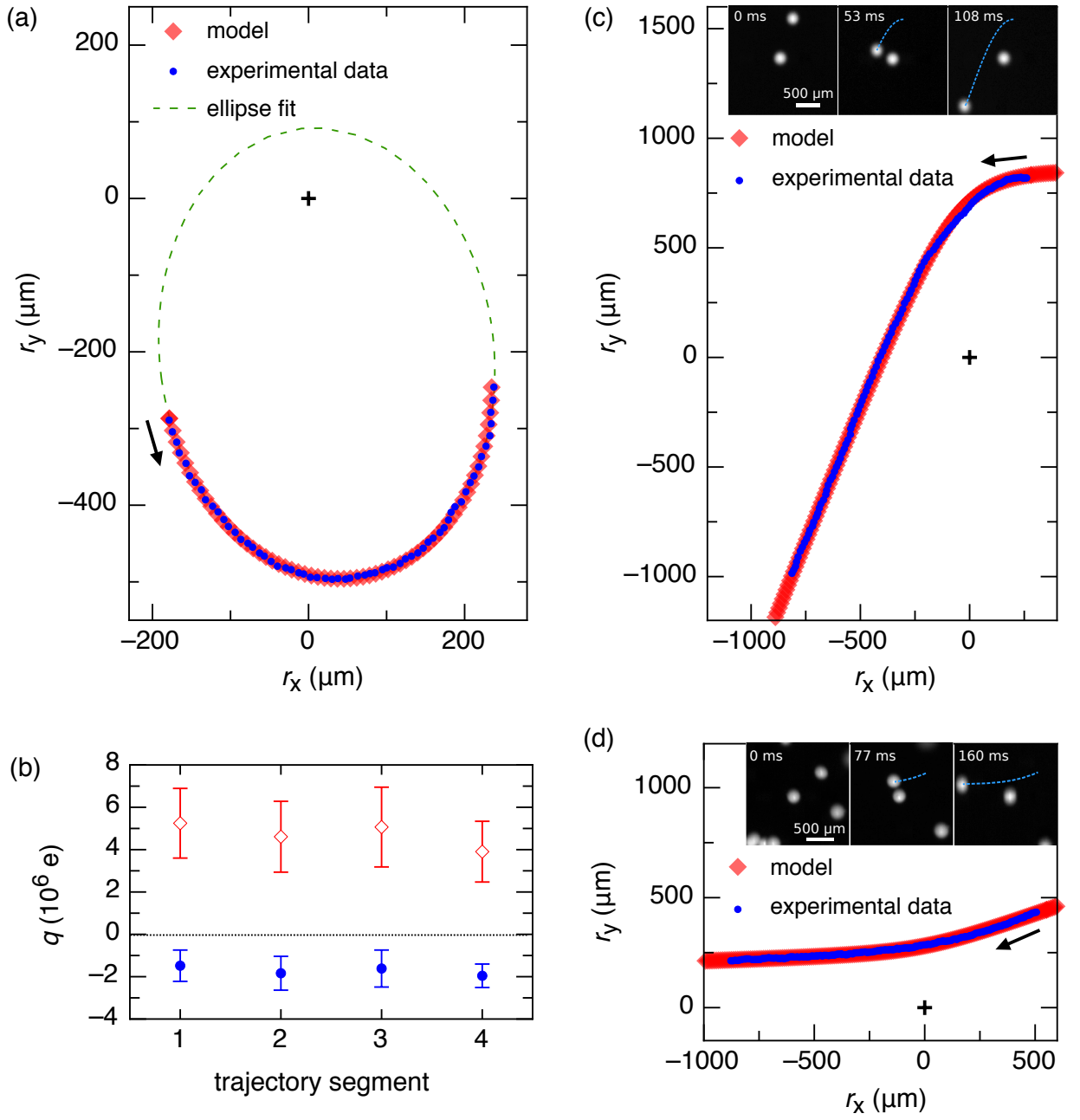

Figure 3.2: Kepler-like trajectories. (a) Relative position of the two grains from trajectory segment 4 in Fig. 3.1(d),(e) (blue circles). The data approximately follow an elliptical Kepler orbit (green dashed line) with focus at the origin (black cross). A fit including corrections for dielectric polarization effects is shown by the red diamonds. (b) Charges q_1 (red diamonds) and q_2 (blue circles) on the two particles in Fig. 3.1(d) for each trajectory segment, extracted from 10% best fits with polarization contributions. The length of the error bars corresponds to one standard deviation above and below the average. (c) Example of a hyperbolic trajectory due to attractive electrostatic interaction. (d) Hyperbolic trajectory due to repulsive interaction. Insets to (c) and (d): Still images from the videos from which the data were extracted. The arrows in (a),(c) and (d) indicate the direction of the relative motion at the beginning of the video.

A Nelder-Mead simplex algorithm [114] was used for multidimensional optimization of the model trajectories to get them as close as possible to the observed trajectories. Five hundred fitting trials were performed for each trajectory segment. For each fitting trial, random initial guesses of the fitting parameters (the charges q_1 and q_2 on particle 1 and 2, the initial relative positions in the z direction, and the initial relative velocities) led, via the algorithm, to a local minimum of the absolute median deviation between the model and the experimental trajectory data.

We used the reduced chi-square χ^2_{re} to measure the goodness of fit:

$$\chi^2_{re} = \frac{1}{\nu} \sum_{i=1} \frac{\|\vec{r}_{\text{data},i} - \vec{r}_{\text{model},i}\|^2}{\sigma^2}, \tag{3.1}$$

where ν is the number of degrees of freedom (the number of data points minus the number of fitted parameters minus one), $\vec{r}_{\text{data},i}$ and $\vec{r}_{\text{model},i}$ are the ith observed and model trajectory data point in x-y plane, and σ^2 is the estimated variance of position measurement. In Fig. 3.3(a) we plot the χ^2_{re} versus q for trajectory segment 1 in Figs. 3.1(d)&(e) as an example. Note it is possible for two particles with the same polarity ($q_1 q_2 > 0$) to attract each other with polarization forces as long as there is sufficiently large difference in charge magnitude.

Since the expression for the electrostatic force, including all polarization terms, is symmetric with respect to q_1 and q_2 when the particles have the same size [112], we are not able to unambiguously assign charges q_1 and q_2 to particle 1 and 2 in every fitting trial without further assumptions. Furthermore, the force will not change when the polarities of q_1 or q_2 are switched. To extract and assign charge values, we therefore set $q_1 > 0$ and assumed $|q_1| > |q_2|$, which is justified as long as there is no large amount of charge (on the order of the mean grain charge value, i.e., millions of e) transferred during a single collision. This assumption is reasonable given the published experimental results from collisions with fixed targets [103].

The values $\langle q_1 \rangle$, Δq_1, $\langle q_2 \rangle$, and Δq_2 were determined by the average and the standard

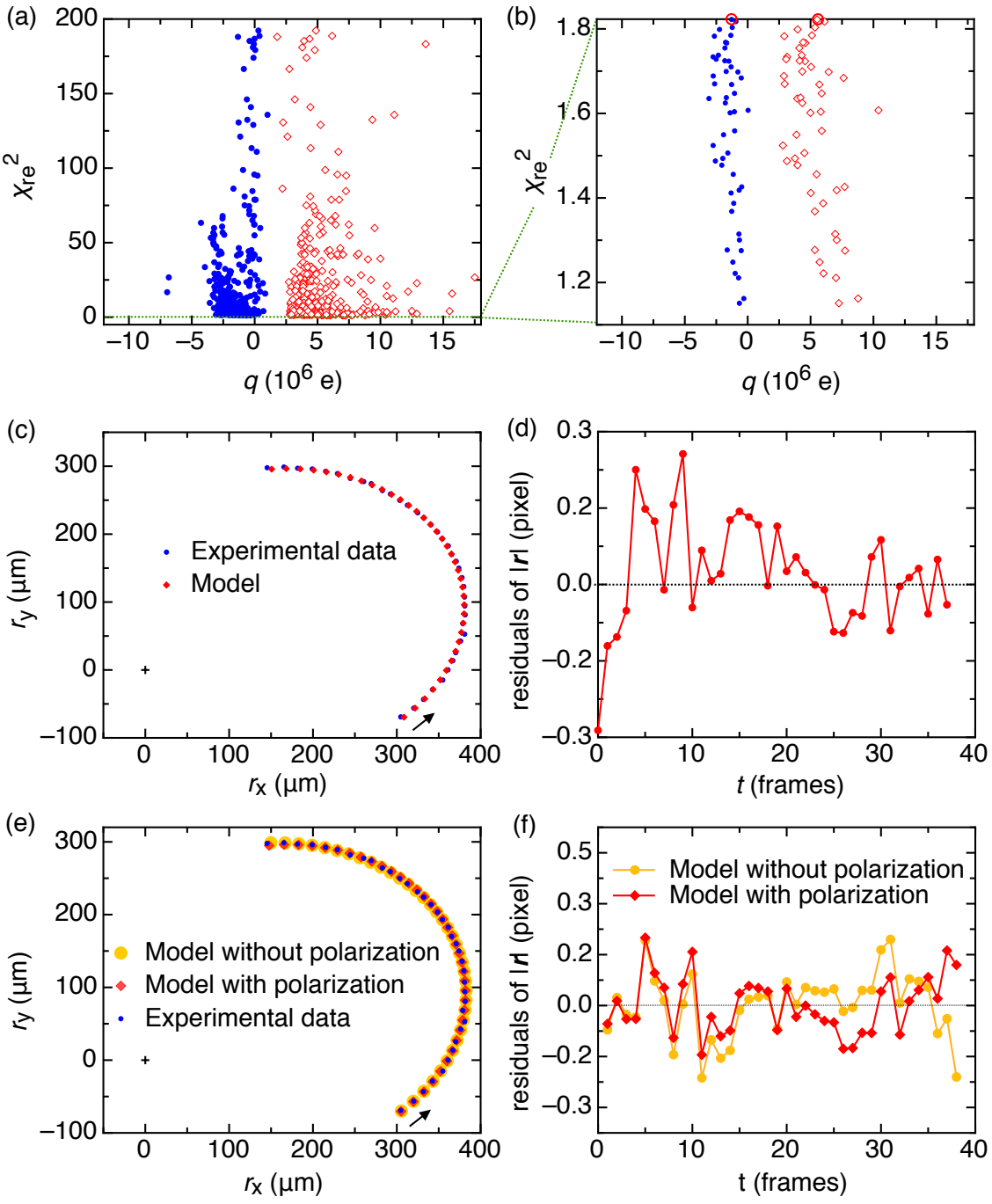

Figure 3.3: Charge determination from trajectory fitting. (a) Reduced chi-square χ^2_{re} vs charges on the two grains q_1 (open red diamonds) and q_2 (solid blue circles). (b) Zoomed-in data from (a) gives the 10% best trials that are used for q_1 and q_2 determination. (c) Comparison between experimentally observed trajectory (blue circles) and the model (red diamonds) for the circled datum in (b). (d) Residuals from fitting the trajectory to the model in (c), which gives a standard deviation of ~ 0.13 pixels. (e) Comparison between experimentally observed trajectory (blue circles) and the best fits with polarization contributions (red diamonds, $\chi^2_{re} = 1.12$), and without polarization contributions (yellow circles, $\chi^2_{re} = 1.28$). (f) Residuals from fitting the trajectory to the models in (e).

deviation of those q_1 and q_2 data that corresponded to the 10% smallest χ^2_{re} values (Fig. 3.3(b)). Note that even with the largest χ^2_{re} value within this 10% range (1.82 in Fig. 3.3(b)), the observed trajectory can be fitted well with the model trajectory (Fig. 3.3(c)). The standard deviation of residuals ($\|\vec{r}_{\mathrm{data},i}\| - \|\vec{r}_{\mathrm{model},i}\|$) from the fit is of the order of 0.1 pixels (Fig. 3.3(d)).

We also simulated the trajectories with electrostatic forces without considering polarization effect (Fig. 3.3(e)). Over the limited range in particle separation available and given the uncertainties of our experimental data, both types of fit seem similarly valid in terms of the fitting residuals and the best χ^2_{re} values (e.g., Fig. 3.3(f)). However, the charge product $q_1 q_2$ based on forces without polarization terms is larger than the one based on full polarization forces by about 40%. We note that, while the trajectories are also fit well by simple Kepler orbits, inclusion of the polarization contributions is important to obtain the correct charge values. If polarization terms are not included, there is only a term containing $q_1 q_2$ in the force, and there would be more freedom in picking widely different q_1 and q_2. With polarization terms, the fitting constrains the range of possible charge magnitudes.

For the collision sequence in Fig. 3.1(e), best fits indicate that q_1 and q_2 possess opposite polarities and stay near their initial values, approximately $+5.2 \times 10^6$ e and -1.5×10^6 e, respectively (Fig. 3.2(b)). The error bars on q_1 and q_2 from the fits are, however, too large to meaningfully constrain the amount of charge, Δq, transferred during a single collision. The actual Δq is likely much smaller. Extrapolating kinetic-energy-based results [103] for micrometre-sized SiO_2 particles hitting a large fixed target gives a rough estimation of $\Delta q \approx 1000$ e per collision, at less than 1/1000 of the total grain charge too small to noticeably affect the trajectories.

We also encounter collisionless interactions, such as hyperbolic Kepler orbits, where one of two oppositely charged grains effectively acts as a slingshot for the other, and trajectories between grains of equal polarity that repel each other. Examples are shown in Fig. 3.2(c),(d).

Figure 3.4 presents the observed trajectories from other single-particle collision events

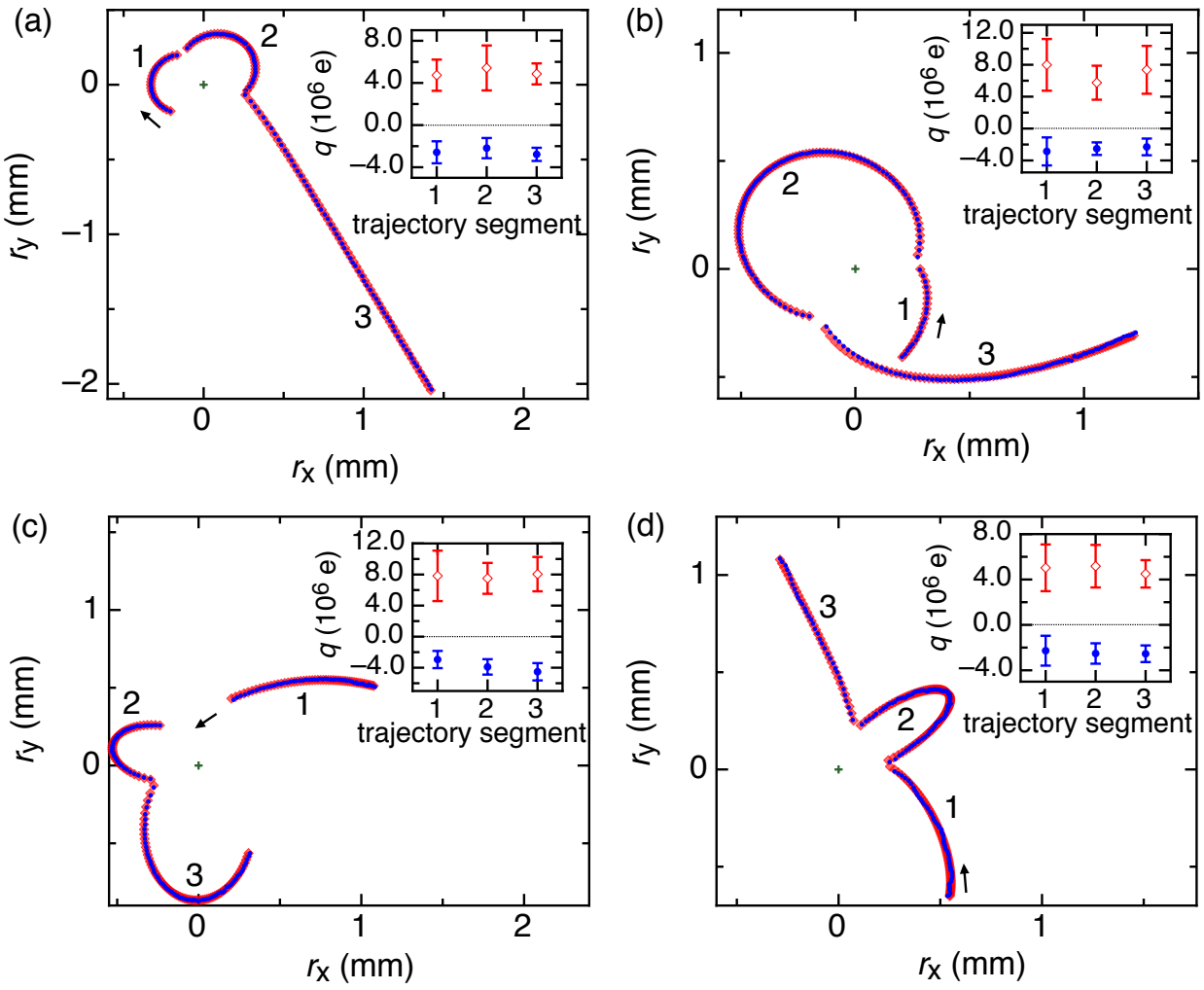

Figure 3.4: (a)-(d) Comparison between experimentally observed trajectories (blue circles) and model trajectories (red diamonds). Insets: Charges on the two grains q_1 (open red diamonds) and q_2 (solid blue circles) for each model trajectory segment as indicated by the numbers. The length of the error bars corresponds to one standard deviation above and below the average. The trajectories in (a) correspond to the grains shown in Fig. 3.5(a). For trajectories in (b)-(d), the image sequences of grains are shown in Appendix B.

and compares them to the best-fit model with polarization forces. As the trajectories are all curved toward the origin, there is no obvious transition from attractive to repulsive trajectories during collisions. Some parts of trajectories during collisions are not shown in the figure because of difficulties to extract them with the particle-tracking procedure [79] when two particles touch or when one grain blocks another one within the field of view. The insets to Fig. 3.4 show that the corresponding q_1 and q_2 values in each case stay, within error bars, at their initial values.

Returning to the issue of aggregation, the relative velocity of colliding particles has to stay below $v_{\rm stick} = (2W_{\rm coh}/\mu {e_{\rm eff}}^2)^{1/2}$ in order for them to stick [100, 101]. Here $W_{\rm coh}$ is the work required to break the bond formed by short-range cohesive forces, including van der Waals forces or capillary forces due to absorbed molecular layers [110], and $e_{\rm eff}$ is an effective coefficient of restitution (the ratio of relative velocity magnitude before and after a collision). We find $e_{\rm eff} \approx 0.94$ from analysis of head-on binary collisions at velocity 1.4 m/s (see Appendix C), close to 0.97 reported [115] for small soda lime glass spheres impacting at $0.5 - 1$ m/s. Grains typically will lose some translational kinetic energy in binary collisions, but particle rotation can have a significant effect. An example is shown in Fig. 3.5(a), where, after two collisions with elliptical trajectories in between, a third collision makes one grain suddenly take off on a hyperbolic trajectory. In this case, the fast-rotating grain was slightly non-spherical and this made it possible to determine its rotational kinetic energy, which during this last collision decreased by 10 pJ, an amount that matches the measured increase in total translational kinetic energy calculated from its trajectory shown in Fig. 3.4(a). Thus, the conversion of rotational into translational kinetic energy via during impact can lead to $e_{\rm eff} > 1$.

However, when single particles collide with clusters of particles, we find that the effective coefficient of restitution is significantly less than unity, likely because now energy can also be dissipated via intra-cluster rearrangements. Figure 3.5(b) illustrates this with snapshots in which two additional particles, one after the other, aggregate onto a cluster comprised

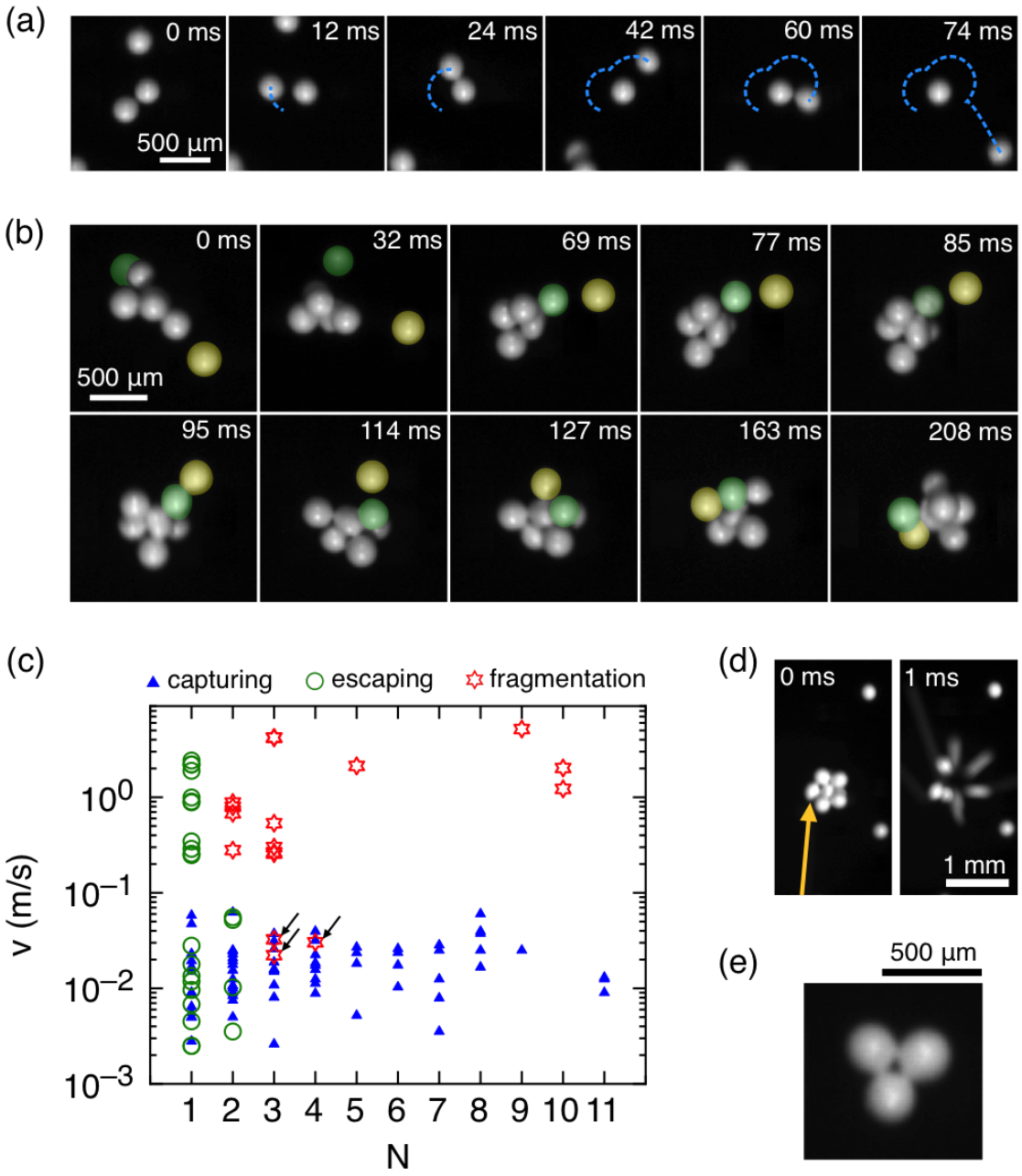

Figure 3.5: Separation and aggregation of charged dielectric particles. (a) Time sequence of particles bouncing and re-approaching over two collisions but separating after the third. (b) Time sequence of two particles (coloured green and yellow) aggregating onto an already formed five-particle cluster. (c) Collision outcomes for a single particle colliding with relative velocity v (in the x-y plane) with a cluster comprised of N particles: capture (blue triangles), escape (green circles) and fragmentation (red stars). Arrows indicate fragmentation events where only one particle is kicked out from the cluster, which we can use to estimate the binding strength (see text). (d) Example of a fragmentation event, showing a $N = 9$ cluster right before and 1 ms after being hit by a fast moving particle, whose direction is indicated by the yellow arrow. (e) Polarization forces can stabilize close-packed arrangements of contacting grains.

of $N = 5$ particles. There are three possible outcomes when an incident particle strikes a cluster: the incident particle is trapped in the mutual electrostatic potential well and after one or more bounces sticks to the cluster, as in Fig. 3.5(b) (capture); the particle bounces and escapes from the potential well (escape); or the particle kicks out one or more different particles from the potential well (fragmentation). Figure 3.5(c) shows that escape is suppressed for $N = 2$, and for $N > 2$ the incident particle is always captured unless it fragments the cluster.

We can use fragmentation events in which only a single particle is kicked out (arrows in Fig. 3.5(c)) to estimate the depth of the potential well that binds grains to the cluster. The kinetic energy $\mu v^2/2$ of the incident particle must overcome the short-range cohesive energy W_{coh} plus the initial electrostatic potential energy U stored in a bond. In Fig. 3.5(c), the minimum incident velocity for fragmentation is approximately 0.02 m/s and of similar magnitude as the maximum velocity v_{capture} for capture, corresponding to a kinetic energy of approximately 4 pJ. This is three orders of magnitude larger than the value $W_{\mathrm{coh}} \leq 10^{-15}$ J found for copper and glass grains of similar size [110]. Thus U clearly dominates the binding energy. Equating the incident kinetic energy with the Coulomb energy, $\mu {v_{\mathrm{capture}}}^2/2 = (1/4\pi\varepsilon_0)|q_1 q_2|/d$, we estimate $(|q_1 q_2|)^{1/2} \approx 2 \times 10^6$ e. This large amount of net charge per particle confirms the notion that at least some of the grains in a clusters are drawn from the tails of the charge distribution $P(q)$ in Fig. 3.1(b).

The fact that $P(q)$ is peaked around zero makes it very likely to find cluster configurations where one highly charged particle has attracted several particles with much smaller charge magnitude. A signature of this is a closely packed arrangement of three or more grains all in direct contact, such as particles inside the cluster in Fig. 3.5(b) or the triangular configuration in Fig. 3.5(e). For particles with high dielectric constant such configurations can be stabilized through the always attractive polarization forces, even if contacting grains have the same polarity, provided there is significant contrast in charge magnitude [116]. Seeing such dynamics in situ highlights the particularly important role polarization can play

in dust aggregation, initiating cluster formation from a single charged particle and potentially leading to runaway growth [105].

Going further, we can use the shape of the charge distribution to control the aggregation outcomes. In particular, for a bimodal $P(q)$ with positive and negative peaks roughly symmetric around zero, we would expect typical cluster configurations in which contacting grains exhibit alternating polarity. Recent experiments have demonstrated that such a $P(q)$ can be achieved by mixing bidisperse same-material grains [111]. The $P(q)$ for such mixture using diameters 326 $\pm$ 10 μm and 251 $\pm$ 10 μm is shown in Fig. 3.6. Since tribocharging will transfer charge in a manner that the larger grains become on average positive and the smaller grains negative [76, 111], this has the added benefit that polarity can be identified directly from the images by particle size. Figure 3.7(a) shows a taxonomy of the resulting, experimentally observed cluster configurations. These structures resemble molecules or fragments of self-assembled, electrostatically stabilized lattices [61, 104].

Modeling these "granular molecules" by taking many-body polarization effects into account we used a technique recently introduced by Barros *et al.* [117], meshing each grain into 720 polarizable patches. The free charges for large ($d = 326\mu$m) and small ($d = 251\mu$m) grains were set to the averages for the bimodal $P(q)$ in Fig. 3.6, i.e. to $+1.8 \times 10^6$ e and -2.3×10^6 e, respectively (the one exception was the L_1S_4 structure, which required charges $\pm 1.8 \times 10^6$ e for a stable 4-armed "tetrapod"). The free charge on each particle was distributed uniformly over its surface. The additional surface bound charge due to polarization was then calculated iteratively until the electrostatic energy U_n at iteration n changed less than $|(U_n - U_{n-1})/U_{n-1}| < 10^{-4}$. A Nelder-Mead algorithm [114] was used to identify, for given numbers of large and small grains, those spatial arrangements that produce local minima in the electrostatic energy and thus are candidates for stable states. As a hard-sphere constraint in the energy minimization the condition of $(d_A + d_B)/2 < r_{AB}$ was used, where d_A and d_B are the diameters for any two particles A and B, and r_{AB} is the center-to-center distance between them. We find that most of the observed configurations correspond to

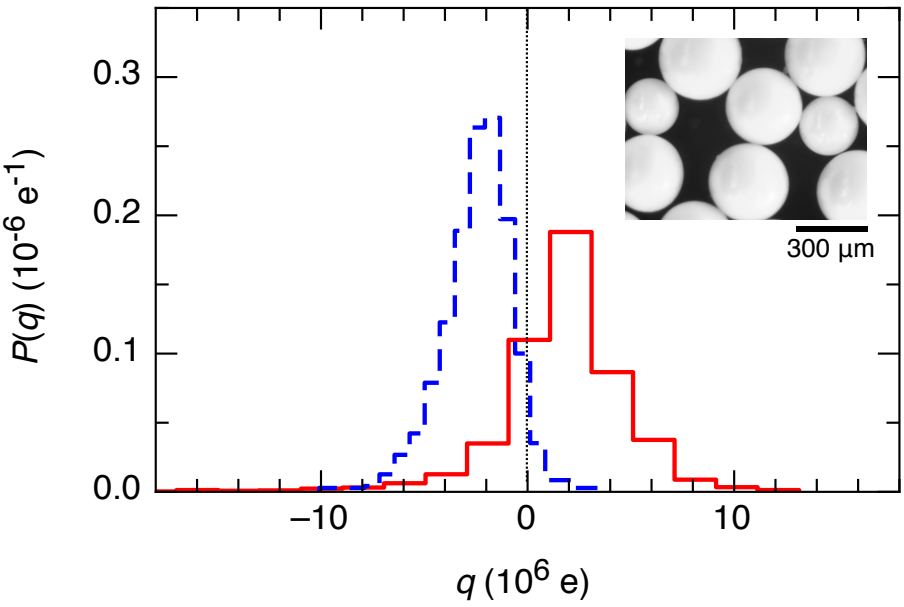

Figure 3.6: Charge distribution resulting from mixing grains with diameters 326 ± 10 μm and 251 ± 10 μm in equal number. The large grains (red solid line) are predominantly (80%) positive whereas the small grains (blue dashed line) are predominantly (95%) negative. Inset: Optical micrograph of large and small grains.

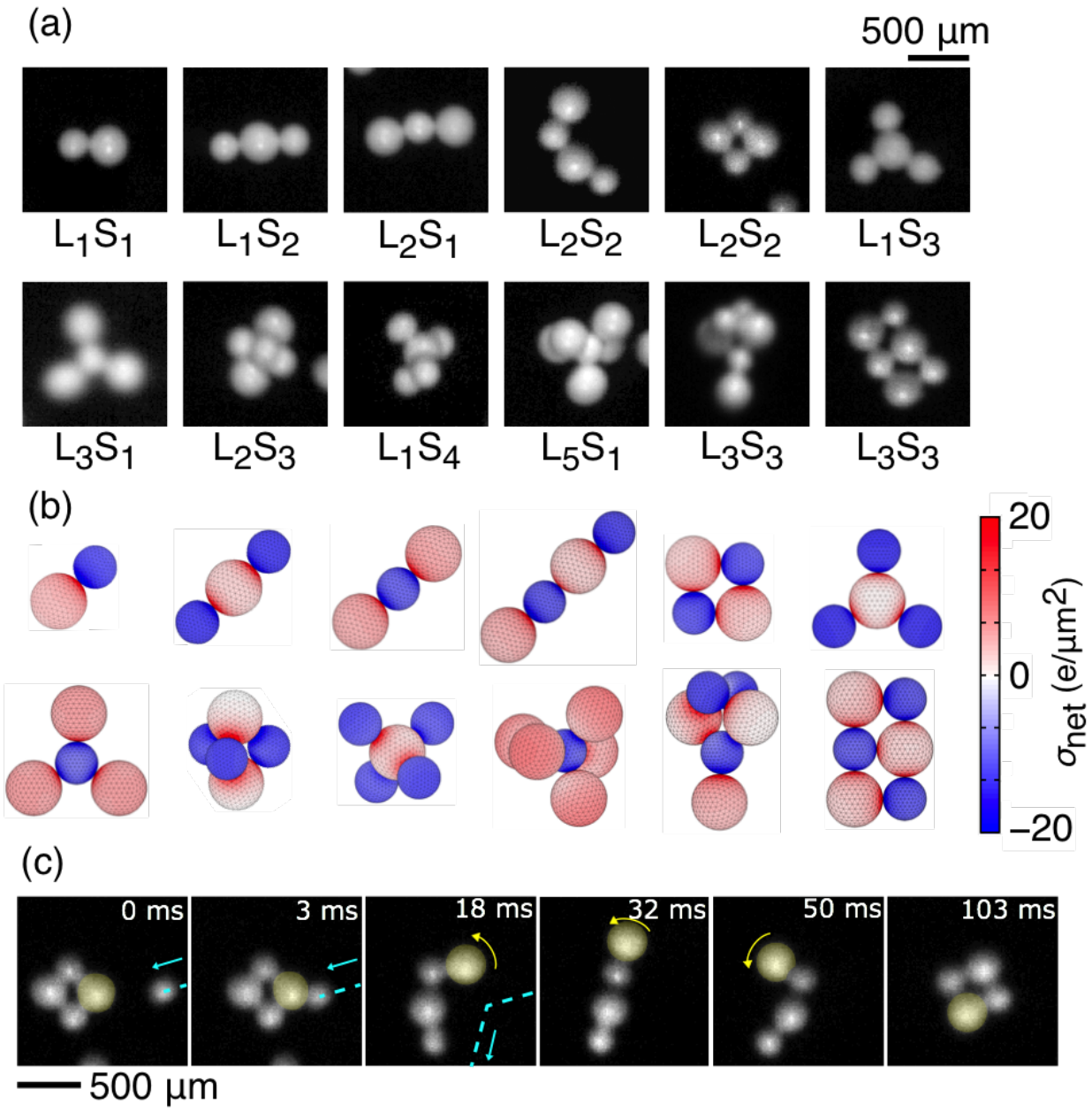

Figure 3.7: Granular molecules formed from bimodal particle-charge distribution. (a) Still images of granular molecules. Their structure consists of alternating large and small grains (labelled L_mS_n , where $m+n$ is the total number of particles in the molecule), giving rise to string-like (L_1S_1, L_1S_2, L_2S_1, L_2S_2), square (L_2S_2, L_3S_3), trigonal planar (L_1S_3, L_3S_1), tetrahedral (L_1S_4) and triangular bipyramid (L_5S_1) geometries. (b) Stable granular molecule configurations corresponding to (a), obtained by minimizing the total electrostatic energy (including polarization effects) for grains with net charge equalling the average positive ($+1.8 \times 10^6$ e) or negative (2.3×10^6 e) charge of the bimodal $P(q)$ shown in Fig. 3.6. Colour represents the net surface (free and bound) charge density σ_{net}. (c) Sequence of stills showing conformation change of an L_2S_2 molecule after impact from the right (arrow). The square structure breaks open, becomes linear, and returns to square.

energetic ground states (Fig. 3.7(b)). Some combinations of large (L) and small (S) particles can have more than one stable state. As an example, Fig. 3.7(c) shows a square L_2S_2 molecule reconfiguring into a linear shape after being impacted and then back to a square, suggesting that the square shape is the ground state while the linear configuration is metastable (calculation shows that the energy for the square shape is 1 pJ lower).

Since like charges of similar magnitude repel each other, the configurations in Fig. 3.7(a), which are all based on a bimodal $P(q)$, tend to be less densely packed than clusters formed from a $P(q)$ with a single peak around $q = 0$ (Fig. 3.1(b)). This is exemplified by the star-shaped configurations L_3S_1 and L_1S_3, the tetrapod L_1S_4, and the L_3S_3 structure. However, forces due to polarization become important at close approach, leading to additional attractive forces (Fig. 3.8(a)-(c)). Figure 3.8(d) demonstrates an event in which a dimer captures another particle to form a stable triangular configuration, and Fig. 3.8(e) shows one of many possible charge assignments that can produce this stable configuration, where the charges are $+1.8 \times 10^6$ e and $+0.2 \times 10^6$ e for the large grains, and 2.3×10^6 e for the small grain. As mentioned before, for large differences in charge magnitude the polarization forces can pull same-polarity grains into contact. Figure 3.9 (a) shows an example of the electrostatic potential energy between two same-polarity grains including the full set of polarization terms $U_{\text{polarization}}$ compared to the potential energy without the polarization terms U_{Couloub} with particle net charges $Q_1 = 15$ C and $Q_2 = 1$ C and $\varepsilon = 10$. $U_{\text{polarization}}$ excibits a peak value at a critical distance $r = r_{\text{critical}}$, which is the distance where the sign of the mutual force between the two particles $F = -dU_{\text{polarization}}/dr$ turns. F is attractive at $r < r_{\text{critical}}$ and repulsive at $r > r_{\text{critical}}$. In Fig. 3.9 (b) we plot r_{critical} as a function of ε and charge asymmetry Q_1/Q_2. r_{critical} increases as ε and Q_1/Q_2 increase due to high attractive polarization forces. There is a region in Fig. 3.9 (b) that particles do not attract to each other even when they touch. The minimum Q_1/Q_2 required to have an attractive mutual force at close approach decreases with ε.

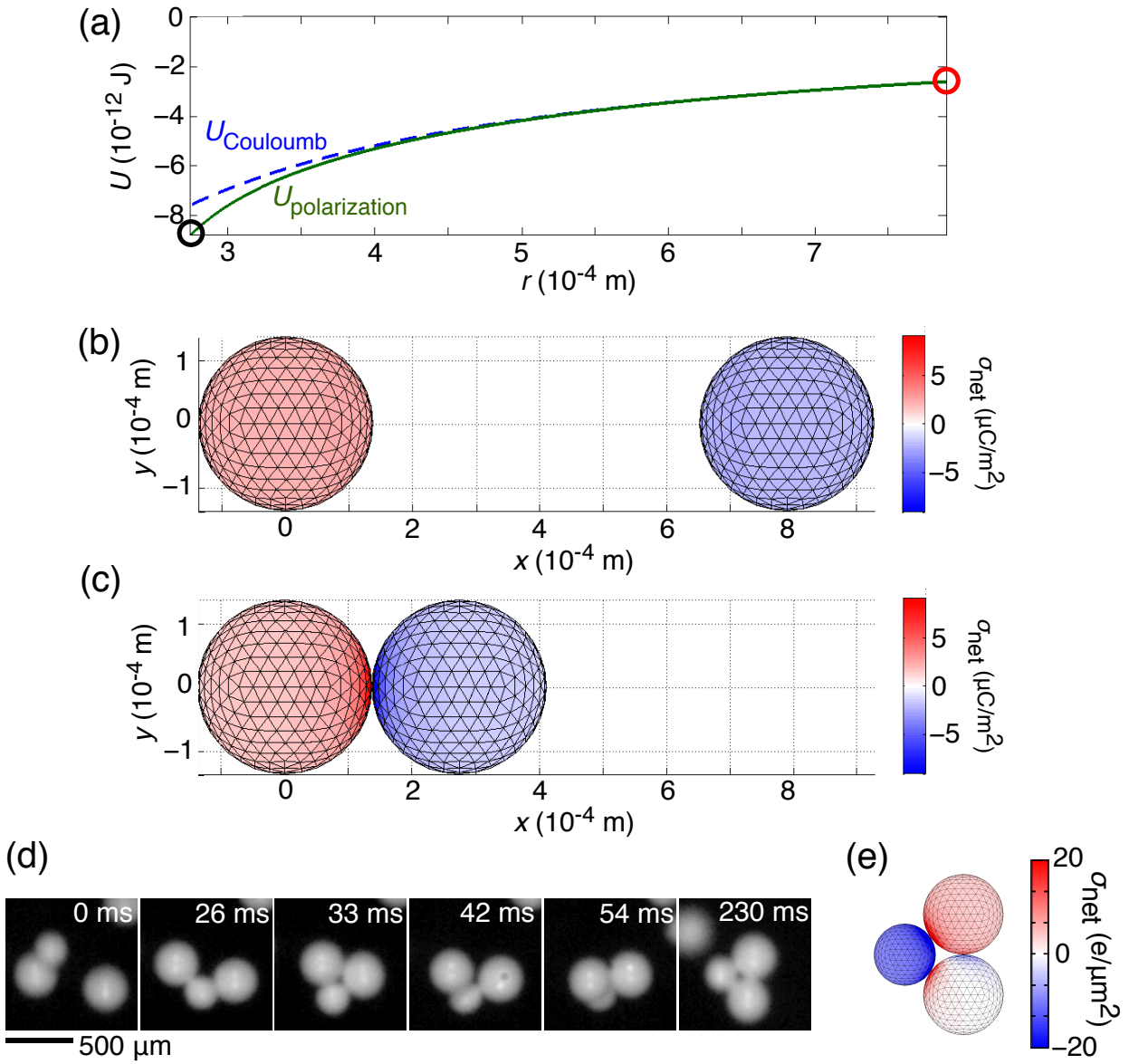

Figure 3.8: (a) Potential energy vs distance between two particles r with ($U_{\text{potential}}$) and without (U_{Coulomb}) taking polarization effects into account. (b)&(c) Induced charges are attractive and become important at close approach. Colour represents the net charge density σ_{net}. Potential energies for (b) and (c) correspond to the data in (a) circled in red and black, respectively. (d) Sequence showing the formation of a triangular molecule from two large positively charged grains and one small negatively charged grain. The closing of the large, visible gap ($t = 42$ ms) between the large particles cannot be explained by short-range sticking and directly implies attractive forces from polarization effects. (e) One of many possible charge assignments that can produce stable triangular molecules from two grains with similar charge magnitude but opposite polarity and one grain of lesser net charge. In this example the charges are $+1.8 \times 10^6$ e and $+0.2 \times 10^6$ e for the large grains, and 2.3×10^6 e for the small grain.

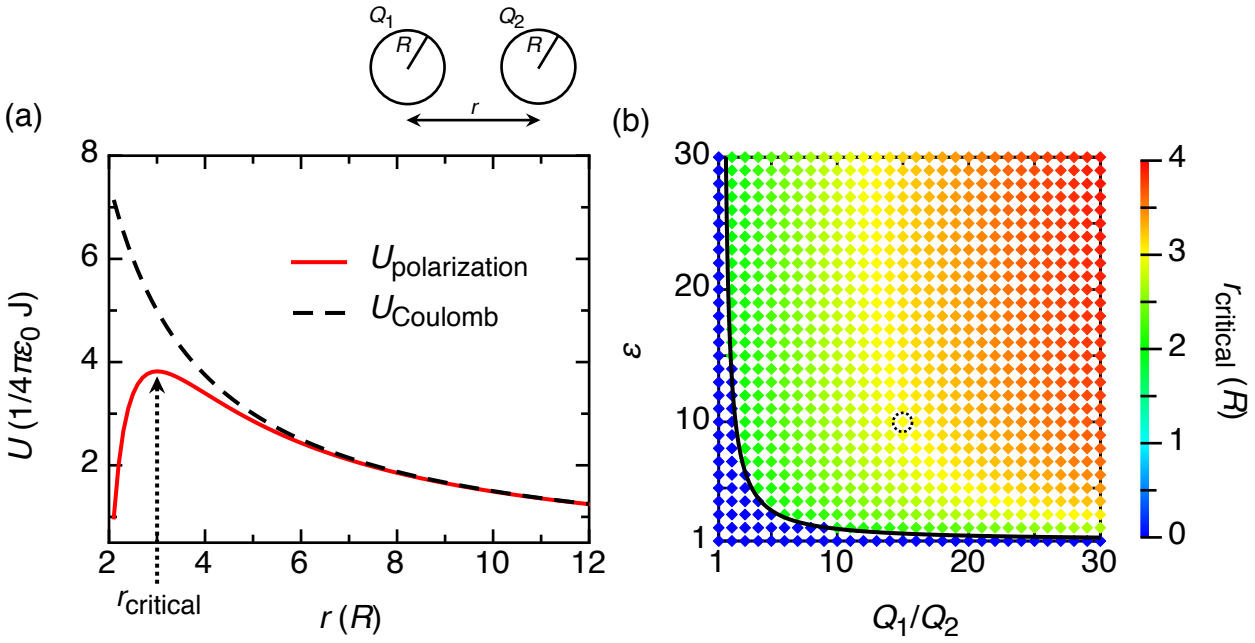

Figure 3.9: Attractive mutual forces between same-polarity grains at close approach. (a) Electrostatic potential energy between two same-polarity grains including the full set of polarization terms $U_{\text{polarization}}$ and the potential energy without the polarization terms U_{Couloub} with particle net charges $Q_1 = 15$ C and $Q_2 = 1$ C and $\varepsilon = 10$. Here $r_{\text{critical}} = 3.005R$ is where the sign of the mutual force turns. R is the radius for both particles. (b) r_{critical} as a function of dielectric constant for the particle material ε and charge asymmetry Q_1/Q_2. The black solid line indicates the minimum required ε and Q_1/Q_2 to have an attractive mutual force at close approach. The circled datum corresponds to the case in (a).

3.4 Summary

These results have implications for a wide range of situations where collision-induced particle aggregation is important. In particular, our results show at the single particle level how long-range electrostatic forces can capture grains whose kinetic energy is orders of magnitude larger than W_{coh}. Multiple bounces enabled by the electrostatic potential well very effectively dissipate kinetic energy, an effect that is further enhanced in $N > 2$ clusters by internal reconfigurations, all of which increases the likelihood of capture and aggregation. Already a very small size dispersion, such as in our nearly monodisperse sample, suffices to generate highly charged particles, an effect likely to become amplified for larger dispersions. Finally, the charge-stabilized granular molecules we observe highlight how intra-cluster particle configurations are controlled by dielectric polarization, an effect of much current interest within the context of self-assembled colloid and ion clusters.

Chapter 4

Hydrophobicity-dependent electrostatic charging of sub-millimeter insulating particles studied with acoustic levitation[1]

4.1 Introduction

Insulating fine particles can acquire a great amount of charge after contact, leading to important consequences in both nature [1–3, 50] and industry [5–7, 59]. However, the underlying mechanism of contact electrification remains elusive. It is still being debated how insulators, which have very low charge mobility, can transfer charge when they are brought into contact [40]. Many mechanisms have been proposed, including the electron-transfer mechanism [18,19], the ion-transfer mechanism [11], and transfer of nanoscale charged material [39].

Interestingly, there appears to be a correlation between the hydrophobicity of nonionic insulators and their charging behavior [11, 118–121]. Hydrophilic insulators such as glass are commonly closer to the top of the triboelectric series, charging positively after contacting other materials. Hydrophobic insulators such as Teflon are usually closer to the bottom of the triboelectric series. Some groups interpreted this correlation as a result of electron transfer [119, 122, 123], proposing that the hydrophobicity of the material depends on its Lewis acid-base property. Since Lewis acids are "electron acceptors" and Lewis bases are "electron donors," this correlation supports the idea that electrons are transferred from Lewis bases to Lewis acids. However, as McCarty and Whitesides point out, "it is not the case that all acids are oxidants or that all bases are reductants," and a Lewis base only shares an electron pair with a Lewis acid instead of transferring electrons [11]. Plus, the ionization

1. In this project, I had the leading role in all parts of the research including the design of the experiments, developing the method of particle charge measurements based on acoustic levitation, performing the particle contact charging experiments, analyzing the data, conducting finite-element and Monte Carlo simulations to compare to experimental data, and preparing the manuscript. This project was supported by the NSF under grant DMR-1309611.

potentials for polymers do not follow their propensity of charging [13], hence making this correlation between hydrophobicity and charging behavior difficult to be rationalized with the electron-transfer mechanism.

Besides electrons, several groups have shown that insulators comprising ionic functional groups constantly develop charge of the opposite sign of the mobile ions in contact charging [24, 25, 27–29], which is explained by the transfer of mobile ions. For nonionic insulators, it has been suggested that aqueous ions of adsorbed water on surfaces may be responsible for the contact charging of nonionic insulators [11]. On one hand, water adsorbed from the atmosphere is ubiquitous. It only takes milliseconds for water molecules to be adsorbed on a surface [124], and it requires baking to get rid of the adsorbed water even in high vacuum [125]. On the other hand, it has been demonstrated that the atmospheric water can enhance the contact charging of insulators [24, 33, 126]. Galembeck and coauthors have also shown that merely varying the relative humidity (RH) changes the charge on a surface without any contact, suggesting that atmospheric water can be the source and sink of charge in solid materials [34, 35, 127]. Studies of electrokinetic measurements and x-ray photoelectron spectroscopy have revealed the accumulation of OH^- ions at solid-water interfaces in hydrophobic insulators [32], hydrophilic self-assembled monolayers [128, 129], ice [130], and metals [131]. Recently, Burgo *et al.* have demonstrated that water is positioned at the top of the triboelectric series [132]; that is, water develops positive charge after flowing over other solid surfaces. Experiments on flow electrification of water done by other groups have also shown the same direction of charge transfer [133–136]. These results can be ascribed to the adsorption of OH^- ions at the solid-water interfaces, which can cause positive charging of water and negative charging of solids.

Although the above studies show evidence in favor of the idea of ion transfer, the mechanism of how ions redistribute themselves during contact electrification of insulators, especially for the charge transfer of insulating grains, is still poorly understood. To better understand the charge transfer mechanism, we need precise charge measurement techniques. Nowadays

the most common techniques for studying the charging of fine particles use Faraday cup-like devices [58, 137, 138], whose precisions that typically give access to a large number of particles' net charge, hindering the interpretation of complex charging phenomena as a result of many collisions. Few experimental techniques are available for making precise measurements of the impact charging of a single sub-millimeter particle [139–142], and those that are available cannot perform charging measurements of a sub-millimeter particle with repeated collisions. It is also difficult to prevent the particles from contacting foreign materials, which can put additional charges onto the samples by contact. Here we develop a new method that involves high-speed videography and acoustic levitation [143–147]—a contact-free and material-independent technique of object manipulation—to study the charging effect of non-ionic insulating particles. This method gives us a very high resolution of *in situ* charge measurement on a single sub-millimeter particle, allowing us to narrow the complex problem of many-particle charging down to repeated charge measurements of a single particle colliding with a target plate. We use this method to test and control the charge transfer by changing the hydrophobicity of material surfaces and the ambient gases and applying external electric fields during particle collisions. We show that hydrophobicity plays an important role in contact charging, which can be explained by a scenario based on the aqueous-ion transfer.

4.2 Experimental Setup

In the particle charge measurements, we suspended a sub-millimeter glass particle in the ambient gas with acoustic levitation. Then we used electric fields to drive the levitated particle and obtained the particle charge (q) from the response of the particle to the electric fields. To study the charge transfer during particle collisions, we made the particle collide with a target plate underneath. A short sound-modulating pulse ($\sim$12 ms in pulse width) was used to temporarily switch off the acoustic levitation. When the acoustic levitation was switched off, the particle dropped due to gravity, hit against the target plate below, and bounced. After the bounce, the acoustic levitation was quickly turned on again and the

particle was trapped at the equilibrium point, ensuring that there was only one collision per drop. During the collision, the particle exchanged charges with the target plate. Then we applied an AC electric field to the levitated particle to measure q again. This routine could be repeated under computer control. The experiments of acoustic levitation were conducted at 40% RH inside a chamber injected with an adjustable mixture of dry nitrogen gas and nitrogen gas saturated with water vapor unless otherwise stated.

The experimental setup is shown in Fig. 4.1(a). A function generator and a high voltage amplifier provided the driving voltage signal for a sound transducer (Hesentec Rank E) that generated ultrasound at a frequency of approximately 146.5 kHz. A flat target plate underneath the transducer acted as a reflector of sound. When the distance between the transducer and the sound-reflecting target plate was an integer multiple of the half wavelength of sound ($\lambda/2$), a standing sound wave could be established, and a sub-millimeter particle could be trapped at the pressure node. To have a horizontally localized standing wave, we drilled a cylindrical hole (800 μm in diameter, 125 μm deep) on the flat surface of the transducer and adjusted the distance between the ceiling of the hole and the target plate to $\lambda/2$ (≈ 1.2 mm). For a spherical particle with radius R much smaller than λ ($R/\lambda < 0.1$), the acoustic potential (U) was derived by Gor'kov [148]:

$$U = 2\pi R^3 \left(\frac{\langle p^2 \rangle}{3\rho c^2} - \frac{\rho \langle v^2 \rangle}{2} \right), \tag{4.1}$$

where ρ is the density of the gas, c is the speed of sound, $\langle p^2 \rangle$ and $\langle v^2 \rangle$ are the mean square amplitudes of the acoustic pressure and velocity of the gas. Figure 4.1(b) shows the dimensionless acoustic potential ($\tilde{U}$) in our setup simulated with COMSOL Multiphysics 5.2, where $\tilde{U} = U/(\pi R^3 \rho v_0^2)$ with v_0 the maximum acoustic velocity. The particle could be trapped at the equilibrium point of gravity and the acoustic radiation force $\mathbf{F}_a = -\nabla U$. The acoustic velocity potential for a standing sound wave along the vertical axis (y-axis) is given by [149]

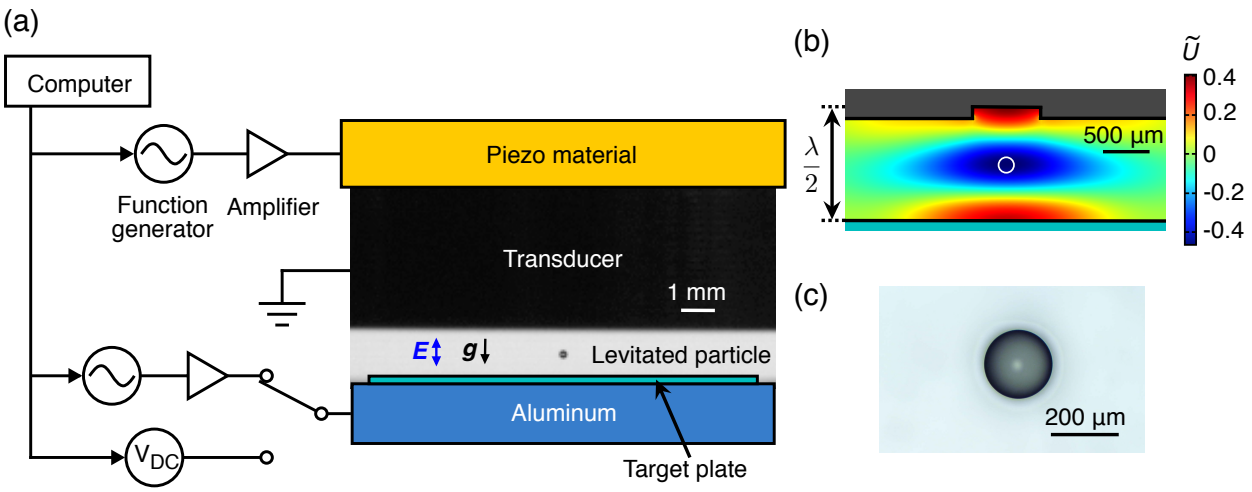

Figure 4.1: Particle charge measurement with acoustic levitation. (a) Experimental setup. A sub-millimeter particle is acoustically levitated between a grounded ultrasonic transducer and a sound-reflecting target plate. A piece of aluminum underneath the target plate is connected to an AC or a DC voltage source. The particle was backlighted and filmed from the side with a high-speed camera. Not shown here are the high-speed camera and an ambient gas-controlled chamber that contains the system of acoustic levitation. (b) Side-view cross section of the dimensionless acoustic potential ($\tilde{U}$) simulated with COMSOL Multiphysics 5.2. The white circle illustrates the approximate size and position of a levitated particle. (c) Microscope image of a glass particle.

$$\phi = -\frac{v_0}{k}\cos(ky)\sin(\omega t), \tag{4.2}$$

where $k = 2\pi/\lambda$ is the wave number and $\omega = kc$ is the angular frequency of sound. This leads to acoustic pressure and velocity for the standing sound wave along the y-axis

$$p = -\rho\frac{\partial\phi}{\partial t} = \rho c v_0 \cos(ky)\cos(\omega t) \tag{4.3}$$

and

$$v = \frac{\partial\phi}{\partial y} = v_0 \sin(ky)\sin(\omega t). \tag{4.4}$$

From Eqs. (4.1), (4.3), and (4.4), we can obtain the acoustic radiation force along the y-axis

$$F_{ay} = -\frac{\partial U}{\partial y} = \frac{5}{6}\pi R^3 \rho v_0^2 k \sin(2ky). \tag{4.5}$$

The strong acoustic radiation forces allowed us to directly lift up the sub-millimeter particle from the target plate before applying any electric field across the particle. Figure 4.2(a) shows the lifting of a particle with vertical position y as a function of time. After lifted, the particle oscillated in the acoustic potential about its equilibrium point (just below $y = \lambda/4$) and experienced damping forces from air drag. The amplitude of oscillation can be fitted into an exponential decay with a decay constant $\beta \approx 2.4$ Hz, which is correct presumably only for the particle size and mass in this experiment. The levitated particle was filmed from the side by a high-speed camera (Phantom v12; 1000 frames per second) with backlight illumination. The position of the particle was tracked with an algorithm developed by Crocker and Grier [79].

To measure the net charge q on the particle, we applied AC and DC electric fields across the levitated particle and tracked the particle motion in response to the electric fields. The surface of the transducer was grounded. An aluminum piece underneath the target plate was connected to either a set of a function generator and an amplifier or a high-voltage bipolar

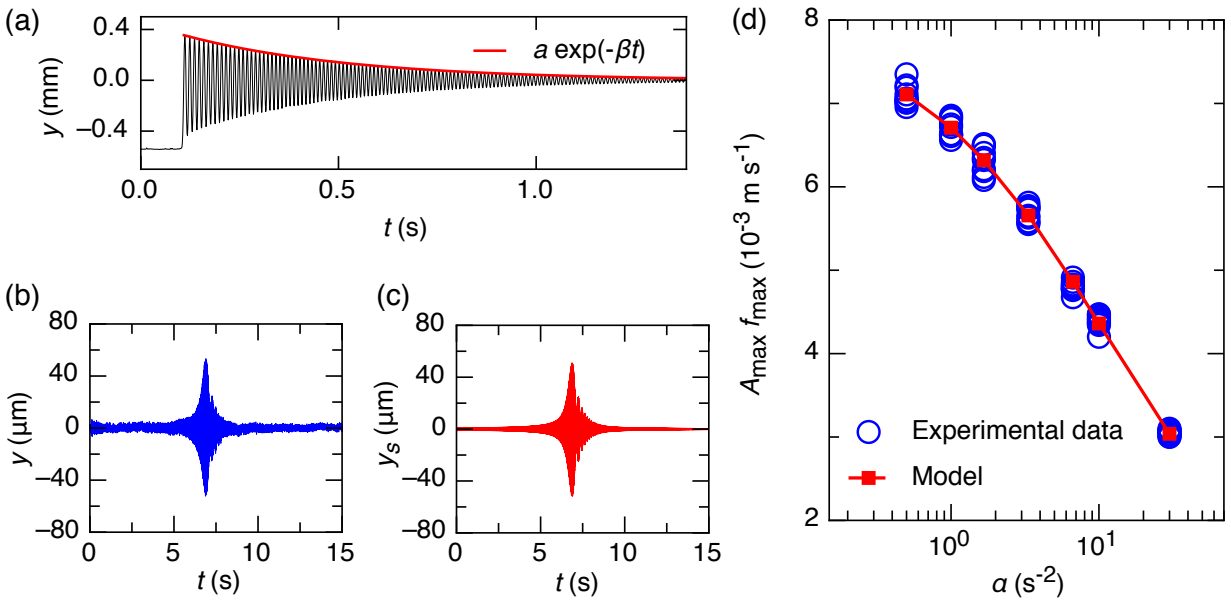

Figure 4.2: (a) Vertical position (y) of a particle levitated from a plate without electric fields vs. time t (black line) and a fit of an exponential decay (red line). (b)&(c) Experimental data y (b) and model y_s (c) for the vertical position of a levitated particle in a frequency-swept AC electric field vs. t. (d) Comparison between the experimental data and the model for the product of the maximum amplitude of oscillation A_{max} and the resonance frequency f_{max} vs. frequency sweeping rate α. The experimental data are measured with the same levitated particle without any collisions.

DC power supply, switched by a computer-controlled relay, providing AC or DC electric fields across the levitated particle in the vertical direction.

We used an AC electric field to make the levitated particle oscillate due to Coulomb forces to measure the charge magnitude ($|q|$). The particle can be resonated when the frequency of the AC electric field matches the resonance frequency of the levitated particle (f_{max}). This resonance gives us high resolution of particle charge measurement. In order to find out f_{max} to achieve the resonance, we applied an AC electric field with a linear frequency sweep across the levitated particle. If the frequency of the AC field went through f_{max}, the particle would experience a pulse-like oscillation, which is a signature of experiencing a resonance. Figure 4.2(b) shows an example of the observed y versus time (t) in response to the frequency-swept (from 50 Hz to 150 Hz in 15 seconds) AC electric field. The particle exhibited a pulse-like resonance. To obtain the amplitude and frequency of oscillation, it is useful to express $y(t)$ in the form of the analytic signal ($Y(t)$), which is

$$Y(t) = y(t) + i\tilde{y}(t) = A(t)e^{i\varphi(t)}, \tag{4.6}$$

where $\tilde{y}(t)$ is the Hilbert transform of $y(t)$ defined by [150]

$$\tilde{y}(t) = \hat{H}[y(t)] = \frac{1}{\pi}\int_{-\infty}^{\infty}\frac{y(\tau)}{t-\tau}d\tau. \tag{4.7}$$

The instantaneous amplitude $A(t)$ and frequency $f(t)$ of $y(t)$ can be obtained by

$$A(t) = |Y(t)| = \sqrt{y^2(t) + \tilde{y}^2(t)} \tag{4.8}$$

and

$$f(t) = \frac{1}{2\pi}\frac{d\varphi(t)}{dt}, \tag{4.9}$$

where $\varphi(t)$ is the instantaneous phase angle, given by

$$\varphi(t) = \arctan\left(\frac{\tilde{y}(t)}{y(t)}\right). \tag{4.10}$$

In Fig. 4.3, we plot the zoomed-in data of $y(t)$ in Fig. 4.2(b) and its corresponding $A(t)$ and $f(t)$. We define the maximum amplitude of oscillation A_{max} to be the maximum point of $A(t)$ at $t = t'$, and the resonance frequency f_{max} to be its corresponding instantaneous frequency ($f_{max} = f(t')$). In principle, the instantaneous frequency can also be obtained by fitting the discrete $y(t)$ data into sine functions. However, fitting the data is computationally much more time-consuming than using the Hilbert transform. With the Hilbert transform, we can efficiently obtain $A_{max} \approx 52$ μm at $f_{max} \approx 93$ Hz at $t \approx 6.9$ s for $y(t)$ in Fig. 4.2(b).

The equation of motion of the particle along the y-axis can be expressed as

$$m\ddot{y} + 2m\beta\dot{y} = F_{ay} - mg + |q|E_0 \sin(\omega_E(t)t), \tag{4.11}$$

where m is the particle mass, $2m\beta\dot{y}$ is the air drag on the particle, mg is the force of gravity, E_0 and $\omega_E(t) = 2\pi(\alpha t/2 + f_i)$ are the amplitude and sweeping frequency of the AC electric field across the levitated particle, α is the frequency sweeping rate, and f_i is the initial frequency of electric field. We computed m with the material density by measuring the particle size with an optical microscope (Fig. 4.1(c)). β was obtained by fitting the attenuating amplitude of oscillation into an exponential decay as in Fig. 4.2(a). E_0 was simulated with COMSOL in consideration of the hole on the transducer surface and the target plate. Eq. (4.5) can be expressed with a fitting parameter F_{a0} as

$$F_{ay} = \frac{5}{6}\pi R^3 \rho v_0^2 k \sin(\frac{4\pi y}{\lambda}) \equiv F_{a0} \sin(\frac{4\pi y}{\lambda}). \tag{4.12}$$

With a given set of $|q|$ and F_{a0}, a simulated trajectory $y_s(t)$ can be generated by numerically solving Eq. (4.11). From $y_s(t)$, we can obtain the corresponding maximum amplitude of

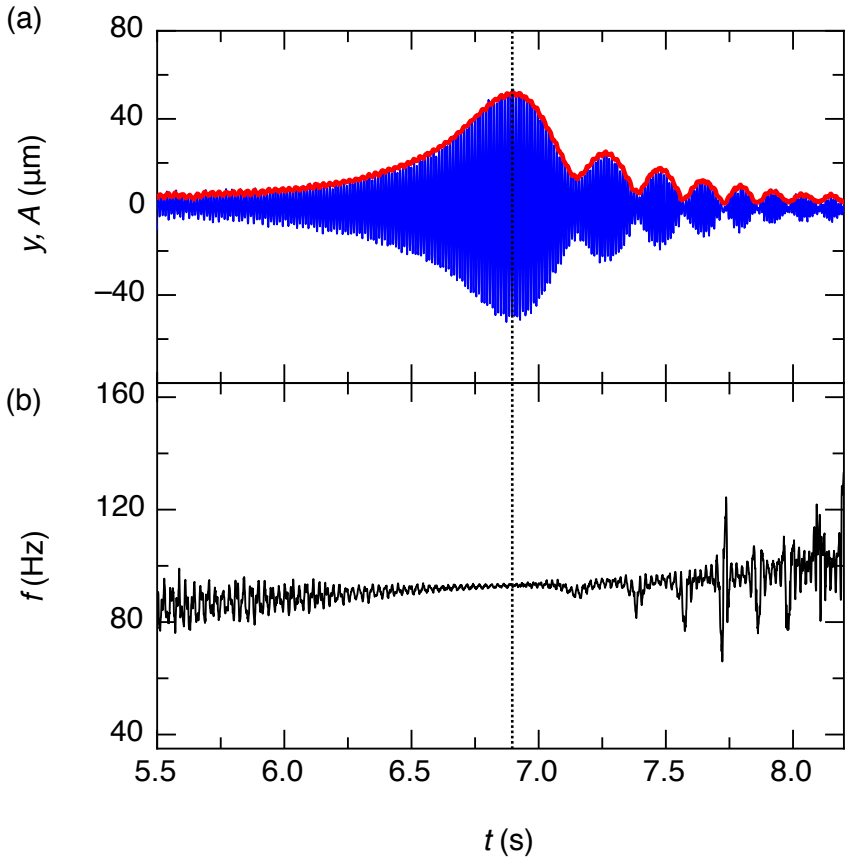

Figure 4.3: Instantaneous amplitude and frequency obtained from the Hilbert transform. (a) Zoomed-in data of $y(t)$ from Fig. 4.2(b) (blue line) and its instantaneous amplitude $A(t)$ (red line). (b) Instantaneous frequency $f(t)$ of $y(t)$ in (a). The vertical dotted line indicates the time t' when $A = A_{max}$ and $f = f_{max}$.

oscillation A'_{max} and the resonance frequency f'_{max} of the simulated trajectory with the Hilbert transform. We used a Nelder-Mead simplex algorithm [114] as the multidimensional optimization method with the parameters $|q|$ and F_{a0} to search for the minimum of squared relative error between the simulated and the experimental results of A_{max} and f_{max}, which is described by

$$\delta = \left(\frac{A'_{max} - A_{max}}{A_{max}}\right)^2 + \left(\frac{f'_{max} - f_{max}}{f_{max}}\right)^2. \tag{4.13}$$

From the fitting, a set of A_{max} and f_{max} from the experiment led to a single set of $|q|$ and F_{a0}, and we made sure that δ became less than 10^{-7} for each fitting. We hence obtained the charge magnitude $|q|$ for the experiment. Based on Eq. (4.11), $|q|$ scales as m/E_0. As a result, the uncertainty of measured charge magnitude ($\Delta|q|$) is smaller with a larger applied E_0. During experiments we used AC electric fields with the range of 3.3×10^3 V/m $< E_0 < 1.6 \times 10^5$ V/m, rendering the range of charge precision, in units of elementary charges (e $= 1.6 \times 10^{-19}$ C), 1×10^3 e $\lesssim \Delta|q| \lesssim 6.5 \times 10^4$ e. We prevented the particle from colliding with the transducer or the target plate during the charge measurements when $|q|$ is large by choosing a small enough E_0. Figure 4.2(c) shows the fitted numerical solution compared to Fig. 4.2(b), and as shown in Fig. 4.2(d), the model fits the experimental data of $A_{max}f_{max}$ well with all the same fitted $|q|$ and F_{a0} but different α. The smaller $A_{max}f_{max}$ for a larger α is presumably due to a shorter time for the particle to be in/near resonance. The polarity of the particle net charge was determined by applying a DC electric field pointing up or down on the levitated particle, which moved to a higher or lower equilibrium point depending on its polarity.

The samples we used were borosilicate glass particles (density $\rho_p = 2200$ kg/m^3, 204 ± 8 μm in diameter, Cospheric) and borosilicate glass target plates (Catalog no. 12-542B cover slide, 22 mm $\times$ 22 mm, 0.15 ± 0.02 mm thick, Fisher Scientific). Before the experiments, the samples were cleaned in an ultrasonic bath of acetone, ethanol, and DI water for one hour each, and dried in a vacuum chamber with an oil-free pump. To test the effect of hydrophobicity of insulators on particle charging, we made originally hydrophilic borosilicate

glass particles or glass plates hydrophobic by attaching nonpolar groups ($-CH_3$) onto the glass surfaces via silanization (Fig. 4.4(a)). The silanization was done by immersing the glass particles and cover slides in a solution of NaOH:H_2O:ethanol = 1:2:2 by weight for one hour, washing with ethanol, and drying at 60°C for 12 hours. The glass particles and plates were then immersed in a solution of ethanol:$(CH_3)_3SiCl$ (Sigma-Aldrich) = 10:1 by weight for 8 hours, washed with ethanol, and dried in a desiccator.

4.3 Results and discussion

Charging of hydrophilic and hydrophobic particles

We plot examples of q of a levitated particle colliding with a target plate versus the number of collisions N in Fig. 4.4(b). For the cases of charging between similar surfaces (hydrophilic glass vs. hydrophilic glass and hydrophobic glass vs. hydrophobic glass), the charging is relatively small compared to the ones between dissimilar surfaces. For a hydrophilic glass particle colliding with a hydrophobic glass plate, the particle accumulated significant positive charges (charging rate $dq/dN \approx +6600$ e/collision). Instead, a hydrophobic glass developed substantial negative charges by colliding with a hydrophilic glass plate ($dq/dN \approx -6400$ e/collision). When the particle charge becomes as high as $|q| \approx 4 \times 10^6$ e, the attractive electrostatic force between the particle and the target plate is higher than the acoustic force during levitation, so the particle becomes stuck to the target plate after bouncing. Here we show that the charging behavior of glass material can be altered significantly by changing the surface properties: after contact, the hydrophilic glass charges positively and the hydrophobic glass charges negatively.

McCarty and Whitesides suggest that the contact charging between nonionic insulators in general might be due to the transfer of OH^- ions in the adsorbed water on the surfaces of insulators [11]. Experimental studies have shown that water adsorbed on solid surfaces may not form a continuous film of water but individual water islands even for a hydrophilic material like mica [151]. The sizes of the water islands are found to be from tens of nanome-

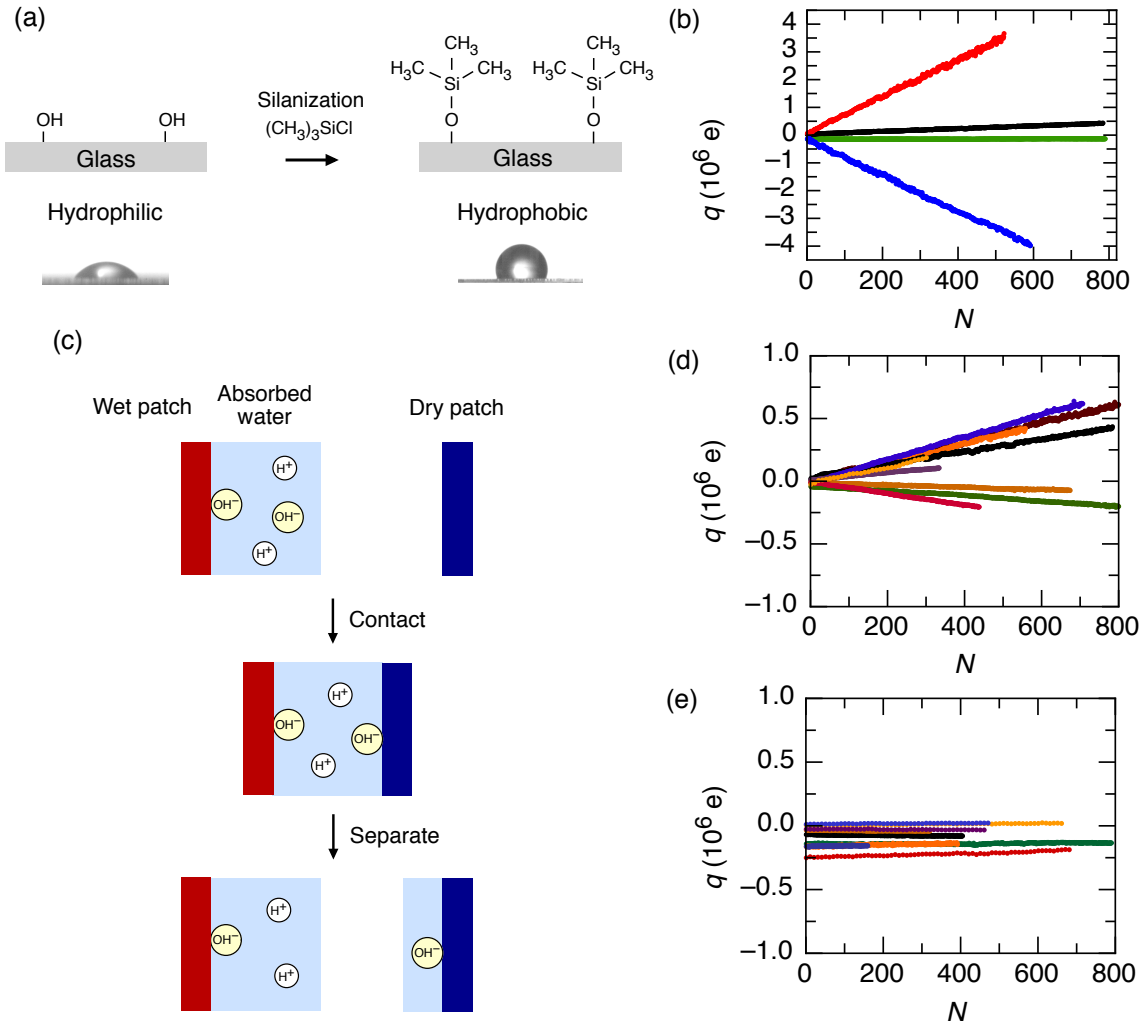

Figure 4.4: Charge transfer between glass surfaces. (a) Glass surface silanized with trimethylchlorosilane $(CH_3)_3SiCl$. The contact angles between a water drop and the glass plate before and after silanization were $50 \pm 3^\circ$ and $110 \pm 3^\circ$, respectively. (b) Examples of particle charge q vs. the number of particle-plate collisions (N) for a hydrophilic glass particle vs. a hydrophobic glass plate (red), a hydrophobic glass particle vs. a hydrophilic glass plate (blue), a hydrophilic glass particle vs. a hydrophilic glass plate (black), and a hydrophobic glass particle vs. a hydrophobic glass plate (green). Note that in experiments of red and blue curves, we used a lower amplitude of AC electric field (3.3×10^3 V/m) to prevent the highly charged particles from colliding with the transducer or the target plate surface during the field-driven oscillations, resulting in a higher statistical error of particle charge measurements. (c) Possible mechanism of charge transfer between a wet patch on a surface and a dry patch on another surface. (d)&(e) Different trials of q vs. N for (d) a hydrophilic glass particle vs. a hydrophilic glass plate and (e) a hydrophobic glass particle vs. a hydrophobic glass plate.

ters to over a micron at 40% RH, and the coverage of water layer is ∼50% at 40% RH and not 100% complete even at 90% RH.

Based on this, we suggest a possible scenario for the charge transfer between nonionic insulators with different hydrophobicity due to different amounts of adsorbed water. This is sketched in Fig. 4.4(c). When an adsorbed water island (wet patch) on one surface contacts an area without water molecules (dry patch) on another surface, an OH^- ion will be transferred and adsorbed onto the dry patch. This scenario is based on molecular-dynamics simulations [31], which showed that OH^- ions tend to be localized at solid-water interfaces. Therefore, there can be more OH^- ions than H^+ ions accumulating on the originally dry surface, leading to net negative charge transfer after separation. Recent experimental results have shown that solid materials tend to get negative charges after contacting water [132], supporting the idea of OH^- adsorption at the solid-water interfaces. For hydrophilic nonionic insulators, water molecules are adsorbed from the atmospheric moisture due to the formation of strong hydrogen bonds [152]. On the other hand, although hydrophobic insulators can still adsorb water due to ubiquitous dispersion forces [152,153], the forces are much smaller than the hydrogen bonds, which can lead to larger dry areas on its surface. The net charge transfer may hence be determined by the different coverage of water islands between two contacting surfaces. The water predominantly from the hydrophilic insulator may be the source of OH^- ions and leave negative charges on the surface of hydrophobic insulator after separation. Another factor of charge transfer may be that the hydrophobic insulator can have a higher affinity for OH^- ions, leading to higher OH^- ions adsorption on the hydrophobic surface compared to the hydrophilic one. This explanation is based on electrokinetic studies, where it is shown that the zeta potential is generally more negative with increasing hydrophobicity [130,154,155]. It is probably because the adsorption of OH^- ions at the solid-water interface is competing with the adsorption of water molecules.

Figure 4.4(d) shows different trials of charge transfer measurements for a hydrophilic glass particle colliding with a hydrophilic glass plate. We observed both directions of charge

transfer, and the particles charged up in a linear way. The charging rate ranges from $dq/dN = -460$ to 897 e/collision. The non-zero charging rate may result from slightly different surface properties between surfaces of particles and target plates. Although the materials are both borosilicate glass, they are not strictly identical due to different manufacturers. There could also be some differences between each glass particle and glass plate, resulting in both positive and negative charging rates observed. However, as shown in Fig. 4.4(e), the charging rate is much smaller for a hydrophobic particle colliding with a hydrophobic glass plate (dq/dN ranges from -26 to 80 e/collision), which is probably because the same kind of nonpolar groups is attached to the surfaces of glass particles and target plates, minimizing the differences in surface properties. An additional reason is that the transferable ions can be less on the hydrophobic surfaces, rendering the smaller charge transfer.

In situ contact charging measurements of other groups have shown that charge on surfaces should eventually saturate after many contacts when the transferable charges are depleted or exhibit rapid discharge events when the charge per unit surface area is high enough [16,27,49]. However, the result in Fig. 4.4 that no sign of charge saturation is observed up to $|q| = 4\times10^6$ e suggests that q is in a linear regime where the charge transfer is not affected by the charging history of the particle. It is likely that the number of transferable charges is much larger than the number of charges that have been transferred. Plus, in our experiments of acoustic levitation, some oscillational instability caused by time delays on the response of the acoustic forces to the particle motion could occur and make the particle rotate continuously [156]. Therefore, different spots on the particle could contact the target plate each time. With a maximum contact area (A_c) during particle collisions of $\sim$20 μm^2 in our experiments (see Appendix D) and a total particle surface area of $\sim1.3\times10^5$ μm^2, we estimate that the average number of collisions per individual patch is still small ($\sim$0.15) even at 1000 collisions. The highly linear $q(N)$ dependence we found in all cases thus demonstrates that any wet and dry patches must have been much smaller than 20 μm^2, so that the particle surfaces appeared homogeneous when averaged over the contact area.

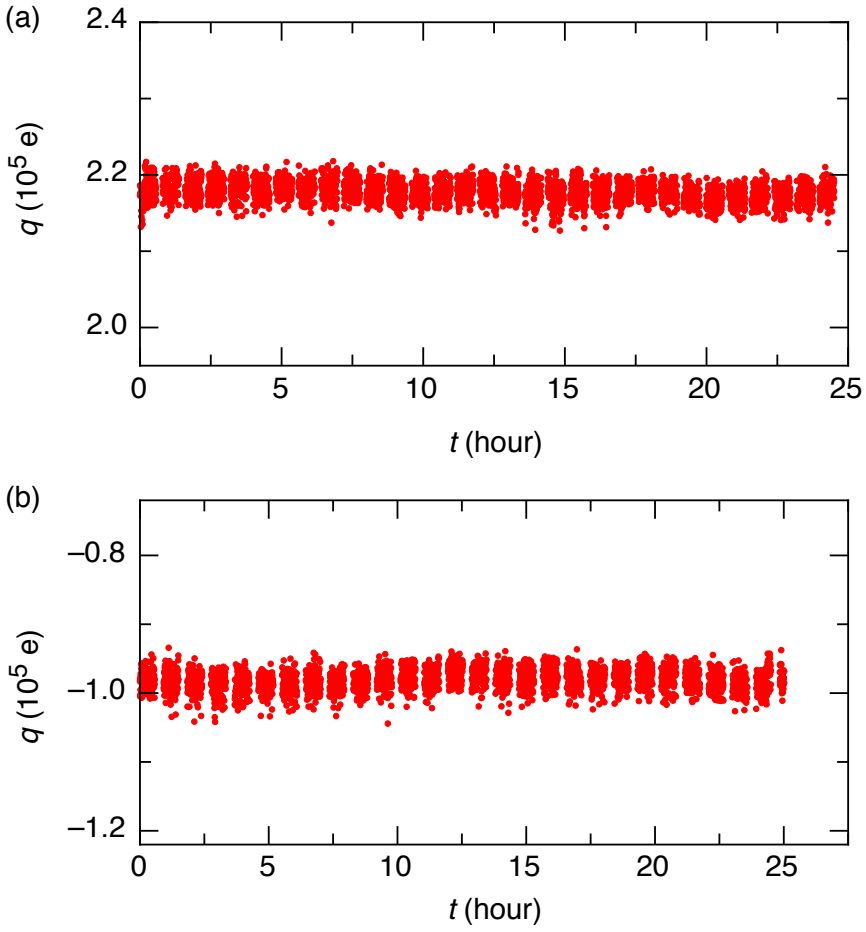

Figure 4.5: Examples of charge q on (a) a hydrophilic glass particle and (b) a hydrophobic glass particle levitated in nitrogen gas at 40% RH vs. time t. The gaps of charge measurements in t are the time required for saving high-speed video files.

To see the effect of the ambient nitrogen gas on the charge q of the particles, we levitated hydrophilic and hydrophobic glass particles and repeatedly measured q without any collisions for $\sim$25 hours (for example, Fig. 4.5), larger than the amount of time spent in our experiments of repeated particle collisions (typically less than 6 hours). No detectable charge transfer between the ambient gas and the levitated particles was found.

Particle charging in acidic/basic atmospheres

If the contact charging is indeed due to OH^- ions, then changing the ambient atmosphere should alter the amount of ions dissolved in the adsorbed water layers and thus influence the amount of charge transfer per collision. To test this, we changed the ambient atmosphere by introducing acidic or basic vapors to the experimental chamber. These vapors were prepared by bubbling nitrogen gas into 1 M aqueous solutions of acetic acid and ammonia, respectively. The atmosphere in the chamber was stabilized for two hours before each experiment.

In Fig. 4.6, we plot the charging rate of a hydrophobic particle colliding with a hydrophilic glass target plate as a function of relative humidity in acidic, basic, and neutral environments. All the hydrophobic particles charged negatively after contacting hydrophilic target plates over the range of RH studied (10-50% RH). The negative charging rate of the particle in a basic atmosphere is enhanced compared to a neutral atmosphere, while it is suppressed in an acidic atmosphere. This makes sense in light of electrokinetic studies, which showed that OH^- and H^+ ions have a much stronger affinity than other electrolyte ions for hydrophobic surfaces [32, 128, 130, 154], whereas acetate and ammonium ions behave indifferent [157–159]. Thus, the enhancement and suppression of the charging rate in the basic and acidic environments can be attributed to different numbers of OH^- ions dissolved in the adsorbed water, which are the ions predominantly transferred from a hydrophilic to a hydrophobic surface during contact.

Our experiments could only go to RH values around 50%. Controlled levitation-collision sequences become difficult to perform with larger humidity due to the increasingly strong

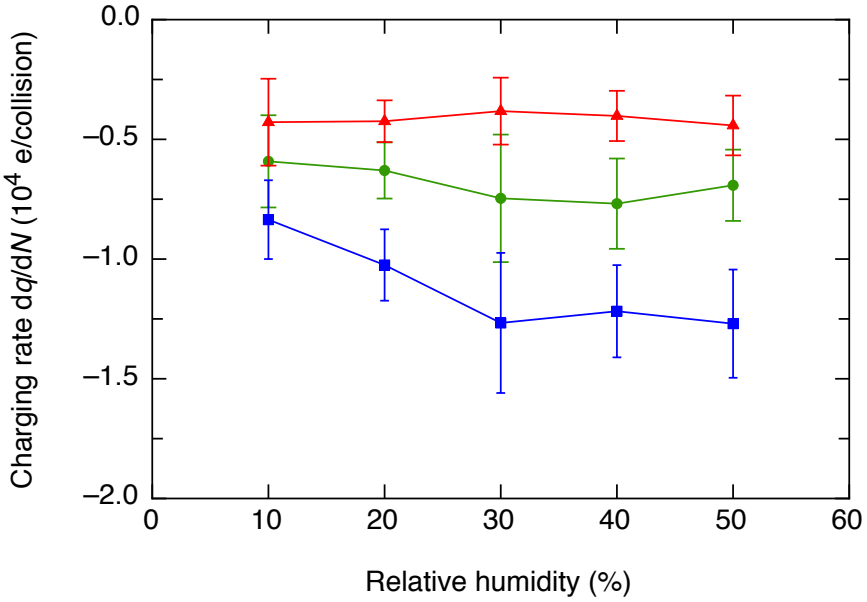

Figure 4.6: Charging rate (dq/dN) for a hydrophobic glass particle colliding with a hydrophilic glass target plate vs. relative humidity in acidic (red triangle), neutral (green circle), and basic (blue square) atmospheres.

capillary forces between particle and target plate. While the data in Fig. 4.6 stays relatively flat up to 50% RH, larger humidity eventually will let charge leak away by increasing the conductivity. Previous studies showed, however, that charging of hydrophobic particles does not decrease until 60% RH is reached [160, 161].

Besides the impurity ions from the ambient atmosphere, it cannot be excluded that ions from substrates are involved as well. For example, glass materials contacting water are known to leach out ions through the ion exchange between the alkali ion from the glass and the H^+ ion in [162–164]. This effect may lead to a decrease in H^+ ions and thus an increase of the pH of water [164]. Hence, charging may be enhanced due to a larger number of OH^- ions in the adsorbed water. However, further investigation of the ion leaching in the adsorbed water on grass surfaces is needed to obtain the charge transfer contribution of the impurity ions from substrates.

Particle charging controlled by electric fields

Based on the scenario that ions in adsorbed water can lead to contact charging, applying an external electric field to the contacting surfaces can change the distribution of ions thus the amount of charge transferred. In our setup we can explore this straightforwardly by applying a DC electric field during particle collisions. Figure 4.7(a) shows q of a hydrophilic glass particle colliding with a hydrophilic glass target plate in a DC electric field $E = \pm 8 \times 10^5$ V/m pointing up (to the particle) or down (to the target plate) as a function of N. The particle started negatively charged, and became less negative when colliding in an electric field pointing up. Then q went through zero and became more positive. The direction of charge transfer for a particle was not affected by its own net charge polarity. Yet, sharp transitions of charging rate were observed after changing the direction of the electric field. The particle charged negatively when the electric field pointed down, and it charged positively again when the direction of the electric field was up. Other groups have also observed particle charging induced by electric fields [56, 165], but the *kinetics* of how a single particle gets

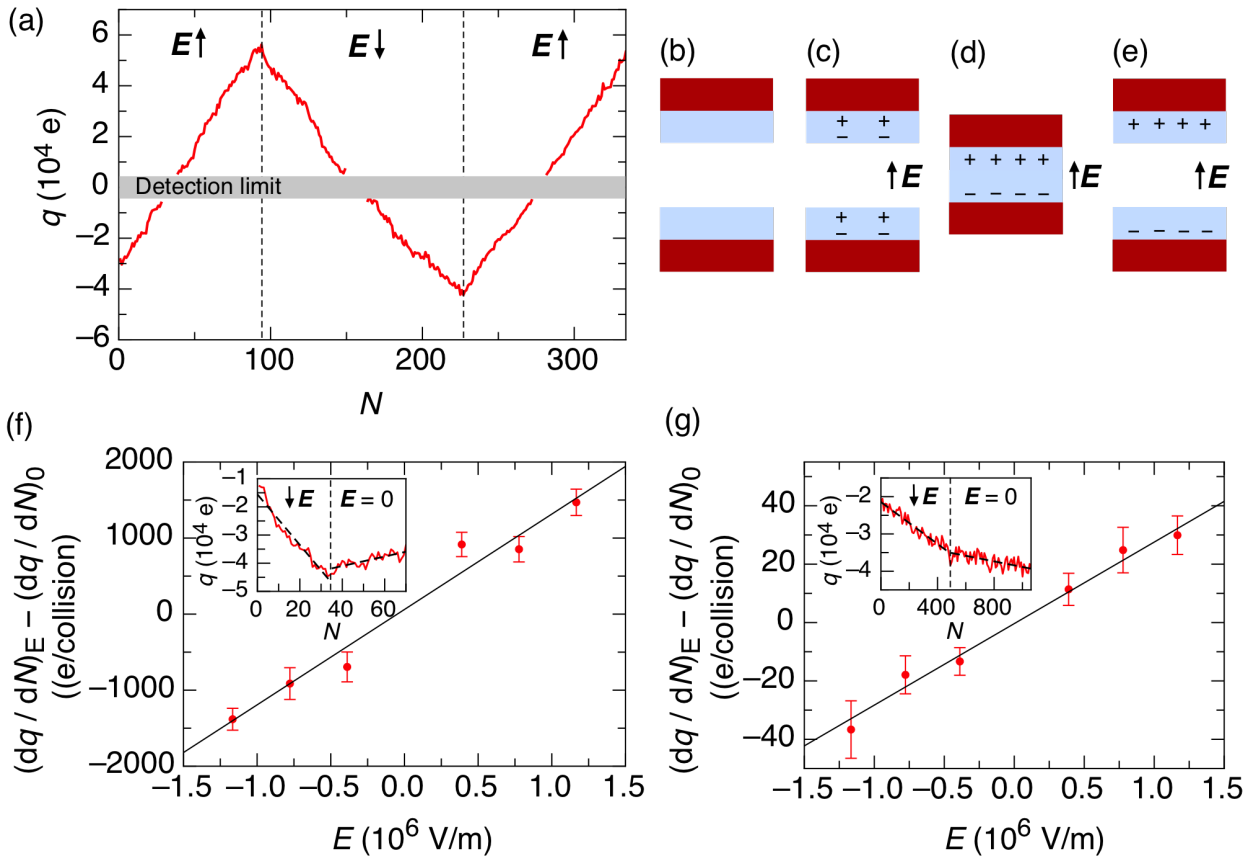

Figure 4.7: Field-induced particle charging. (a). Charge (q) on a hydrophilic glass particle colliding with a hydrophilic glass target plate in an electric field pointing up or down ($E = \pm 8 \times 10^5$ V/m) as a function of the number of collisions. (b)-(e) Possible charging mechanism of two surfaces contacting in an electric field. (f)&(g) Charging rate in an electric field minus the charging rate in no electric field vs. the electric field (E) for (f) a hydrophilic glass particle colliding with a hydrophilic glass target plate and for (g) a hydrophobic glass particle colliding with a hydrophobic glass target plate. Insets show particle charge (q) vs. the number of collisions (N) with an electric field ($E = -8 \times 10^5$ V/m) or without any field for the cases of (f) a hydrophilic glass particle against a hydrophilic glass target plate and (g) a hydrophobic glass particle against a hydrophobic glass target plate.

charged repeatedly due to an electric field has not been demonstrated. Here we clearly show that the direction of charge transfer can be controlled by electric fields. The detection limit is from the difficulty of detecting A_{max} and f_{max} with the existence of small particle oscillation with an amplitude of $\sim$3 μm in acoustic levitation. In these experiments, the acceleration of a particle in an electric field is controlled to be less than $\sim$0.7 m/s^2 by stopping the test before the acceleration is too large. The *maximum* acceleration will cause $\sim$3% change of impact velocity ($V_{imp} = \sqrt{2gh} \approx 0.11$ m/s when no electric field is applied) and $\sim$3% change of the maximum contact area during a collision A_c ($\sim$20 μm^2).

We can explain the observed field-induced charging by considering the migration of ions due to the external electric field when, during particle collisions, the two contacting surfaces are brought into contact. For contact between two wet patches, no net charge transfer happens without a field; however, with an applied field, ions of different polarity migrate across the interface in different directions, inducing a field-controlled net transfer of charge after separation, as illustrated in Fig. 4.7(b)-(e). Similarly, when a wet and a dry patch collide (see Fig. 4.4(c)), the applied field drives OH^- ions in the wet patch either towards or away from the interface with the dry patch and thus controls the amount of charge transfer. For the contact between two dry patches, no ions will be transferred.

As before when $E = 0$ during collisions, no obvious sign of saturation of the particle charge is seen in Fig. 4.7(a). This again is because of particle rotation, so that, at least up to the collision numbers N tracked in our experiments, different spots of the particle hit the target plate. Therefore, for each collision new patches are brought into contact and contribute to the field-induced charge transfer. In addition, if we assume uniform charge distribution on the particle, the electric field $(1/4\pi\epsilon_0)(q/R^2)$ due to the charge buildup is no larger than 8×10^3 V/m for the data in Fig. 4.7(a). This is two orders of magnitude smaller than the external applied electric field $E = 8 \times 10^5$ V/m. Therefore, the built-up particle charge is unlikely to affect the collisional charging, and the external electric field still dominates the charge transfer.

Figure 4.7(f) shows the charging rate of a hydrophilic glass particle colliding with a hydrophilic glass target plate driven by the electric field $(dq/dN)_E - (dq/dN)_0$ versus E, where $(dq/dN)_E$ is the charging rate for a particle colliding in a DC field and $(dq/dN)_0$ is the charging rate for the same particle and target plate without the field. A linear relationship between $(dq/dN)_E - (dq/dN)_0$ and E is observed, and the slope of the linear fit is $1.25 \times 10^{-3} \pm 8 \times 10^{-5}$ (e/collision)/(V/m).

We simulated the charge transfer due to polarization of the water bridge between a glass particle and a glass plate in an external electric field with COMSOL. As shown in Fig. 4.8(a), the simulation contains a 204 μm diameter glass particle and a 150 μm thick glass plate with dielectric constant $\kappa = 4.6$ for borosilicate glass [166], connected by a water bridge ($\kappa = 80.1$ at 20°C [167]). The water bridge is approximated as a cylinder with base area of 20 μm^2 and height H. The glass particle, the water bridge, and the glass plate are in between a grounded conductive surface with a cylindrical hole (800 μm in diameter, 125 μm deep) and a conductive surface with a constant potential of 1000 V. The distance between the ceiling of the hole and the glass plate is 1.2 mm, giving an average external electric field $E = 8 \times 10^5$ V/m. The surface bound charge of water at the solid-water interface (Q) can be obtained by integrating the normal component of the polarization ($\mathbf{P}$) in the water bridge over the solid-water interface ($Q = \int \mathbf{P} \cdot \hat{\mathbf{n}} dS$). The thickness of the water bridge between the glass surfaces is assumed to be on the order of a few nanometers as the thickness of the water layer adsorbed on a hydrophilic surface is ~1 nm at 40% RH [152]. However, in the simulation, the water bridge is too thin to construct a proper mesh when H is smaller than 0.1 μm. In Fig. 4.8(c) we plot the simulation result of Q as a function of H, which can be fitted well by an exponential recovery curve $Q = a_1(1 - \exp(-H/a_2)) + a_3$ with fitting parameters a_1, a_2, and a_3. This curve is attenuated to $\sim 3.08 \times 10^3$ e when H is smaller than 0.1 μm, which is of the same order of magnitude as the experimental value of field-induced charge transfer ($\sim 1 \times 10^3$ e) for the same DC electric field applied ($E = 8 \times 10^5$ V/m). The smaller experimental value may result from the incomplete coverage of water islands in

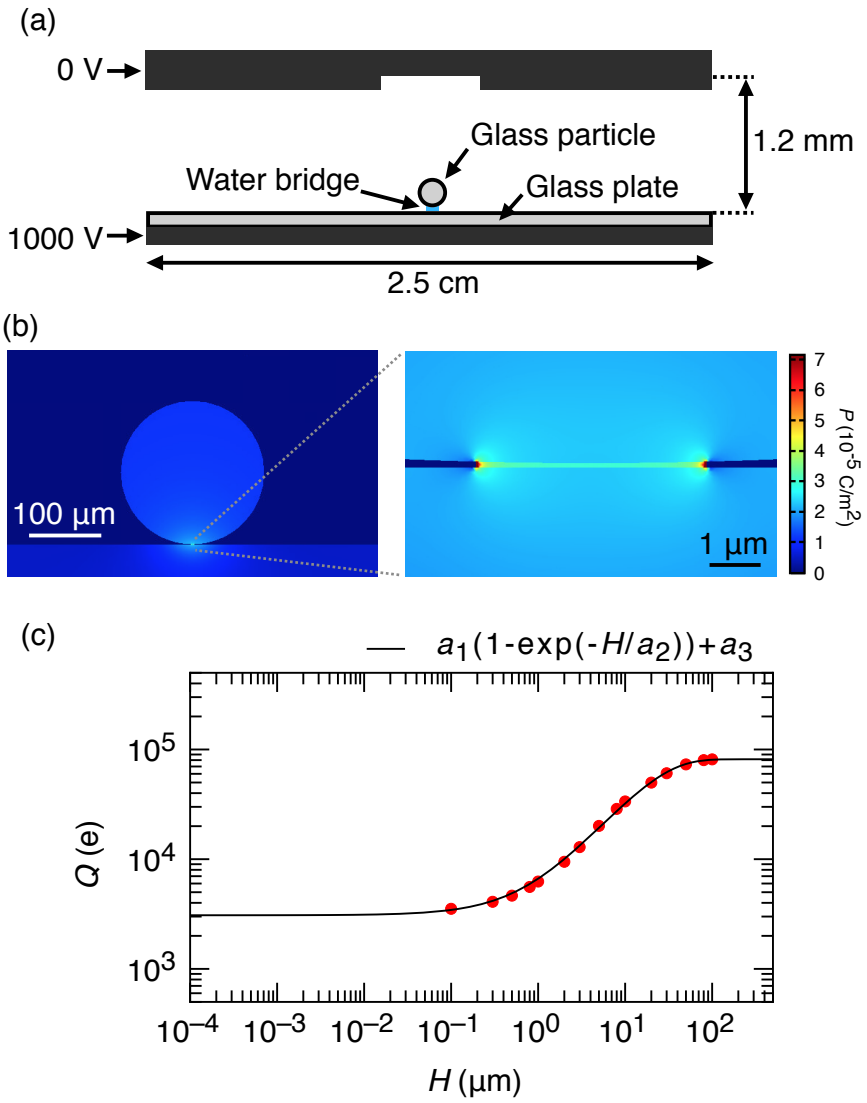

Figure 4.8: Finite-element simulation for the polarization of a water bridge between a glass particle and a glass plate. (a) Schematics of the simulation. (b) Simulation of polarization P surrounding a glass particle, a water bridge, and a glass plate. The simulation with a 0.1-μm thick water bridge is shown here. (d) Simulations of the surface bound charge of the polarized water at the solid-water interface (Q) as a function of the thickness of the water bridge (H).

the contact area. The polarization of water can thus account for the field-induced particle charging between hydrophilic surfaces.

By contrast, for a hydrophobic glass particle colliding with a hydrophobic glass target plate in a DC electric field, the slope of the linear fit of $(dq/dN)_E - (dq/dN)_0$ vs. E is measured as $2.8 \times 10^{-5} \pm 3 \times 10^{-6}$ (e/collision)/(V/m) (Fig. 4.7(g)), much smaller than that for the case of hydrophilic glasses. This result is in agreement with the scenario involving polarization of water bridges: smaller amount of adsorbed water on the hydrophobic surfaces gives rise to lower transfer of ions induced by electric fields [165]. It also highlights the importance of the surface properties as opposed to the properties of the bulk materials in the field-induced particle charging.

4.4 Proposed mechanism for size-dependent particle charging

The picture of individual water islands adsorbed on solid surfaces may also account for the tribocharging in same-material grains considered in Chapter 2 and 3. When two particles collide, nanoscale dry or wet areas on both surfaces are brought into contact, and OH^- ions can be transferred from a wet area on one surface to a dry area on another surface. If different sizes of particles are involved, charge can be built up due to an asymmetry of contact areas.

We conducted a Monte Carlo simulation for the charge transfer within a mixture of large and small particles in equal number. We set the ratio of the sizes for large and small particles to be 3:2. By taking water islands into consideration, we partition the surfaces of the large and small particles into smaller patches with the same size. Each patch is assigned as either a "dry" patch or a "wet" one. The probability for a patch to be wet is set to be 30% on both large and small particles. In each routine, two patches on different particles are randomly picked, regardless of the particle size, and brought into contact. When two patches collide, if the transferable charges are not depleted, a fixed amount of negative charge (OH^- ions) is transferred from a wet patch to a dry one. No charge transfer happens for other cases.

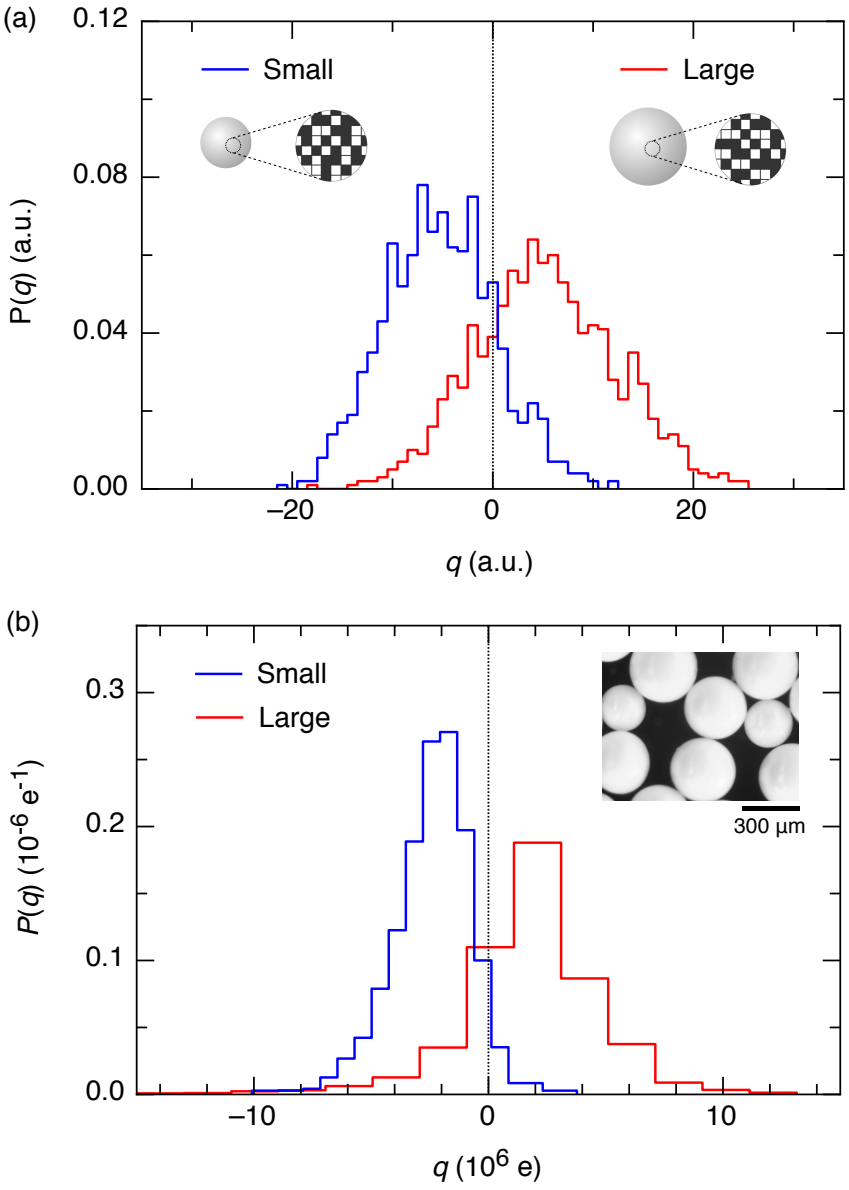

Figure 4.9: Monte Carlo simulation of tribocharging in same-material grains due to OH^- transfer compared with experimental data. (a) Particle charge distribution result of a Monte Carlo simulation, where large and small particles are mixed together in equal number and transfer charge for many particle collisions. (b) Experimental result of particle charge distribution due to mixing large and small grains in equal number, which is the same as the data presented in Fig. 3.6.

Initially, all wet patches have the same amount of OH^- ions, and those ions can be depleted after many collisions. The net charge q is the sum of the patch charges on each particle.

Figure 4.9(a) shows the final state of the particle charge distribution when all the available charges are depleted. It shows that larger particles tend to be positive, and smaller ones tend to be negative. This result is due to the asymmetric transfer of OH^- ions for large and small particles. If the surface density of wet patches is the same on all particles, larger particles will have more total area of wet patches due to the larger surface area, so at first, they will have more OH^- ions to transfer than smaller ones. Therefore, after all of the available OH^- ions are depleted, larger particles will tend to be more positive. Smaller particles will give out less and collect more OH^- ions than larger particles, getting more negative after many collisions.

The result in Fig. 4.9(a) resembles the charge distribution in charging experiments with bidisperse particle sizes in Chapter 2 and 3 (Fig. 4.9(b) and Fig. 3.6). Here, we show that the nanoscale dry/wet patches and the transfer of OH^- ions may explain the charging in particles made of the same material.

4.5 Summary

We have developed a new particle charge measurement technique based on acoustic levitation, which allows us to repeatedly measure the charge on a single sub-millimeter particle and the charge transfer due to collisions with a target plate. We show that contact charging of glass particles can be greatly affected just by changing the hydrophobicity of either glass surface: hydrophilic surfaces accumulate positive charges, whereas hydrophobic surfaces obtain negative charges, which can be explained by the transfer of OH^- ions between nonionic insulators. The results that contact charging between a hydrophilic and a hydrophobic surface is suppressed (enhanced) in an acidic (basic) atmosphere further support this mechanism. Moreover, we are able to control the charge transfer by applying an external electric field during particle collisions. This charge transfer can be attributed to the separation of

aqueous ions in water bridges between surfaces due to the electric field. We show that the field-induced particle charging is much larger for hydrophilic insulators than for hydrophobic ones, emphasizing the role of adsorbed water in contact charging of nonionic insulators. We propose that water islands and aqueous ions can also account for the effect of charge segregation in particles with bidisperse particle sizes.

Chapter 5

Conclusions

This thesis focuses on the understanding of the electrostatic charging effects in microscopic insulating grains. Tracking microscopic grains accelerated in a horizontal electric field, we were able to measure the charges of individual grains directly (Chapter 2). We showed that same-material tribocharging depends on particle size, with large grains becoming more positively charged and small ones more negatively charged. Previous models assuming the transfer of trapped electrons so far have not been validated. We demonstrated that the density of trapped electrons, measured independently by a thermoluminescence technique, is orders of magnitude too low to account for the amount of charge transferred. This result showed that trapped electrons are not causing same-material tribocharging (at least in the dielectric grain types studied here). It suggests that another negatively charged species, such as ions, is responsible for the charge transfer.

Same-material tribocharging can result in important electrostatic interactions among microscopic particles, but how these interactions contribute to particle aggregation has remained elusive. Using free-fall, high-speed imaging, we directly observed how charged grains can orbit around each other in attractive as well as repulsive Kepler-like trajectories (Chapter 3). We demonstrated that charged particles can get trapped in their mutual electrostatic potentials and form clusters via multiple bounces. These electrostatic potentials dominate the binding energy of a cluster by several orders of magnitude and thus make clustering much easier than without electrostatic forces. Moreover, by using a bipolar particle charge distribution, we observed that particles form electrostatically stable "granular molecules". Their rearrangements are analogous to breakage and formation of bonds in chemical molecules. Furthermore, we found configurations that are stable only with full consideration of higher-order, many-body polarization effects. These polarization effects provide additional attractive forces and therefore promote aggregation.

Studying the contact charging of microscopic grains is challenging because it usually

involves a great number of complex particle collisions. We developed a new method based on acoustic levitation techniques, which allows us to repeatedly measure the charge transfer of a single sub-millimeter particle colliding with a flat plate (Chapter 4). With this method, we demonstrated that the contact charging is dependent on the hydrophobicity of particles as well as the acidity or basicity of ambient gases. Moreover, we were able to control the charge on a single particle by applying an external electric field during collisions. We found that this electric field-induced particle charging is also hydrophobicity-dependent. These results strongly support the idea of aqueous-ion transfer between dielectric surfaces.

For future work, direct measurements of charge transfer during particle-particle collisions might be possible by changing the shape of the potential wells in acoustic levitation, which will help understand the roles played in particle contact charging by the contact area, the kinetic energy, the surface geometries, and the materials of the grains play in particle contact charging. It remains important to study whether ion transfer is dominating the charge transfer between insulators in general, or whether the charging mechanisms are different for oxides and polymers. To better understand the contribution of aqueous ions in charge transfer, it will be interesting to systematically study the relationship between contact charging and zeta-potential of surfaces, which can be characterized by electrokinetic measurements or streaming current techniques.

Appendix A

Air drag in the falling-camera apparatus

At low gas pressure, the drag force F_{d} on a particle with diameter d moving at speed v can be described by

$$F_{\mathrm{d}} = F_{\mathrm{s}}(1 + K(a + be^{-c/K}))^{-1}, \tag{A.1}$$

where $F_{\mathrm{s}} = 3\pi\eta dv$ is the Stokes drag force, $\eta = 1.8 \times 10^{-5}$ Pa·s is the viscosity of air at ambient pressure 100 kPa, $a = 0.864$, $b = 0.290$, $c = 1.25$ are empirical constants [168], and $K = 2\lambda/d$ is the Knudsen number, which is the ratio of the mean free path of the gas molecules λ to the particle radius $d/2$. For our falling-camera experiments in Chapter 2 and 3, we have $d \approx 300\mu$m and at a pressure of ≈ 2 mTorr inside the vacuum chamber the mean free path is $\lambda \approx 2.6$ cm. This gives $K \approx 173 \gg 1$, which already indicates that air drag is negligible. The maximum vertical speed of the free-falling particles is $v_{\mathrm{max}} = \sqrt{2gH} \approx 5.5$ m/s, leading to a *maximum* $F_{\mathrm{d}} \approx 1$ nN, much smaller than the electrostatic force on the order of 20-50 nN and the particle weight $mg \approx 40$ nN. Thus, air drag can be neglected in our experiments.

Appendix B

Time sequences of charged grains in free fall

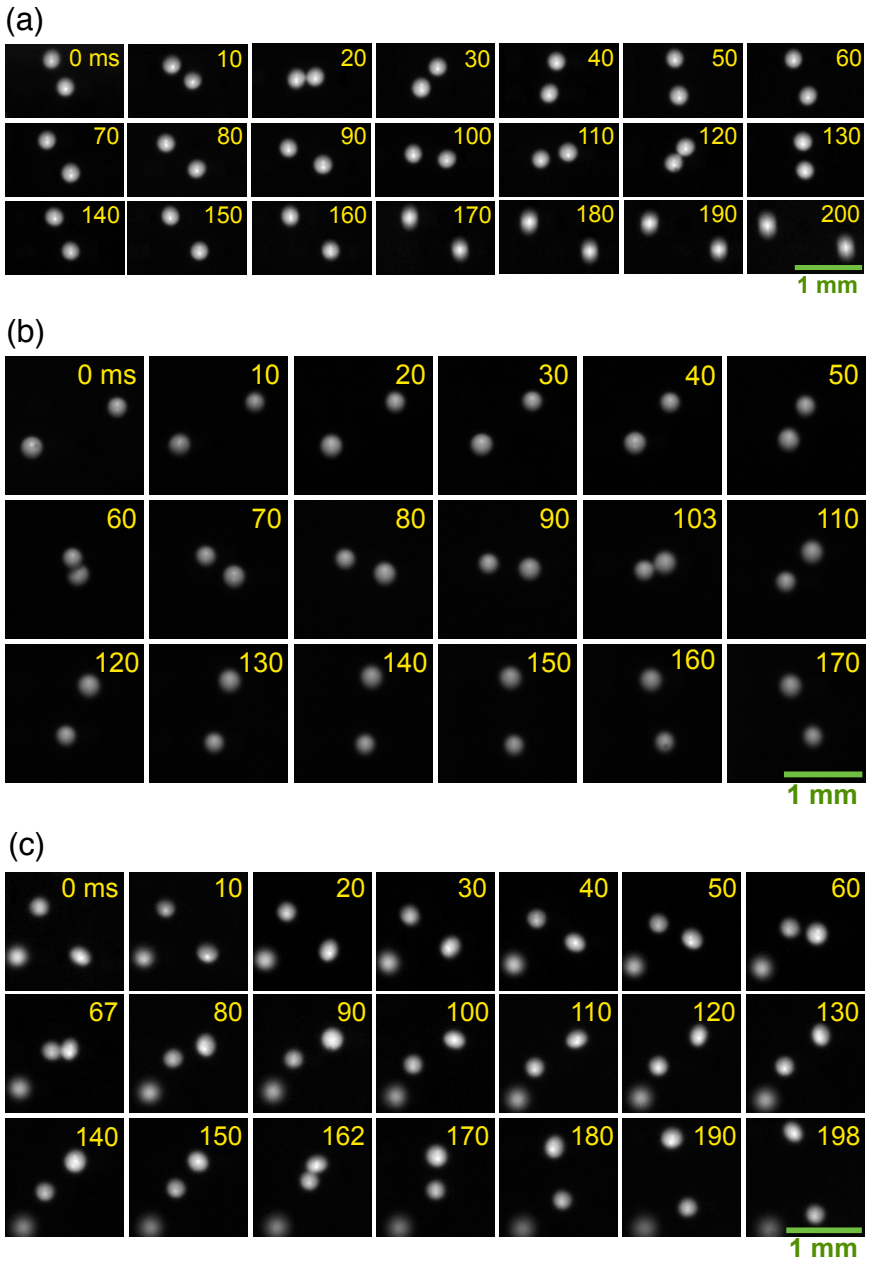

Figure B.1: (a)-(c) Sequence of stills for the particle trajectories in Fig. 3.4 (b)-(d).

Appendix C

Measuring effective coefficient of restitution from a nearly head-on collision

Figure C.1 shows an essentially head-on collision in the falling-camera experiment that allowed us to measure the effective coefficient of restitution e_{eff} (the ratio of relative velocity magnitude before and after a collision) of ZrO_2 grains. Before the collision, the target particle (Particle 1) moves slowly relative to the other nearby particles, and the incoming particle (Particle 2) is approaching at high impact velocity ($\sim$ 1.4 m/s in the x-y plane). After the collision, Particle 1 shoots off at high velocity while Particle 2 moves slowly, similar to the behavior due to momentum transfer in a 2-particle Newton's cradle. The incoming and outgoing trajectories are approximately parallel (no more than $\sim 5^\circ$ off) in the x-y plane, and we measure e_{eff} to be about 0.94.

Out-of-plane (z-direction) motion could influence this determination of e_{eff}. The 2-mm depth of field of the lens (Nikon AF Micro-Nikkor ED 200mm f/4 D IF with f-number 32 and focused distance 0.52 m) allows us to roughly estimate the z-direction velocities v_z of the slow particles. From the sharpness of the edge of the particles, we find that the out-of-plane velocity v_z of Particle 1 before the collision and Particle 2 after the collision cannot be larger than 0.01 m/s, about 2 orders of magnitude less than the x-y components of the impacting and leaving velocities. Therefore, the z-motion is too small to affect the above value for e_{eff}.

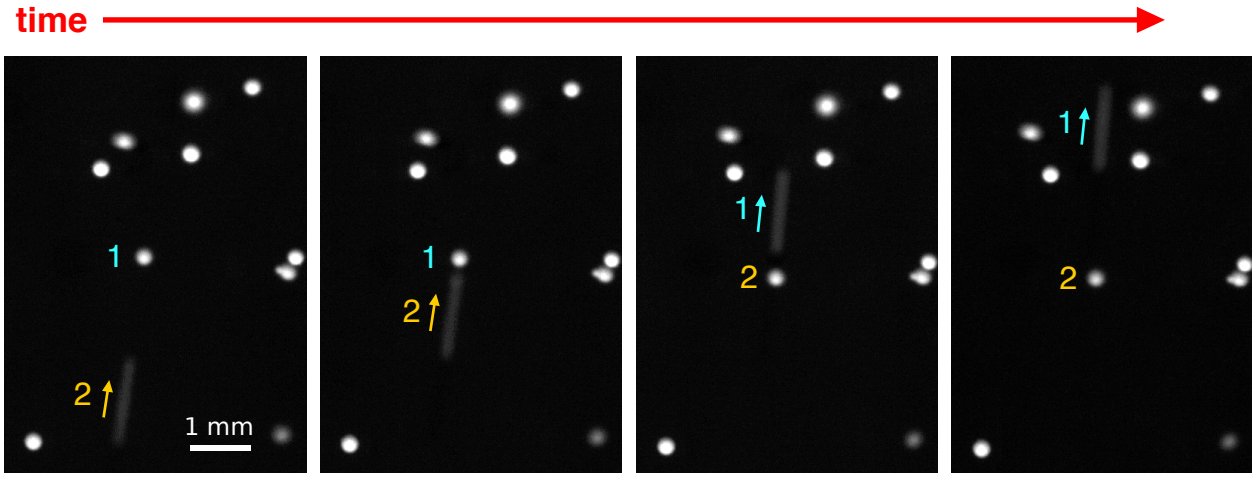

Figure C.1: Successive image stills showing a nearly head-on collision. The time interval between two frames is 1 ms. Fast (higher than 0.5 m/s) particles are elongated as lines in the stills.

Appendix D

Estimation of maximum contact area during a particle collision

The maximum contact area during a collision (A_c) due to elastic-plastic deformation for a particle being dropped onto a flat surface can be estimated with the Hertz contact theory [169, 170]:

$$A_c = 0.41\pi D^2 \sqrt{\frac{\rho_p}{Y_p}} \left(V_{imp} - 0.05\sqrt{\frac{\kappa^4 Y_p^5}{\rho_p}} \right), \tag{D.1}$$

where $D = 204 \pm 8$ μm, $\rho_p = 2200$ kg/m^3 and $Y_p = 190$ MPa are diameter, density and yield pressure of the borosilicate glass particle, respectively, supplied by the manufacturer, $V_{imp} = \sqrt{2gh} = 0.11$ m/s is the impact velocity, $h = 0.6$ mm is the drop height, $\kappa = (1-\nu_1)^2/E_1 + (1-\nu_1)^2/E_2$ is the elasticity parameter, $\nu_1 = \nu_2 = 0.2$ and $E_1 = E_2 = 67.5$ GPa are Poisson's ratio and Young's modulus of borosilicate glass [166], and subscripts 1 and 2 denote the particle and the target plate, respectively. We obtain $A_c \sim 20$ μm^2 for a glass particle in our acoustic-levitation setup in Chapter 4.

References

[1] M. Brook, C. Moore, and T. Sigurgeirsson, "Lightning in volcanic clouds," *Journal of Geophysical Research*, vol. 79, no. 3, pp. 472–475, 1974.

[2] C. Stow, "Dust and sand storm electrification," *Weather*, vol. 24, no. 4, pp. 134–144, 1969.

[3] W. Farrell, P. Smith, G. Delory, G. Hillard, J. Marshall, D. Catling, M. Hecht, D. Tratt, N. Renno, M. Desch, S. Cummer, J. Houser, and B. Johnson, "Electric and magnetic signatures of dust devils from the 2000–2001 MATADOR desert tests," *Journal of Geophysical Research: Planets*, vol. 109, no. E3, 2004.

[4] Y. Yair, "Charge generation and separation processes," *Space Science Reviews*, vol. 137, no. 1-4, pp. 119–131, 2008.

[5] D. Boland, Q. Al-Salim, and D. Geldart, "Static electrification in fluidised beds," *Chemical Engineering Science*, vol. 24, no. 8, pp. 1389–1390, 1969.

[6] M. F. Al-Adel, D. A. Saville, and S. Sundaresan, "The effect of static electrification on gas-solid flows in vertical risers," *Industrial & Engineering Chemistry Research*, vol. 41, no. 25, pp. 6224–6234, 2002.

[7] T. Abbasi and S. Abbasi, "Dust explosions–cases, causes, consequences, and control," *Journal of Hazardous Materials*, vol. 140, no. 1, pp. 7–44, 2007.

[8] L. B. Schein, *Electrophotography and Development Physics*, vol. 14. Springer Science & Business Media, 2013.

[9] A. G. Bailey, "The science and technology of electrostatic powder spraying, transport and coating," *Journal of Electrostatics*, vol. 45, no. 2, pp. 85–120, 1998.

[10] A. Jaworek, A. Krupa, and T. Czech, "Modern electrostatic devices and methods for exhaust gas cleaning: A brief review," *Journal of Electrostatics*, vol. 65, no. 3, pp. 133–155, 2007.

[11] L. S. McCarty and G. M. Whitesides, "Electrostatic charging due to separation of ions at interfaces: contact electrification of ionic electrets," *Angewandte Chemie International Edition*, vol. 47, no. 12, pp. 2188–2207, 2008.

[12] P. F. O'grady, *Thales of Miletus: The Beginnings of Western Science and Philosophy*. Routledge, 2017.

[13] A. Diaz and R. Felix-Navarro, "A semi-quantitative tribo-electric series for polymeric materials: the influence of chemical structure and properties," *Journal of Electrostatics*, vol. 62, no. 4, pp. 277–290, 2004.

[14] W. R. Harper, *Contact and Frictional Electrification*. Laplacian Press Morgan Hill, CA, 1998.

[15] J. Lowell and A. Rose-Innes, "Contact electrification," *Advances in Physics*, vol. 29, no. 6, pp. 947–1023, 1980.

[16] J. A. Wiles, B. A. Grzybowski, A. Winkleman, and G. M. Whitesides, "A tool for studying contact electrification in systems comprising metals and insulating polymers," *Analytical Chemistry*, vol. 75, no. 18, pp. 4859–4867, 2003.

[17] J. Lowell and W. Truscott, "Triboelectrification of identical insulators. I. An experimental investigation," *Journal of Physics D: Applied Physics*, vol. 19, no. 7, p. 1273, 1986.

[18] J. Lowell and W. Truscott, "Triboelectrification of identical insulators. II. Theory and further experiments," *Journal of Physics D: Applied Physics*, vol. 19, no. 7, p. 1281, 1986.

[19] C. Liu and A. J. Bard, "Electrostatic electrochemistry at insulators," *Nature Materials*, vol. 7, no. 6, pp. 505–509, 2008.

[20] C.-Y. Liu and A. J. Bard, "Chemical redox reactions induced by cryptoelectrons on a PMMA surface," *Journal of the American Chemical Society*, vol. 131, no. 18, pp. 6397–6401, 2009.

[21] S. Piperno, H. Cohen, T. Bendikov, M. Lahav, and I. Lubomirsky, "The absence of redox reactions for Palladium(II) and Copper(II) on electrostatically charged Teflon: Relevance to the concept of "Cryptoelectrons"," *Angewandte Chemie International Edition*, vol. 50, no. 25, pp. 5654–5657, 2011.

[22] B. Baytekin, H. T. Baytekin, and B. A. Grzybowski, "What really drives chemical reactions on contact charged surfaces?," *Journal of the American Chemical Society*, vol. 134, no. 17, pp. 7223–7226, 2012.

[23] J. Medley, "Fractional electrification of polar polymers," *Nature*, vol. 171, no. 4363, pp. 1077–1077, 1953.

[24] S. Pence, V. Novotny, and A. Diaz, "Effect of surface moisture on contact charge of polymers containing ions," *Langmuir*, vol. 10, no. 2, pp. 592–596, 1994.

[25] A. Diaz, "Contact electrification of materials: the chemistry of ions on polymer surfaces," *The Journal of Adhesion*, vol. 67, no. 1-4, pp. 111–122, 1998.

[26] A. Diaz, D. Wollmann, and D. Dreblow, "Contact electrification: ion transfer to metals and polymers," *Chemistry of Materials*, vol. 3, no. 6, pp. 997–999, 1991.

[27] S. W. Thomas, S. J. Vella, G. K. Kaufman, and G. M. Whitesides, "Patterns of electrostatic charge and discharge in contact electrification," *Angewandte Chemie*, vol. 120, no. 35, pp. 6756–6758, 2008.

[28] L. S. McCarty, A. Winkleman, and G. M. Whitesides, "Ionic electrets: electrostatic charging of surfaces by transferring mobile ions upon contact," *Journal of the American Chemical Society*, vol. 129, no. 13, pp. 4075–4088, 2007.

[29] S. W. Thomas Iii, S. J. Vella, M. D. Dickey, G. K. Kaufman, and G. M. Whitesides, "Controlling the kinetics of contact electrification with patterned surfaces," *Journal of the American Chemical Society*, vol. 131, no. 25, pp. 8746–8747, 2009.

[30] T. W. Healy and D. W. Fuerstenau, "The isoelectric point/point-of zero-charge of interfaces formed by aqueous solutions and nonpolar solids, liquids, and gases," *Journal of Colloid and Interface Science*, vol. 309, no. 1, pp. 183–188, 2007.

[31] K. N. Kudin and R. Car, "Why are water- hydrophobic interfaces charged?," *Journal of the American Chemical Society*, vol. 130, no. 12, pp. 3915–3919, 2008.

[32] R. Zimmermann, S. Dukhin, and C. Werner, "Electrokinetic measurements reveal interfacial charge at polymer films caused by simple electrolyte ions," *The Journal of Physical Chemistry B*, vol. 105, no. 36, pp. 8544–8549, 2001.

[33] J. A. Wiles, M. Fialkowski, M. R. Radowski, G. M. Whitesides, and B. A. Grzybowski, "Effects of surface modification and moisture on the rates of charge transfer between metals and organic materials," *The Journal of Physical Chemistry B*, vol. 108, no. 52, pp. 20296–20302, 2004.

[34] R. F. Gouveia and F. Galembeck, "Electrostatic charging of hydrophilic particles due to water adsorption," *Journal of the American Chemical Society*, vol. 131, no. 32, pp. 11381–11386, 2009.

[35] R. F. Gouveia, J. S. Bernardes, T. R. Ducati, and F. Galembeck, "Acid–base site detection and mapping on solid surfaces by Kelvin force microscopy (KFM)," *Analytical Chemistry*, vol. 84, no. 23, pp. 10191–10198, 2012.

[36] M. Hogue, C. Buhler, C. Calle, T. Matsuyama, W. Luo, and E. Groop, "Insulator–insulator contact charging and its relationship to atmospheric pressure," *Journal of Electrostatics*, vol. 61, no. 3, pp. 259–268, 2004.

[37] W. Salaneck, A. Paton, and D. Clark, "Double mass transfer during polymer-polymer contacts," *Journal of Applied Physics*, vol. 47, no. 1, pp. 144–147, 1976.

[38] J. Lowell, "The role of material transfer in contact electrification," *Journal of Physics D: Applied Physics*, vol. 10, no. 17, p. L233, 1977.

[39] H. Baytekin, A. Patashinski, M. Branicki, B. Baytekin, S. Soh, and B. A. Grzybowski, "The mosaic of surface charge in contact electrification," *Science*, vol. 333, no. 6040, pp. 308–312, 2011.

[40] D. J. Lacks and R. M. Sankaran, "Contact electrification of insulating materials," *Journal of Physics D: Applied Physics*, vol. 44, no. 45, p. 453001, 2011.

[41] T. Matsuyama and H. Yamamoto, "Charge-relaxation process dominates contact charging of a particle in atmospheric condition: II. The general model," *Journal of Physics D: Applied Physics*, vol. 30, no. 15, p. 2170, 1997.

[42] C. Wadhwa, *High Voltage Engineering*. New Age International, pp. 10–12, 2007.

[43] D. J. Lacks, "The unpredictability of electrostatic charging," *Angewandte Chemie International Edition*, vol. 51, no. 28, pp. 6822–6823, 2012.

[44] M. Sow, D. J. Lacks, and R. Mohan Sankaran, "Dependence of contact electrification on the magnitude of strain in polymeric materials," *Journal of Applied Physics*, vol. 112, no. 8, p. 084909, 2012.

[45] M. Sow, R. Widenor, A. Kumar, S. W. Lee, D. J. Lacks, and R. M. Sankaran, "Strain-induced reversal of charge transfer in contact electrification," *Angewandte Chemie International Edition*, vol. 51, no. 11, pp. 2695–2697, 2012.

[46] H. T. Baytekin, B. Baytekin, J. T. Incorvati, and B. A. Grzybowski, "Material transfer and polarity reversal in contact charging," *Angewandte Chemie*, vol. 124, no. 20, pp. 4927–4931, 2012.

[47] R. Pham, R. C. Virnelson, R. M. Sankaran, and D. J. Lacks, "Contact charging between surfaces of identical insulating materials in asymmetric geometries," *Journal of Electrostatics*, vol. 69, no. 5, pp. 456–460, 2011.

[48] T. Shinbrot, T. Komatsu, and Q. Zhao, "Spontaneous tribocharging of similar materials," *EPL (Europhysics Letters)*, vol. 83, no. 2, p. 24004, 2008.

[49] M. M. Apodaca, P. J. Wesson, K. J. Bishop, M. A. Ratner, and B. A. Grzybowski, "Contact electrification between identical materials," *Angewandte Chemie*, vol. 122, no. 5, pp. 958–961, 2010.

[50] G. D. Freier, "The electric field of a large dust devil," *Journal of Geophysical Research*, vol. 65, no. 10, pp. 3504–3504, 1960.

[51] T. Miura, T. Koyaguchi, and Y. Tanaka, "Measurements of electric charge distribution in volcanic plumes at Sakurajima Volcano, Japan," *Bulletin of Volcanology*, vol. 64, no. 2, pp. 75–93, 2002.

[52] P. Cartwright, S. Singh, A. G. Bailey, and L. Rose, "Electrostatic charging characteristics of polyethylene powder during pneumatic conveying," *IEEE Transactions on Industry Applications*, no. 2, pp. 541–546, 1985.

[53] I. I. Inculet, G. P. Castle, and G. Aartsen, "Generation of bipolar electric fields during industrial handling of powders," *Chemical Engineering Science*, vol. 61, no. 7, pp. 2249–2253, 2006.

[54] D. J. Lacks and A. Levandovsky, "Effect of particle size distribution on the polarity of triboelectric charging in granular insulator systems," *Journal of Electrostatics*, vol. 65, no. 2, pp. 107–112, 2007.

[55] D. J. Lacks, N. Duff, and S. K. Kumar, "Nonequilibrium accumulation of surface species and triboelectric charging in single component particulate systems," *Physical Review Letters*, vol. 100, no. 18, p. 188305, 2008.

[56] T. Pähtz, H. J. Herrmann, and T. Shinbrot, "Why do particle clouds generate electric charges?," *Nature Physics*, vol. 6, no. 5, pp. 364–368, 2010.

[57] R. Yoshimatsu, N. Araújo, G. Wurm, H. Herrmann, and T. Shinbrot, "Self-charging of identical grains in the absence of an external field," *Scientific Reports*, vol. 7, 2017.

[58] A. Mehrotra, F. J. Muzzio, and T. Shinbrot, "Spontaneous separation of charged grains," *Physical Review Letters*, vol. 99, no. 5, p. 058001, 2007.

[59] R. Cocco, F. Shaffer, R. Hays, S. R. Karri, and T. Knowlton, "Particle clusters in and above fluidized beds," *Powder Technology*, vol. 203, no. 1, pp. 3–11, 2010.

[60] S. Chen, W. Liu, and S. Li, "Effect of long-range electrostatic repulsion on pore clogging during microfiltration," *Physical Review E*, vol. 94, no. 6, p. 063108, 2016.

[61] B. A. Grzybowski, A. Winkleman, J. A. Wiles, Y. Brumer, and G. M. Whitesides, "Electrostatic self-assembly of macroscopic crystals using contact electrification," *Nature Materials*, vol. 2, no. 4, pp. 241–245, 2003.

[62] R. Cademartiri, C. A. Stan, V. M. Tran, E. Wu, L. Friar, D. Vulis, L. W. Clark, S. Tricard, and G. M. Whitesides, "A simple two-dimensional model system to study electrostatic-self-assembly," *Soft Matter*, vol. 8, no. 38, pp. 9771–9791, 2012.

[63] J. Blum and G. Wurm, "The growth mechanisms of macroscopic bodies in protoplanetary disks," *Annu. Rev. Astron. Astrophys.*, vol. 46, pp. 21–56, 2008.

[64] J. M. Harper, G. McDonald, J. Dufek, M. Malaska, D. Burr, A. Hayes, J. McAdams, and J. Wray, "Electrification of sand on Titan and its influence on sediment transport," *Nature Geoscience*, vol. 10, no. 4, pp. 260–265, 2017.

[65] E. Gill, "Frictional electrification of sand," *Nature*, vol. 162, pp. 568–569, 1948.

[66] T. Shinbrot and H. J. Herrmann, "Granular matter: Static in motion," *Nature*, vol. 451, no. 7180, pp. 773–774, 2008.

[67] J. R. Leeman and E. D. Schmitter, "Electric signals generated by tornados," *Atmospheric Research*, vol. 92, no. 2, pp. 277–279, 2009.

[68] R. Anderson, S. Gathman, J. Hughes, S. Björnsson, S. Jónasson, D. C. Blanchard, C. B. Moore, H. J. Survilas, and B. Vonnegut, "Electricity in volcanic clouds," *Science*, vol. 148, no. 3674, pp. 1179–1189, 1965.

[69] T. Mather and R. Harrison, "Electrification of volcanic plumes," *Surveys in Geophysics*, vol. 27, no. 4, pp. 387–432, 2006.

[70] I. M. Houghton, K. L. Aplin, and K. A. Nicoll, "Triboelectric charging of volcanic ash from the 2011 Grímsvötn eruption," *Physical Review Letters*, vol. 111, no. 11, p. 118501, 2013.

[71] C. Cimarelli, M. Alatorre-Ibargüengoitia, U. Kueppers, B. Scheu, and D. B. Dingwell, "Experimental generation of volcanic lightning," *Geology*, vol. 42, no. 1, pp. 79–82, 2014.

[72] H. Zhao, G. Castle, and I. Inculet, "The measurement of bipolar charge in polydisperse powders using a vertical array of Faraday pail sensors," *Journal of Electrostatics*, vol. 55, no. 3, pp. 261–278, 2002.

[73] K. M. Forward, D. J. Lacks, and R. M. Sankaran, "Methodology for studying particle–particle triboelectrification in granular materials," *Journal of Electrostatics*, vol. 67, no. 2, pp. 178–183, 2009.

[74] K. M. Forward, D. J. Lacks, and R. M. Sankaran, "Particle-size dependent bipolar charging of Martian regolith simulant," *Geophysical Research Letters*, vol. 36, no. 13, 2009.

[75] K. M. Forward, D. J. Lacks, and R. M. Sankaran, "Triboelectric charging of granular insulator mixtures due solely to particle-particle interactions," *Industrial & Engineering Chemistry Research*, vol. 48, no. 5, pp. 2309–2314, 2008.

[76] K. M. Forward, D. J. Lacks, and R. M. Sankaran, "Charge segregation depends on particle size in triboelectrically charged granular materials," *Physical Review Letters*, vol. 102, no. 2, p. 028001, 2009.

[77] N. Duff and D. J. Lacks, "Particle dynamics simulations of triboelectric charging in granular insulator systems," *Journal of Electrostatics*, vol. 66, no. 1, pp. 51–57, 2008.

[78] W. Hu, L. Xie, and X. Zheng, "Contact charging of silica glass particles in a single collision," *Applied Physics Letters*, vol. 101, no. 11, p. 114107, 2012.

[79] J. C. Crocker and D. G. Grier, "Methods of digital video microscopy for colloidal studies," *Journal of Colloid and Interface Science*, vol. 179, no. 1, pp. 298–310, 1996.

[80] S. Waitukaitis and H. Jaeger, "In situ granular charge measurement by free-fall videography," *Review of Scientific Instruments*, vol. 84, no. 2, p. 025104, 2013.

[81] P. Iacconi, D. Lapraz, and R. Caruba, "Traps and emission centres in thermoluminescent ZrO_2," *Physica Status Solidi (a)*, vol. 50, no. 1, pp. 275–283, 1978.

[82] W.-C. Hsieh and C.-S. Su, "UV induced thermoluminescence in ZrO_2 doped by Er_2O_3," *Journal of Physics D: Applied Physics*, vol. 27, no. 8, p. 1763, 1994.

[83] H. Hristov, N. Arhangelova, V. Velev, I. Penev, M. Bello, G. Moschini, and N. Uzunov, "UV light-induced thermoluminescence of Er+ Li doped ZrO_2," in *Journal of Physics: Conference Series*, vol. 253, p. 012025, IOP Publishing, 2010.

[84] J. Azorin, T. Rivera, C. Falcony, E. Martinez, and M. García, "Ultraviolet thermoluminescent dosimetry using terbium-doped zirconium oxide thin films," *Radiation Protection Dosimetry*, vol. 85, no. 1-4, pp. 317–320, 1999.

[85] J. Randall and M. H. F. Wilkins, "Phosphorescence and electron traps. I. The study of trap distributions," in *Proceedings of the Royal Society of London A: Mathematical, Physical and Engineering Sciences*, vol. 184, pp. 365–389, The Royal Society, 1945.

[86] M. J. Aitken, *Thermoluminescence Dating*. Academic press, 1985.

[87] J. S. Noller, J. M. Sowers, and W. R. Lettis, *Quaternary Geochronology: Methods and Applications*, vol. 4. American Geophysical Union, pp. 157–176, 2000.

[88] A. Kamra, "Measurements of the electrical properties of dust storms," *Journal of Geophysical Research*, vol. 77, no. 30, pp. 5856–5869, 1972.

[89] J. F. Kok and N. O. Renno, "Electrostatics in wind-blown sand," *Physical Review Letters*, vol. 100, no. 1, p. 014501, 2008.

[90] D. Schmidt, R. Schmidt, and J. Dent, "Electrostatic force on saltating sand," *Journal of Geophysical Research: Atmospheres*, vol. 103, no. D8, pp. 8997–9001, 1998.

[91] W. Harper, "The volta effect as a cause of static electrification," in *Proceedings of the Royal Society of London A: Mathematical, Physical and Engineering Sciences*, vol. 205, pp. 83–103, The Royal Society, 1951.

[92] J. Lowell, "Contact electrification of metals," *Journal of Physics D: Applied Physics*, vol. 8, no. 1, p. 53, 1975.

[93] C.-Y. Liu and A. J. Bard, "Electrostatic electrochemistry: Nylon and polyethylene systems," *Chemical Physics Letters*, vol. 485, no. 1, pp. 231–234, 2010.

[94] C.-Y. Liu and A. J. Bard, "Electrons on dielectrics and contact electrification," *Chemical Physics Letters*, vol. 480, no. 4, pp. 145–156, 2009.

[95] A. Zsom, C. Ormel, C. Güttler, J. Blum, and C. Dullemond, "The outcome of protoplanetary dust growth: pebbles, boulders, or planetesimals?-II. Introducing the bouncing barrier," *Astronomy & Astrophysics*, vol. 513, p. A57, 2010.

[96] A. Kataoka, H. Tanaka, S. Okuzumi, and K. Wada, "Fluffy dust forms icy planetesimals by static compression," *Astronomy & Astrophysics*, vol. 557, p. L4, 2013.

[97] A. Castellanos, "The relationship between attractive interparticle forces and bulk behaviour in dry and uncharged fine powders," *Advances in Physics*, vol. 54, no. 4, pp. 263–376, 2005.

[98] J. Marshall, "Discrete-element modeling of particulate aerosol flows," *Journal of Computational Physics*, vol. 228, no. 5, pp. 1541–1561, 2009.

[99] N. V. Brilliantov and T. Pöschel, *Kinetic Theory of Granular Gases*. Oxford University Press, 2010.

[100] F. Spahn, N. Albers, M. Sremčević, and C. Thornton, "Kinetic description of coagulation and fragmentation in dilute granular particle ensembles," *EPL (Europhysics Letters)*, vol. 67, no. 4, p. 545, 2004.

[101] N. V. Brilliantov, N. Albers, F. Spahn, and T. Pöschel, "Collision dynamics of granular particles with adhesion," *Physical Review E*, vol. 76, no. 5, p. 051302, 2007.

[102] L. Schein, "Recent progress and continuing puzzles in electrostatics," *Science*, vol. 316, no. 5831, pp. 1572–1573, 2007.

[103] T. Poppe, J. Blum, and T. Henning, "Experiments on collisional grain charging of micron-sized preplanetary dust," *The Astrophysical Journal*, vol. 533, no. 1, p. 472, 2000.

[104] M. E. Leunissen, C. G. Christova, A.-P. Hynninen, C. P. Royall, A. I. Campbell, A. Imhof, M. Dijkstra, R. Van Roij, and A. Van Blaaderen, "Ionic colloidal crystals of oppositely charged particles," *Nature*, vol. 437, no. 7056, pp. 235–240, 2005.

[105] A. Ivlev, G. Morfill, and U. Konopka, "Coagulation of charged microparticles in neutral gas and charge-induced gel transitions," *Physical Review Letters*, vol. 89, no. 19, p. 195502, 2002.

[106] K. Barros and E. Luijten, "Dielectric effects in the self-assembly of binary colloidal aggregates," *Physical Review Letters*, vol. 113, no. 1, p. 017801, 2014.

[107] K. F. Freed, "Perturbative many-body expansion for electrostatic energy and field for system of polarizable charged spherical ions in a dielectric medium," *Journal of Chemical Physics*, vol. 141, no. 3, p. 034115, 2014.

[108] R. Weidling, C. Güttler, and J. Blum, "Free collisions in a microgravity many-particle experiment. I. Dust aggregate sticking at low velocities," *Icarus*, vol. 218, no. 1, pp. 688–700, 2012.

[109] R. Yousefi, A. B. Davis, J. Carmona-Reyes, L. S. Matthews, and T. W. Hyde, "Measurement of net electric charge and dipole moment of dust aggregates in a complex plasma," *Physical Review E*, vol. 90, no. 3, p. 033101, 2014.

[110] J. R. Royer, D. J. Evans, L. Oyarte, Q. Guo, E. Kapit, M. E. Möbius, S. R. Waitukaitis, and H. M. Jaeger, "High-speed tracking of rupture and clustering in freely falling granular streams," *Nature*, vol. 459, no. 7250, pp. 1110–1113, 2009.

[111] S. R. Waitukaitis, V. Lee, J. M. Pierson, S. L. Forman, and H. M. Jaeger, "Size-dependent same-material tribocharging in insulating grains," *Physical Review Letters*, vol. 112, no. 21, p. 218001, 2014.

[112] Y. Nakajima and T. Sato, "Calculation of electrostatic force between two charged dielectric spheres by the re-expansion method," *Journal of Electrostatics*, vol. 45, no. 3, pp. 213–226, 1999.

[113] R. W. Hockney and J. W. Eastwood, *Computer Simulation Using Particles*. CRC Press, 1988.

[114] J. C. Lagarias, J. A. Reeds, M. H. Wright, and P. E. Wright, "Convergence properties of the Nelder–Mead simplex method in low dimensions," *SIAM Journal on Optimization*, vol. 9, no. 1, pp. 112–147, 1998.

[115] S. F. Foerster, M. Y. Louge, H. Chang, and K. Allia, "Measurements of the collision properties of small spheres," *Physics of Fluids*, vol. 6, no. 3, pp. 1108–1115, 1994.

[116] E. Bichoutskaia, A. L. Boatwright, A. Khachatourian, and A. J. Stace, "Electrostatic analysis of the interactions between charged particles of dielectric materials," *Journal of Chemical Physics*, vol. 133, no. 2, p. 024105, 2010.

[117] K. Barros, D. Sinkovits, and E. Luijten, "Efficient and accurate simulation of dynamic dielectric objects," *Journal of Chemical Physics*, vol. 140, no. 6, p. 064903, 2014.

[118] R. G. Horn, D. Smith, and A. Grabbe, "Contact electrification induced by monolayer modification of a surface and relation to acid–base interactions," *Nature*, vol. 366, no. 6454, pp. 442–443, 1993.

[119] J. Clint and T. Dunstan, "Acid-base components of solid surfaces and the triboelectric series," *EPL (Europhysics Letters)*, vol. 54, no. 3, p. 320, 2001.

[120] F. Galembeck, T. A. Burgo, L. B. Balestrin, R. F. Gouveia, C. A. Silva, and A. Galembeck, "Friction, tribochemistry and triboelectricity: recent progress and perspectives," *RSC Advances*, vol. 4, no. 109, pp. 64280–64298, 2014.

[121] S. Friedle and S. W. Thomas, "Controlling contact electrification with photochromic polymers," *Angewandte Chemie International Edition*, vol. 49, no. 43, pp. 7968–7971, 2010.

[122] R. P. Veregin, M. N. McDougall, M. S. Hawkins, C. Vong, V. Skorokhod, and H. P. Schreiber, "A bidirectional acid-base charging model for triboelectrification: part 1. Theory," *Journal of Imaging Science and Technology*, vol. 50, no. 3, pp. 282–287, 2006.

[123] R. P. Veregin, M. N. McDougall, M. S. Hawkins, C. Vong, V. Skorokhod, and H. P. Schreiber, "A bidirectional acid-base charging model for triboelectrification: part II. Experimental verification by inverse gas chromatography and charging of metal oxides," *Journal of Imaging Science and Technology*, vol. 50, no. 3, pp. 288–293, 2006.

[124] G. E. Ewing, "Ambient thin film water on insulator surfaces," *Chemical Reviews*, vol. 106, no. 4, pp. 1511–1526, 2006.

[125] A. Berman, "Water vapor in vacuum systems," *Vacuum*, vol. 47, no. 4, pp. 327–332, 1996.

[126] H. T. Baytekin, B. Baytekin, S. Soh, and B. A. Grzybowski, "Is water necessary for contact electrification?," *Angewandte Chemie International Edition*, vol. 50, no. 30, pp. 6766–6770, 2011.

[127] T. R. Ducati, L. H. Simoes, and F. Galembeck, "Charge partitioning at gas-solid interfaces: Humidity causes electricity buildup on metals," *Langmuir*, vol. 26, no. 17, pp. 13763–13766, 2010.

[128] R. Zimmermann, U. Freudenberg, R. Schweiß, D. Küttner, and C. Werner, "Hydroxide and hydronium ion adsorption—a survey," *Current Opinion in Colloid & Interface Science*, vol. 15, no. 3, pp. 196–202, 2010.

[129] Y.-H. M. Chan, R. Schweiss, C. Werner, and M. Grunze, "Electrokinetic characterization of oligo-and poly(ethylene glycol)-terminated self-assembled monolayers on gold and glass surfaces," *Langmuir*, vol. 19, no. 18, pp. 7380–7385, 2003.

[130] J. Drzymala, Z. Sadowski, L. Holysz, and E. Chibowski, "Ice/water interface: Zeta potential, point of zero charge, and hydrophobicity," *Journal of Colloid and Interface Science*, vol. 220, no. 2, pp. 229–234, 1999.

[131] S. Yamamoto, H. Bluhm, K. Andersson, G. Ketteler, H. Ogasawara, M. Salmeron, and A. Nilsson, "In situ x-ray photoelectron spectroscopy studies of water on metals and oxides at ambient conditions," *Journal of Physics: Condensed Matter*, vol. 20, no. 18, p. 184025, 2008.

[132] T. A. Burgo, F. Galembeck, and G. H. Pollack, "Where is water in the triboelectric series?," *Journal of Electrostatics*, vol. 80, pp. 30–33, 2016.

[133] K. Yatsuzuka, Y. Mizuno, and K. Asano, "Electrification phenomena of pure water droplets dripping and sliding on a polymer surface," *Journal of Electrostatics*, vol. 32, no. 2, pp. 157–171, 1994.

[134] K. Yatsuzuka, Y. Higashiyama, and K. Asano, "Electrification of polymer surface caused by sliding ultrapure water," *IEEE Transactions on Industry Applications*, vol. 32, no. 4, pp. 825–831, 1996.

[135] M. Matsui, N. Murasaki, K. Fujibayashi, P. Y. Bao, and Y. Kishimoto, "Electrification of pure water flowing down a trough set up with a resin sheet," *Journal of Electrostatics*, vol. 31, no. 1, pp. 1–10, 1993.

[136] B. Ravelo, F. Duval, S. Kane, and B. Nsom, "Demonstration of the triboelectricity effect by the flow of liquid water in the insulating pipe," *Journal of Electrostatics*, vol. 69, no. 6, pp. 473–478, 2011.

[137] K. R. LaMarche, X. Liu, S. K. Shah, T. Shinbrot, and B. J. Glasser, "Electrostatic charging during the flow of grains from a cylinder," *Powder Technology*, vol. 195, no. 2, pp. 158–165, 2009.

[138] A. Sowinski, F. Salama, and P. Mehrani, "New technique for electrostatic charge measurement in gas–solid fluidized beds," *Journal of Electrostatics*, vol. 67, no. 4, pp. 568–573, 2009.

[139] T. Matsuyama, M. Ogu, H. Yamamoto, J. C. Marijnissen, and B. Scarlett, "Impact charging experiments with single particles of hundred micrometre size," *Powder Technology*, vol. 135, pp. 14–22, 2003.

[140] H. Watanabe, A. Samimi, Y. L. Ding, M. Ghadiri, T. Matsuyama, and K. G. Pitt, "Measurement of charge transfer due to single particle impact," *Particle & Particle Systems Characterization*, vol. 23, no. 2, pp. 133–137, 2006.

[141] A. Sickafoose, J. Colwell, M. Horányi, and S. Robertson, "Photoelectric charging of dust particles in vacuum," *Physical Review Letters*, vol. 84, no. 26, p. 6034, 2000.

[142] M. K. Mazumder, R. Ware, T. Yokoyama, B. Rubin, and D. Kamp, "Measurement of particle size and electrostatic charge distributions on toners using E-SPART analyzer," *IEEE Transactions on Industry Applications*, vol. 27, no. 4, pp. 611–619, 1991.

[143] W. L. Nyborg, "Radiation pressure on a small rigid sphere," *The Journal of the Acoustical Society of America*, vol. 42, no. 5, pp. 947–952, 1967.

[144] E. Trinh, "Compact acoustic levitation device for studies in fluid dynamics and material science in the laboratory and microgravity," *Review of Scientific Instruments*, vol. 56, no. 11, pp. 2059–2065, 1985.

[145] R. Löfstedt and S. Putterman, "Theory of long wavelength acoustic radiation pressure," *The Journal of the Acoustical Society of America*, vol. 90, no. 4, pp. 2027–2033, 1991.

[146] W. Xie and B. Wei, "Parametric study of single-axis acoustic levitation," *Applied Physics Letters*, vol. 79, no. 6, pp. 881–883, 2001.

[147] E. Lierke and L. Holitzner, "Perspectives of an acoustic–electrostatic/electrodynamic hybrid levitator for small fluid and solid samples," *Measurement Science and Technology*, vol. 19, no. 11, p. 115803, 2008.

[148] L. Gor'kov, "On the forces acting on a small particle in an acoustical field in an ideal fluid," in *Soviet Physics Doklady*, vol. 6, p. 773, 1962.

[149] M. Barmatz and P. Collas, "Acoustic radiation potential on a sphere in plane, cylindrical, and spherical standing wave fields," *The Journal of the Acoustical Society of America*, vol. 77, no. 3, pp. 928–945, 1985.

[150] S. L. Hahn, *Hilbert Transforms in Signal Processing*. Artech House Boston, p. 305, 1996.

[151] K. Xu, P. Cao, and J. R. Heath, "Graphene visualizes the first water adlayers on mica at ambient conditions," *Science*, vol. 329, no. 5996, pp. 1188–1191, 2010.

[152] D. B. Asay and S. H. Kim, "Evolution of the adsorbed water layer structure on silicon oxide at room temperature," *The Journal of Physical Chemistry B*, vol. 109, no. 35, pp. 16760–16763, 2005.

[153] Y. Awakuni and J. Calderwood, "Water vapour adsorption and surface conductivity in solids," *Journal of Physics D: Applied Physics*, vol. 5, no. 5, p. 1038, 1972.

[154] A. Bismarck, A. Boccaccini, E. Egia-Ajuriagojeaskoa, D. Hülsenberg, and T. Leutbecher, "Surface characterization of glass fibers made from silicate waste: Zeta-potential and contact angle measurements," *Journal of Materials Science*, vol. 39, no. 2, pp. 401–412, 2004.

[155] N. Kuehn, H.-J. Jacobasch, and K. Lunkenheimer, "Zum Zusammenhang zwischen dem Kontaktwinkel zwischen Wasser und festen Polymeren und ihrem zeta-potential gegenüber wäßrigen Lösungen," *Acta Polymerica*, vol. 37, no. 6, pp. 394–396, 1986.

[156] J. Rudnick and M. Barmatz, "Oscillational instabilities in single-mode acoustic levitators," *The Journal of the Acoustical Society of America*, vol. 87, no. 1, pp. 81–92, 1990.

[157] J. K. Beattie, A. M. Djerdjev, G. V. Franks, and G. G. Warr, "Dipolar anions are not preferentially attracted to the oil/water interface," *The Journal of Physical Chemistry B*, vol. 109, no. 33, pp. 15675–15676, 2005.

[158] P. Mela, A. van Den Berg, Y. Fintschenko, E. B. Cummings, B. A. Simmons, and B. J. Kirby, "The zeta potential of cyclo-olefin polymer microchannels and its effects on insulative (electrodeless) dielectrophoresis particle trapping devices," *Electrophoresis*, vol. 26, no. 9, pp. 1792–1799, 2005.

[159] D. Li, M. B. Müller, S. Gilje, R. B. Kaner, and G. G. Wallace, "Processable aqueous dispersions of graphene nanosheets," *Nature Nanotechnology*, vol. 3, no. 2, pp. 101–105, 2008.

[160] A. Schella, S. Herminghaus, and M. Schröter, "Influence of humidity on tribo-electric charging and segregation in shaken granular media," *Soft Matter*, vol. 13, no. 2, pp. 394–401, 2017.

[161] E. Németh, V. Albrecht, G. Schubert, and F. Simon, "Polymer tribo-electric charging: dependence on thermodynamic surface properties and relative humidity," *Journal of Electrostatics*, vol. 58, no. 1, pp. 3–16, 2003.

[162] B. C. Bunker, G. W. Arnold, D. E. Day, and P. Bray, "The effect of molecular structure on borosilicate glass leaching," *Journal of Non-Crystalline Solids*, vol. 87, no. 1-2, pp. 226–253, 1986.

[163] A. Ledieu, F. Devreux, P. Barboux, L. Sicard, and O. Spalla, "Leaching of borosilicate glasses. I. Experiments," *Journal of Non-Crystalline Solids*, vol. 343, no. 1, pp. 3–12, 2004.

[164] H. Scholze, *Glass: nature, structure, and properties.* Springer-Verlag New York, p. 336, 1991.

[165] Y. Zhang, T. Pähtz, Y. Liu, X. Wang, R. Zhang, Y. Shen, R. Ji, and B. Cai, "Electric field and humidity trigger contact electrification," *Physical Review X*, vol. 5, no. 1, p. 011002, 2015.

[166] E. B. Shand, "Glass engineering handbook," 1958.

[167] W. M. Haynes, *CRC Handbook of Chemistry and Physics.* CRC Press, 2014.

[168] R. A. Millikan, "The general law of fall of a small spherical body through a gas, and its bearing upon the nature of molecular reflection from surfaces," *Physical Review*, vol. 22, no. 1, p. 1, 1923.

[169] H. Masuda and K. Iinoya, "Electrification of particles by impact on inclined metal plates," *AIChE Journal*, vol. 24, no. 6, pp. 950–956, 1978.

[170] S. Timoshenko and T. Goodier, *Theory of Elasticity.* McGraw-Hill New York: USA, Chapter 12, 1970.